Neutron Scattering Studies on Singlet Magnetic Ground State Systems

Neutron Scattering Studies on Singlet Magnetic Ground State Systems

By

SARA HARAVIFARD, B.Sc.

A Thesis

Submitted to the School of Graduate Studies

in Partial Fulfillment of the Requirements

for the Degree of

Master of Science

McMaster University

MASTER OF SCIENCE (2005) McMaster University

(Physics) Hamilton, Ontario

TITLE: Neutron Scattering Studies on Singlet Magnetic Ground State Systems

AUTHOR: Sara Haravifard, B.Sc. (McMaster University)

SUPERVISOR: Professor Bruce D. Gaulin

NUMBER OF PAGES: xvi, 118

Abstract:

An energy gap or "pseudogap", where there is spin pairing without phase coherence, has been observed in a number of unconventional superconductors that has been detected even above the superconducting transition. It has been proposed that this "pseudogap" region is intimately related to the appearance of high Tc superconductivity. Comparable spin gaps have been observed in a number of low dimensional quantum spin systems with a spin-singlet ground state. Therefore quantum magnets which show collective singlet ground states have been receiving much interest recently.

As an example of these; $CuGeO_3$ is one of the few quasi-one dimensional magnetic insulators which displays a Spin-Peierls transition. This novel transition results from the coupling of the lattice with S=1/2 spin degrees of freedom to break transitional symmetry below some characteristic phase transition temperature, and a collective singlet magnetic ground state with a characteristic energy gap is observed.

In my thesis I have studied the critical phenomena associated with the Spin-Peierls transition which occurs in the inorganic compound $Cu_{1-x}Cd_xGeO_3$ by means of X-ray Scattering. I also conducted inelastic neutron scattering experiments and studied the temperature dependence of the singlet-triplet excitation of this system. I applied different theoretical methods to determine the best model describing the behavior observed for this material and compared the results with those obtained on the pure compound.

There are few quasi two dimensional experimental examples of interacting dimers such as $SrCu_2(BO_3)_2$ which has been proposed as a realization of the Shastry-Sutherland

model. This system has been modeled as Heisenberg spins in a square lattice with two exchange coupling constants of magnitudes J and J' along the diagonal and the edges of the lattice. Its ground state is known to be a collective singlet state. It is known theoretically that its ground state changes from a gapped singlet to a gapless antiferromagnetic state as a function of J/J'. Recently, subleading terms in the Hamiltonian have been considered, such as Dzyaloshinski-Moriya interactions, which are needed to understand the precise physical properties of this material.

I performed high resolution, inelastic neutron scattering measurements on this material aim at clarifying the nature of the singlet-triplet excitation spectrum. The results revealed the dispersion relations along with the Q-dependence of the excitations. Finally, neutron powder diffraction measurements were also performed in order to investigate any possible structural phase transition in this material.

Acknowledgements:

I would like to express my sincere appreciation to my supervisor, Professor Bruce D. Gaulin for his unlimited support and continuous guidance during the course of this research. This work could not have been accomplished without his efforts. Sincere thanks are owed to Professor A. John Berlinsky for his collaboration and assistance throughout my study at McMaster University. I would like to thank as well the other member of my supervisory committee, Professor Graeme M. Luke, for taking the time to read this thesis and provide me with his useful comments.

I would like to express my gratitude toward the management and staff of Chalk River Laboratories, ON and NIST Laboratories, MD for their hospitality and assistance. Particularly, I offer my appreciations to Y. Qui, J. Copley and S. Lee of NIST, as well as W. J. L. Buyers, Z. Yamani, Z. Tun and L. Cranswick of Chalk River for their assistance on conducting the experiments. I should also thank my colleagues at McMaster University in particular H. Dabkowska, S. Dunsiger, J. Castellan and K. Rule.

I would like to extend my appreciation to my parents for their encouragement and support. Finally, I would like to express my deep gratitude to my beloved husband, Farzin, for his consistent support and sacrifices that made completion of this thesis possible.

Table of Contents:

List of Figures:

List of Tables:

Chapter 1

Phase Transitions and Quantum Magnetism:

1.1. Phase Transitions:

The degree of ordering in every system arises from the compromise between interactions that enforce order and thermal motion which acts to enhance disorder. As a result of the competition between the tendencies to minimize energy and to maximize entropy, many systems can form different macroscopic phases.

A *Phase transition* is the transformation of a thermodynamic system from one of its phases to another. Phase transitions happen when the free energy of a system is non-analytic for some choice of thermodynamic variables, which means that there is a discontinuity in the free energy of the system or one of its derivatives. The distinguishing characteristic of a phase transition is a sudden change in one or more physical properties (e.g. the transitions between the solid, liquid, and gaseous phases, or the transition

between the ferromagnetic and paramagnetic phases of magnetic materials at the Curie point).

1.1.1. Classification of phase transitions:

According to the *modern classification* scheme, phase transitions are divided into two broad categories which are defined as below:

First-order or Discontinuous Transition:

If there is a finite discontinuity in one or more of the first derivatives of the appropriate thermodynamic potential, the transition is *first-order* or *discontinuous*. For example in a magnetic system this can be a discontinuity in the magnetization and for a fluid the discontinuity can be in the volume.

One of the characteristic of a first-order phase transition is the existence of a latent heat. This means that during such a transition, a system either absorbs or releases a fixed amount of energy. Because energy cannot be instantaneously transferred between the system and its environment, first-order transitions are associated with "mixed-phase regimes" in which some parts of the system have completed the transition and others have not (e.g. boiling water).

Second-order or Continuous Transition:

The second class of phase transitions are the *second-order* or *continuous* phase transitions. If the first derivatives of thermodynamic potential are continuous but second derivatives are discontinuous or infinite, the transition will be described as higher order, continuous, or critical.

The key feature of a continuous phase transition is the presence of fluctuating micro regions of both phases near the critical point. The characteristic size of these fluctuating regions, which is called the correlation length ξ, tends to infinity at the critical point. (Collins 1989).

1.1.2. Magnetic phase transitions:

To further discuss the behavior near a critical point, let's focus on a magnetic system. Such a system involves a set of interacting magnetic moments which are located at lattice points of a crystal. These magnetic moments arise from the spin angular momentums of the unpaired electrons residing on the atoms in a crystalline solid.

Let's consider a ferromagnetic system. In this system, nearest neighbors interact in such a way that makes it favorable to have spins pointing in the same direction at some temperature below the critical temperature T_c. Thermal fluctuations may drive a region of the system into a state at which the spins are in opposite directions. Consequently, there will be an increase in the free energy of the system (Kadanoff 1976). If the energy required in the formation of such a "droplet" region is significantly greater than the

thermal energy present in the system (i.e. k_BT) then such a process will be unlikely to happen.

The thermal energy increases as the temperature rises and a larger number of these droplets are formed. However, the net magnetization (i.e. number of spins in one direction minus number of spins in the opposite direction) approaches zero. Therefore, the energy for formation of a droplet decreases as temperature approaches T_c, and consequently, size of the droplets increases rapidly. The size of the largest such droplet, defined as correlation length ξ, diverges with $T \rightarrow T_c$ (Stanley 1971).

The existence of a quantity, which is non-zero below a finite temperature T_c and zero above it, is an important feature associated with the critical points of a wide variety of physical systems. This quantity is called the *order parameter*.

1.1.3. Symmetry:

Phase transitions often take place between phases with different symmetry. The transition between a fluid (i.e. liquid or gas) and a crystalline solid is an example of these phase transitions. Generally, one phase participating in a phase transition is more symmetrical than the other. The transition from the more symmetrical phase to the less symmetrical one, such as the one in the case of fluid-solid transition, is a *symmetry-breaking* process.

The ferromagnetic transition is another example of a symmetry-breaking transition. This symmetry is broken in the ferromagnetic phase as a result of the

formation of magnetic domains containing aligned magnetic moments. Inside each domain, there is a magnetic field pointing in a fixed direction chosen spontaneously during the phase transition. In magnetic systems, there are three common symmetry breaking scenarios:

1. The magnetic moment has a component in only one direction. This is also known as discrete or Ising.
2. The spins are confined to a single plane – XY symmetry.
3. The spins are free to rotate throughout 3D space – Heisenberg symmetry.

1.1.4. Critical exponents and universality classes:

The phenomena associated with continuous phase transitions are called *critical phenomena*, due to their association with critical points. It is found both experimentally and theoretically, that a number of quantities diverge at phase transitions and follow a *power law* behavior close to T_c:

$$O(t) \sim t^{-\lambda} \tag{1.1}$$

where t is the *reduced temperature* and defined as:

$$t = 1 - T/T_c \tag{1.2}$$

and λ is called the *critical exponent*. Some examples of the power law behavior and the critical exponents for thermodynamic quantities are:

$$C \sim |t|^{-\alpha} \tag{1.3}$$

$$M_0(T) \sim t^{\beta} \tag{1.4}$$

$$\chi = (\partial M / \partial H)_T \sim |t|^{-\gamma} \tag{1.5}$$

It has been found that phase transition in some systems often possess the same set of critical exponents. Such systems are said to be in the same *universality class* (Kadanoff 1971). Therefore, universality states that it is possible for the systems belonging to same class to exhibit the same critical behavior and if one system is understood all the systems in the same class can be understood.

To explain power law behavior and critical exponents better; let's consider the case of spin -1/2 Ising model as an example. A classical spin variable s_i, with a value of 1 or -1, is placed on each lattice site. These spins interact according to a Hamiltonian as follow:

$$\mathcal{H} = -J \sum_{\langle i,j \rangle} s_i s_j - \sum_{\langle i,J \rangle} h_i s_i \tag{1.6}$$

where $\langle i, j \rangle$ denotes a sum over nearest spins.

In this Hamiltonian, the first term is responsible for the cooperative behavior and the possibility of a phase transition, in which J is the exchange energy. It can be seen that a positive J favors parallel alignment while a negative J favors antiparallel alignment of the spins. It can be seen from the Hamiltonian that a given spin i in this system feels the external field plus the internal fields created by its neighbors:

$$h_i(\{s\}) = \sum_{\langle i,J \rangle} J_{ij} s_j + h_i \tag{1.7}$$

By replacing the actual field by the *mean field*, we can calculate thermodynamic quantities such as the magnetization:

$$m_i = \tanh\left[\beta\left(\sum_{j\neq i} J_{ij} m_j + h_i\right)\right] \tag{1.8}$$

In principle, this is a set of many equations which should be solved for m_i and therefore further simplifications are required. Assuming the spatial homogeneity, $h_i = h$, and that surface effects are not important, then $J_{ij} = J(r_i,r_j) = J(|r_i - r_j|)$. We obtain:

$$m = \tanh\left[\beta(qJm + h)\right] \tag{1.9}$$

where,

$$qJ = \sum_{j\neq i} J_{ij} \tag{1.10}$$

For the case $h = 0$, the situation is as illustrated in Figure 1.1.

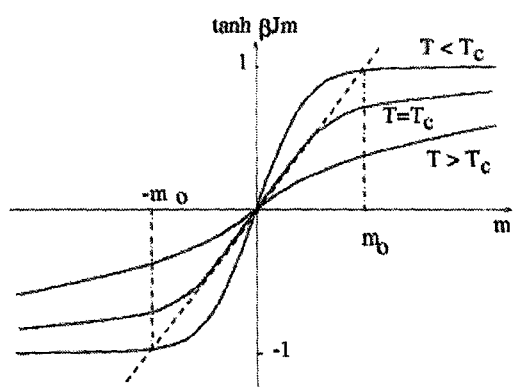

Figure 1.1: Graphical solution of the mean field equation. (Collins 1989)

Expanding the equation for m near the transition temperature T_c, the magnetization will have the following form:

$$m = \pm\sqrt{3}\left(\frac{T}{T_c}\right)\left(1-\frac{T}{T_c}\right)^{1/2} \sim t^{1/2} \qquad (1.11)$$

for which $t = 1 - T/T_c$. Then the critical parameter β in $m \sim t^{\beta}$ is found to be 1/2.

Model	β	γ	ν	α	δ	η
Mean Field	0.5	1.0	0.5	-	3	0
1D Models	-	-	-	-	-	-
2D Models						
Ising	0.125	1.75	1	0	15	0.25
XY	-	-	-	-	15	0.25
Heisenberg	-	-	-	-	-	-
3D Models						
Ising	0.326	1.238	0.6312	0.106	4.780	0.039
XY	0.345	1.316	0.669	-0.010	4.810	0.030
Heisenberg	0.367	1.388	0.707	-0.121	4.780	0.037

Table 1.1: Theoretical predictions for various critical exponents in the conventional universality classes (Collins 1989).

Similarly other power laws and other critical parameters can be derived. A similar calculation results in a power law for susceptibility, $\chi \sim t^{-\gamma}$, where the critical parameter γ is found to be about 1. Another quantity of interest which can be determined is the correlation length ξ. The predicted power law for ξ is $\xi \sim t^{-\nu}$, with $\nu = 1/2$ (Collins 1989).

1.2. Quantum Magnetism:

According to classical electromagnetic theory, magnetic fields are produced by electric currents or changing electric fields and that the magnetic fields far from the electric currents producing them can be described by a magnetic dipole. Therefore, it would be expected that magnetic effects in materials are produced by microscopic current loops created by the motion of electrons in atoms. However, Neils Bohr in 1911 showed that the phenomenon of diamagnetism does not exist in classical physics. Thus, the source of magnetism should be explained by quantum mechanics through the existence of an intrinsic magnetic moment, which in turn is proportional to the intrinsic spin.

Since in most magnetic materials the electrons responsible for magnetic behavior are localized near the atoms of a regular lattice, the simple case of two localized electrons is considered here as an example. Each electron has a spin 1/2 which can point either up or down along the axis which is specified by the applied magnetic field. The electrons interact with each other and with the nearby atoms and are described in part by the spatial

wavefunction $\psi(r_1, r_2)$. This wavefunction must be multiplied by the spin eigenstates to obtain the actual state of the two electron system. We denote the basis for these states as:

$$|\uparrow\uparrow\rangle, |\downarrow\downarrow\rangle, |\uparrow\downarrow\rangle, |\downarrow\uparrow\rangle \tag{1.12}$$

where the arrows corresponds to the spin of the electrons (Sakurai 1985)

These states are eigenstates of the z-component of the total spin angular momentum, S_z, such that S_z operating on any of these states has an eigenvalue equal to the sum of the spins in the z direction. For example:

$$S_z|\uparrow\uparrow\rangle = 1|\uparrow\uparrow\rangle \tag{1.13}$$

and

$$S_z|\uparrow\downarrow\rangle = 0|\uparrow\downarrow\rangle \tag{1.14}$$

Since electrons are fermions, the basis states in Equation 1.12 are not physically meaningful, because if two electrons are interchanged, the new wavefunction must either be the same or differ by only a minus sign. The simplest normalized linear combinations of the states in Equation 1.12 that satisfy this condition are:

$$\frac{1}{\sqrt{2}}\left(|\uparrow\downarrow\rangle - |\downarrow\uparrow\rangle\right) \tag{1.15}$$

$$|\uparrow\uparrow\rangle \tag{1.16}$$

$$\frac{1}{\sqrt{2}}\left(|\uparrow\downarrow\rangle + |\downarrow\uparrow\rangle\right) \tag{1.17}$$

$$|\downarrow\downarrow\rangle \tag{1.18}$$

The state in Equation 1.15 is antisymmetric, because interchanging the two electrons leads to minus the original state. This state has a total spin, $S = 0$, and is called the singlet state. The collection of the last three states (i.e. Equations 1.16 to 1.18) is called the triplet state and has $S = 1$. According to the Pauli principle the states of fermions must be antisymmetric, thus the spin state is antisymmetric when the spatial part of the wavefunction $\psi(r_1, r_2)$ is symmetric and vice versa. That is, if the spin state is symmetric, then $\psi(r_1, r_2) = -\psi(r_2, r_1)$. Similarly, if the spin state is antisymmetric, then $\psi(r_1, r_2) = +\psi(r_2, r_1)$. Hence, when $r_1 = r_2$, ψ is zero for symmetric spin states and is nonzero for antisymmetric spin states. This means that if the spins are parallel, the separation between the two electrons will rarely be small and their average electrostatic energy will be less than it is for antiparallel spins. This is referred to as the second Hund's rule.

A general model (and probably the most common one) for describing the total magnetic energy of magnetism for the spin-spin interaction is expressed as:

$$\mathcal{H} = -\sum_{i,j=1}^{N} J_{ij} S_i \cdot S_j - g\mu_0 H \cdot \sum_{i=1}^{N} S_i \qquad (1.19)$$

where $\mathcal{H}$ is the Hamiltonian operator, H is the external magnetic field, $g\mu_0$ is the magnetic moment of the electron and J_{ij} is the *exchange interaction* which can be positive or negative (Aschroft and Mermin 1976).

1.2.1. The Spin - Peierls transition:

The *spin-Peierls transition* (SP) occurs in antiferromagnetically coupled quantum (low S) spin chains with short range (*nn*) interactions and continuous symmetry (either Heisenberg or XY). This transition is typically described for $S = 1/2$ Heisenberg spin chains since these are the only examples found experimentally (Bray *et al.* 1983). This transition was initially widely studied, both experimentally and theoretically, in the 1970s. However, the experimental work was rather restricted, since there were only very few organic compounds known, which showed this transition. Thus, the observation of a spin-Peierls transition in the inorganic compound $CuGeO_3$ in 1993 by Hase *et al.* attracted widespread attention, since the structure of this material was not as complex as the previously studied organic samples.

For the occurrence of a spin-Peierls transition, several preconditions are necessary:

1. A crystal must contain (quasi-) one-dimensional antiferromagnetic spin chains of half-integer spin, i.e. the exchange coupling between neighboring spins along one crystal direction has to be much larger than those perpendicular to this direction.
2. A finite magneto-elastic coupling is necessary, i.e. the exchange interaction depends on the distance between neighboring sites.

In a strictly one-dimensional spin chain, even at $T = 0K$, no long-range anti-ferromagnetic order can develop. However, the magnetic energy can be lowered by a spin-Peierls transition. In order to understand the salient feature of the SP transition, let

us consider the excitation spectrum shown in Figure 1.2. In this figure $\varepsilon(q) = E(q) - E_{gs}$, where E_{gs} is the ground state energy.

For the particular case of uniform chains with the same antiferromagnetic coupling J, as shown in Figure 1.2(a), the important feature is the lack of a gap between the singlet ground state and the triplet excited state. Consequently, excitations at $q = 0, \pm \pi/a$ are infinitesimally close to the ground state energy. In the case of dimerized spin chain, as shown in Figure 1.2(b), below a certain transition temperature T_{sp} the distances between neighboring spins are no longer uniform. Due to the magneto-elastic coupling this leads to an alternation of the exchange coupling and each pair of stronger-coupled spins is forming a spin singlet. This results in a double unit cell and as can be seen in Figure 1.2(b), a gap separating a singlet ground state from a triplet excited state appears. This is often referred to as dimerization. This dimerization leads to a lower magnetic energy than in the uniform case which compensates the gain of elastic energy arising from the alternating structural distortion along the spin chains. For such a transition to occur, the lowering of magnetic energy due to the gapped excitation spectrum must outweigh the increase in lattice energy which is required to dimerize the chain. Thus, if the lattice is soft in the chain direction, and the chains are magnetically well separated from each other, a periodic deformation (dimerization) of the lattice takes place at a finite temperature T_{sp}. The lattice dimerization alternatively increases $J(1+\delta)$ or decreases $J(1-\delta)$ the anti-ferromagnetic interactions, and brings about singlet pair formations on the enhanced exchange links. Here δ has been defined as the dimensionless relative distortion. This is called spin-Peierls transition.

In a purely one-dimensional system, there can be no phase transition. Thus, within the Hamiltonian there must be some higher dimensionality in order to produce a finite transition. Physical realization of one-dimensional system occurs when interactions which are highly anisotropic, with much stronger interactions along one crystalline direction, appear due to geometry and exchange paths of the system. Therefore, physical one-dimensional systems are actually quasi-one dimensional systems with much stronger interaction along one direction.

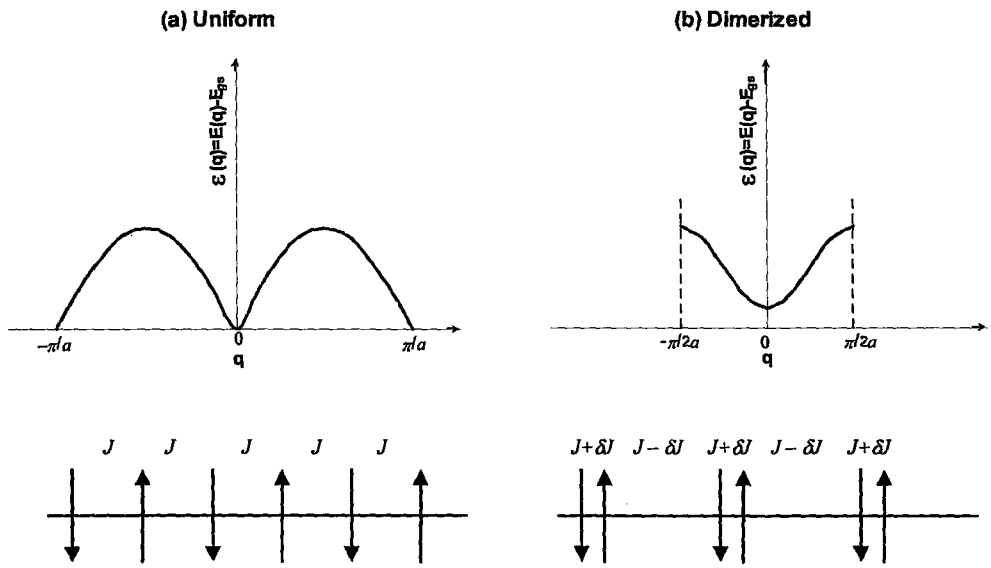

Figure 1.2: (a) An $S = 1/2$ spin chain with a uniform antiferromagnetic interaction J. (b) The lattice dimerized state below the spin Peierls transition temperature T_{sp} (Bray *et al.* 1983).

The ground state structure of the spin-Peierls system is a stacking of singlet pairs along the chain. The ground state is non-magnetic, because each singlet pair produces no

magnetic field. Since the singlet pairs are well localized, there is a finite energy gap between the ground state and the excited states. This energy gap is related to the amount of energy which is necessary to convert a single dimer of the singlet ground state into a triplet.

Experimentally, the spin-Peierls transition and the opening of a spin gap is observed in inelastic neutron scattering, magnetic susceptibility and X-ray scattering experiments. There are several characteristic features which signal the spin-Peierls transition. Below T_{sp}, superstructure reflections can be observed due to the structural distortion leading to the doubling of the unit cell. In addition, there is a drop of the magnetic susceptibility due to the formation of non-magnetic spin singlets. Finally, T_{sp} shows very characteristic magnetic field dependence.

1.2.2. Shastry-Sutherland Model:

In 1981, Shastry and Sutherland introduced a two-dimensional model for which geometrical frustration was essential. In this model, the spins are configured in such a way that each spin is coupled to pairs of spins. With the experimental realization of the Shastry-Sutherland model in the orthoborate $SrCu_2(BO_3)_2$ (Kageyama *et al.* 1999) synthesized by Smith and Kezler in 1991, the model attracted a lot of attention, as it became possible to compare the theoretical findings and experimental data directly.

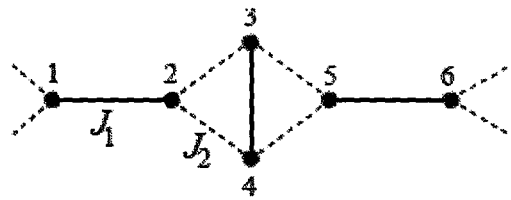

Figure 1.3: Illustration of a dimer solid. Spins are denoted by circles. Two spins interacting via J_1 couple to a dimer. The dimers interact via J_2. The singlet-on-dimers state is always an eigenstate.

The Hamilton operator describing the Shastry-Sutherland model, with spins of size $S = ½$ on the vertices is given by:

$$H = J_1 \sum_{\substack{\text{intra dimers} \\ i,j}} S_i S_j + J_2 \sum_{\substack{\text{inter dimers} \\ k,l}} S_k S_l \qquad (1.20)$$

in which, the sums run over all couplings between the sites connecting diagonal bonds (J_1), and between sites on different dimers (J_2), respectively. It can also be shown that the state in which all dimers are singlet is always an eigenstate (and for certain values of J_1 and J_2 a ground state) (Shastry and Sutherland 1981).

Figure 1.4 shows the Shastry-Sutherland model for the Hamiltonian described in Equation 1.20. In the limit $J_1 = 0$ a simple square lattice is obtained. For other cases, the model can be seen as a square lattice with additional (frustrating) diagonal bonds. The ratio $x = J_2/J_1$ is introduced as the inverse frustration. Because of the particular geometry of the system is sometimes called orthogonal dimer model (Miyahara and Ueda 1999).

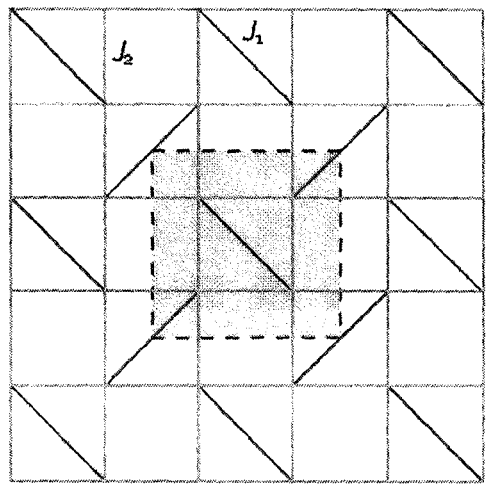

Figure 1.4: Shastry-Sutherland model with spins on the vertices. The couplings on the square lattice are parameterized by J_2 and the diagonal couplings (dimers) are parameterized by J_1. The grey shaded region depicts the unit cell of the system. (shastry and Sutherland 1981)

In their original work in 1981 Shastry and Sutherland designed this model in an effort to create a two- (and three-) dimensional system exhibiting an exact ground state made from a product of singlets. Shastry and Sutherland showed, that the dimer-singlet state is the exact ground state for $x = J_2/J_1 < ½$ (for spin $S = 1/2$). Consequently, the elementary excitations above the dimer-singlet ground state are given by promoting one of the singlets to a triplet.

The left part of Figure 1.5 shows the classical phase diagram (i.e. $S \rightarrow \infty$) of the Shastry-Sutherland model. It can be shown that there is a long range ordered anti-ferromagnetic phase (i.e. Néel phase) for large $J_2 > 0$ and a ferromagnetic ordering for large $J_2 < 0$ (Löw and Müller-Hartmann 2002).

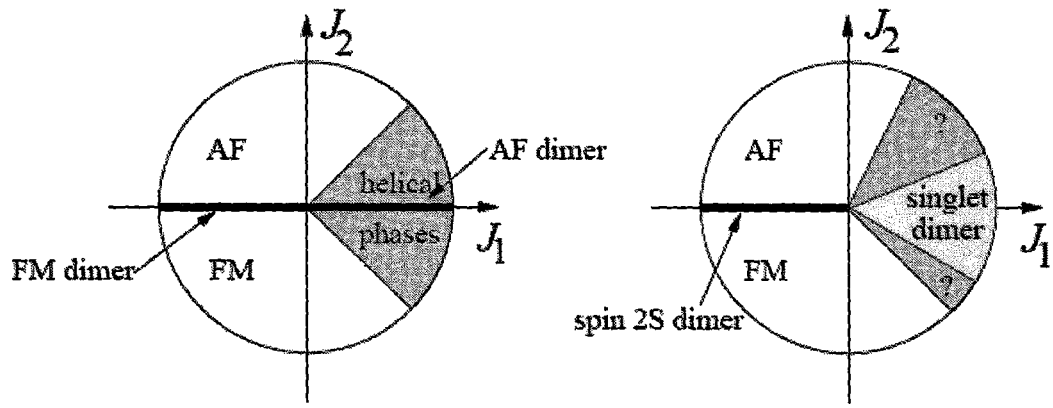

Figure 1.5: The left part shows the classical phase diagram of the two-dimensional Shastry-Sutherland model. The phase transition lines can be calculated exactly. The right part depicts the phase diagram in the quantum mechanical case ($S < \infty$). The singlet dimer phase covers a finite region. The nature of the adjacent phases is not understood yet (Löw and Müller-Hartmann 2002).

In the quantum mechanical regime (i.e. $S < \infty$), the dimer-singlet product state becomes the exact ground state for $J_1 > 0$ and J_2 not too large. The phase diagram on the $J_1 < 0$ side is similar to the classical phase diagram. This is sketched in the right part of Figure 1.5. In 1999, Miyahara and Ueda found that this dimer to Néel transition occurs at $x_c = J_2/J_1 \approx 0.7$, which is a broadly accepted value. Recently, there has been discussion suggesting the existence of an intermediate phase between the singlet collective ground state and long range antiferromagnetic state. The existence and nature of this intermediate phase is still an open question (Miyahara and Ueda 2003).

Chapter 2

X-ray and Neutron Scattering:

2.1. Introduction:

In order to resolve details of condensed matter structures, most of the time a scattering experiment is conducted. When the atomic positions are arranged in a crystal lattice the well known idea of Bragg (1913) can be used to understand the scattering intensity distribution. The incoming waves are *reflected* by parallel lattice planes defined by the periodically aligned atoms. Diffraction maxima are visible if the path difference is an integer multiple of the wavelength,

$$2d\sin\theta = n\lambda \tag{2.1}$$

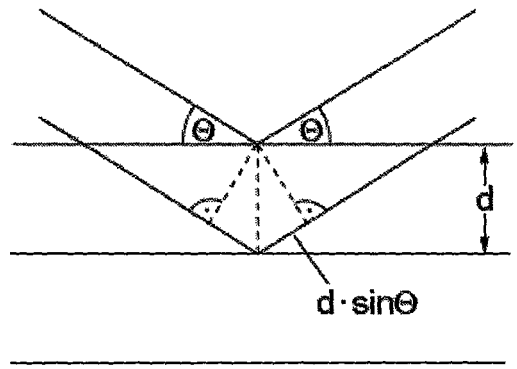

Figure 2.1: Diffraction geometry with path difference of waves scattered at a crystal lattice (Aschroft and Mermin 1976).

2.2. Scattering from crystals:

In general, the nucleus in an atom is surrounded by a spatial distribution of electrons, which can be described by a local electron density $n_e(r)$ within the atomic volume V. The summation of scattering amplitudes of all electrons using correct phase shifts leads to the atomic structure factor $f_j(Q)$:

$$f_j(Q) = \int_V dV n_e(r) e^{iQ.r} \tag{2.2}$$

Due to this spatial distribution of the shell electrons, there is always a Q-dependence of x-ray scattering. This Q-dependence is absent for non-magnetic neutron scattering experiments, since the nucleus appears as a *point source* on the scale of the thermal neutron wavelengths. However, for neutron scattering, a Q-dependence occurs for the magnetic scattering where the magnetic moment caused by unpaired electrons

couples to the magnetic moment of the neutron. Normally, only a few electrons orbiting in the outer shell of the atom will contribute to the magnetic moment. Therefore, the magnetic scattering form factor for neutrons is not identical to the electronic form factor for x-rays.

Let's consider a Bravais lattice with N atoms described by their position vectors $r_n = n_1a + n_2b + n_3c$ where a, b and c are basis vectors in real space. For simplicity, only one type of atom is assumed to be present, thus $f_n = f$. The scattered amplitude of such a lattice is then given by the phase-correct addition of all separate scattering contributions:

$$\begin{aligned} F'(Q) &= \sum_{n}^{N} f_n e^{iQ\cdot r_n} \\ &= f(Q) \sum_{n_1,n_2,n_3}^{N} e^{iQ\cdot(n_1a+n_2b+n_3c)} \\ &= f(Q)\left(\sum_{n_1}^{N_1} e^{in_1Q\cdot a}\right)\left(\sum_{n_2}^{N_2} e^{in_2Q\cdot b}\right)\left(\sum_{n_3}^{N_3} e^{in_3Q\cdot c}\right) \end{aligned} \tag{2.3}$$

where the lattice sum over N atoms in the crystal is separated into three partial sums over N_1, N_2 and N_3.

The condition for constructive interference with sharp maxima requires that each of the three factors has to be non-zero, individually. This means that Q has to satisfy three equations simultaneously:

$$Q\cdot a = 2\pi h \quad Q\cdot b = 2\pi k \quad Q\cdot c = 2\pi l \tag{2.4}$$

where h, k and l are any set of integers. These conditions are known as *Laue conditions*.

In order to identify the solutions of the scattering vector Q that fulfill these conditions $Q = hA + kB + lC$ with a new set of basis vectors A, B and C is made, where:

$$A = \frac{2\pi}{V_c}(b \times c) \quad B = \frac{2\pi}{V_c}(c \times a) \quad C = \frac{2\pi}{V_c}(a \times b) \tag{2.5}$$

and $V_c = a \cdot (b \times c)$ is the volume of a unit cell. The vectors A, B and C have the dimension of a reciprocal length; therefore the lattice they span is called the reciprocal lattice. In this way, each crystal has two associated lattices, the real lattice with its points $r = n_1a + n_2b + n_3c$ and the reciprocal lattice with its points $G = hA + kB + lC$.

The role of the reciprocal lattice can be illustrated further with the discussion of the momentum transfers during the scattering process. Figure 2.2 shows the scattering triangle made up by Q, k_i and k_f together with the reciprocal lattice points. The constructive interference occurs when the scattering vector Q coincides with the lattice vector G:

$$Q = k_i - k_f = G \tag{2.6}$$

Multiplying this equation by $\hbar$ delivers:

$$\hbar Q = \hbar k_f - \hbar k_i = \hbar G \tag{2.7}$$

with $\hbar k = 2\pi\hbar/\lambda = h/\lambda = p$ being the momentum. Hence, Equation 2.7 stands for the momentum conservation in the scattering process.

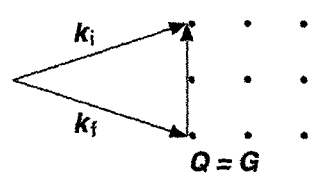

Figure 2.2: Diffraction geometry with path difference of scattered waves.

This fact was used by P. P. Ewald for an instructive geometric interpretation of the Bragg's law and the prediction of allowed scattering maxima, as illustrated in Figure 2.3. In the figure, k_i shows the direction of the incoming beam and may end at any point of the reciprocal lattice. A sphere of radius $|k_i| = 2\pi/\lambda_i$ around the origin of k_i gives the length of k_i of the scattered beam. Now, any point of the reciprocal lattice on the surface of the sphere defines a diffracted beam, $k_f = k_i - G$.

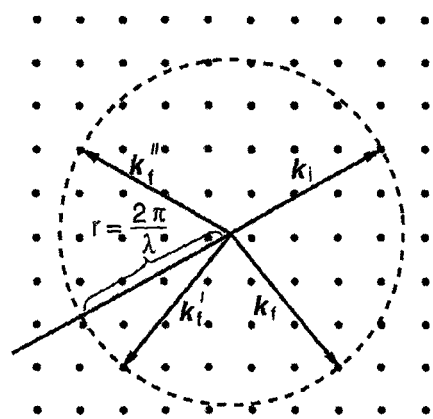

Figure 2.3: Allowed k_f leading to scattering maxima according to the Ewald construction (Aschroft and Mermin 1976).

2.3. Neutron Scattering:

Neutron scattering is a powerful tool to probe dynamic and static properties of condensed matter at microscopic levels. The energies of cold and thermal neutrons are of the order of microscopic excitations in condensed matter and the wavelengths of cold and thermal neutrons are comparable to the intermolecular distances. Since neutrons have no

electrical charge, there is no Coulomb interaction between them and the nuclei of the sample, and therefore they can easily and deeply penetrate the material.

Neutron scattering events are described by means of energy and momentum transfer. The kinematics of a neutron scattering event is shown in Figure 2.4. A neutron with incident momentum p_0 and incident wave-vector k_0 has incident energy of:

$$E_0 = \frac{{p_0}^2}{2m} = \frac{\hbar^2 {k_0}^2}{2m} \tag{2.8}$$

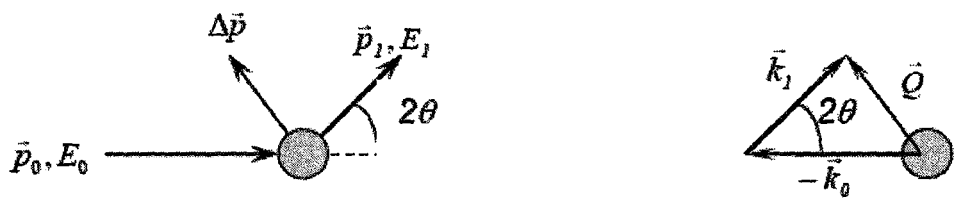

Figure 2.4: Neutron scattering kinematics in real space (left) and in reciprocal space (right) (Squires 1986).

After interactions with the sample, the neutron scatters to the direction 2θ, with a momentum p_1, a wave-vector k_1 and energy E_1. As with any particle scattering technique, the energy and the momentum conservation are the two basic principles of neutron scattering. The energy conservation allows defining the energy transfer of the incident and scattered neutrons:

$$\hbar\omega = E_1 - E_0 = \frac{\hbar^2}{2m}\left({k_1}^2 - {k_0}^2\right) \tag{2.9}$$

Eventually, momentum conservation makes it possible to define the scattering vector Q:

$$\hbar Q = p_1 - p_0 = \hbar k_1 - \hbar k_0 \tag{2.10}$$

The magnitude of Q is related to the incident and scattered neutron energies and to the scattering angle 2θ as follows:

$$Q^2 = \frac{2m}{\hbar^2}\left(E_0 + E_1 - 2\sqrt{E_0 E_1}\cos 2\theta\right) \tag{2.11}$$

Both the sign and the magnitude of the energy transfer are used to classify the neutron scattering event, as shown in Figure 2.5.

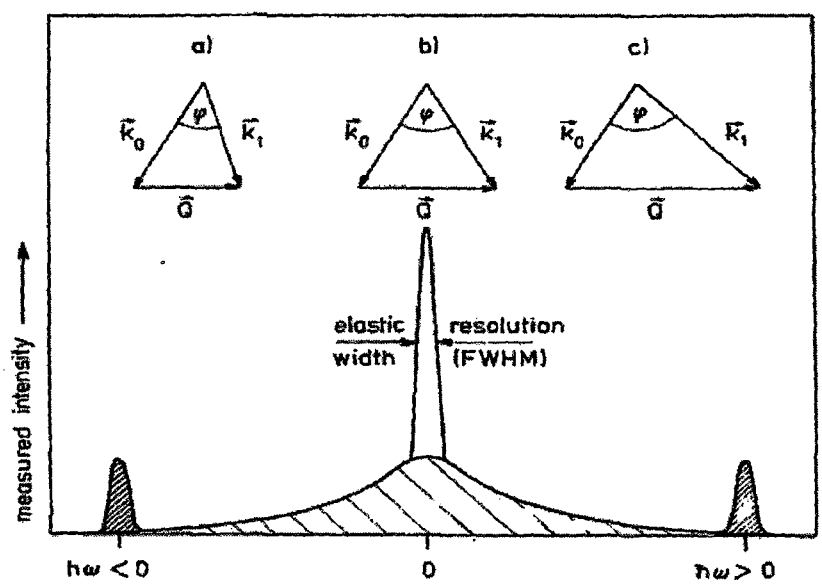

Figure 2.5: Neutron scattering spectrum as a function of energy transfer. The momentum conservation triangles are shown for processes of a) neutron energy loss, b) elastic scattering and c) neutron energy gain (Squires 1986).

Neutron scattering is considered elastic, when $\Delta\hbar\omega = E_1 - E_0 = 0$, i.e. the neutrons do not change their energy in the scattering process. If neutrons either gain (i.e. $\Delta\hbar\omega > 0$), or loose energy (i.e. $\Delta\hbar\omega < 0$) in the scattering process, the scattering is called inelastic.

2.3.1. Neutron scattering cross-section:

The quantity measured in a neutron scattering experiment is the double differential cross-section, $\partial^2\sigma/\partial\Omega\partial E_1$, which gives the proportion of neutrons with an incident energy E_0 scattered into a solid angle element $d\Omega$ with an energy between E_1 and E_1+dE_1. The geometry of the scattering experiment is shown in Figure 2.6.

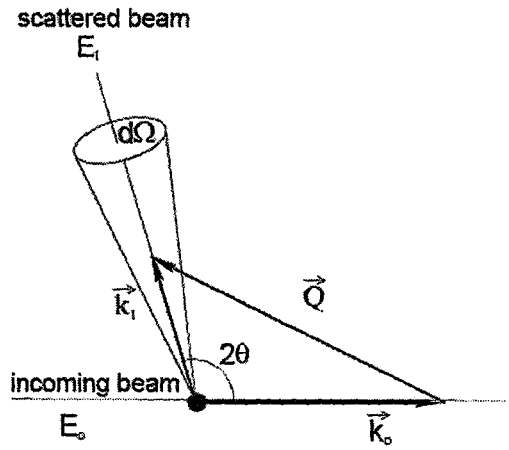

Figure 2.6: Scattering geometry from a single core (Squires 1986).

An incident neutron with a wave vector k_0 is scattered into a state with wave vector k_1. Before and after the interaction with the neutron, the sample can be described by the quantum states λ_0 and λ_1, respectively. The probability that the combined state of the neutron and the sample makes the transition from the initial state $|k_0\lambda_0\rangle$, to the final state $|k_1\lambda_1\rangle$ is given by Fermi's Golden Rule:

$$\sum_{k_1 \text{ in } d\Omega} W_{k_0,\lambda_0\to k_1,\lambda_1} = \frac{2\pi}{\hbar}\rho_{k_1}\left|\langle k_1\lambda_1|V|k_0\lambda_0\rangle\right|^2 \qquad (2.12)$$

Where ρ_{k_1} is the density of the final states of the neutrons described by k_1 in $d\Omega$ and V is the interaction potential between the nuclei in the sample and the neutron. Using the Born approximation for the cross-section, the double differential cross section is given by:

$$\frac{\partial^2\sigma}{\partial\Omega\partial E_1}=\frac{k_1}{k_0}\sum_{\lambda_0\lambda_1}p_{\lambda_0}\left|\langle k_1\lambda_1|V|k_0\lambda_0\rangle\right|^2\delta(\hbar\omega+E_{\lambda_0}-E_{\lambda_1}) \tag{2.13}$$

where the δ-function is included to ensure the energy conservation with the neutron energy transfer $\hbar\omega$, the initial sample energy E_{λ_0} and the final sample energy E_{λ_1}. In this equation, p_{λ_0} is the probability that the initial state of the sample is λ_0. This probability is given by Boltzmann distribution:

$$p_{\lambda_0}=\frac{1}{Z}e^{-E_{\lambda_0}/k_BT}\text{, and } Z=\sum_{\lambda_0}e^{-E_{\lambda_0}/k_BT} \tag{2.14}$$

k_B is the Boltzmann constant, Z the partition function of the sample and T the sample temperature. After further manipulations, the double differential scattering cross-section can be written as:

$$\frac{\partial^2\sigma}{\partial\Omega\partial E_1}=\frac{1}{2\pi\hbar}\frac{k_1}{k_0}\sum_{j,i}\overline{b_jb_i}\int\left\langle e^{-iQR_i(0)}e^{-iQR_j(t)}\right\rangle e^{-i\omega t}dt \tag{2.15}$$

where bj and bi are the scattering lengths of the j^{th} and i^{th} nuclei, $R_i(0)$ is the position operator of the i^{th} nucleus at time zero, $R_j(t)$ is the position operator of the j^{th} nucleus at time t, and $\langle\ \rangle$ denotes a thermal average.

The average $\overline{b_j b_i}$ for cases $j = i$ and $j \neq i$ is given as $\overline{b_j b_i}^{j=i} = \overline{b^2}$,and $\overline{b_j b_i}^{j\neq i} = \bar{b}^2$; therefore Equation 2.15 can be written as a sum of two components, due to the different mean values for cases $j = i$ and $j \neq i$ as follows:

$$\begin{aligned}\frac{\partial^2\sigma}{\partial\Omega\partial E_1} &= \frac{1}{2\pi\hbar}\frac{k_1}{k_0}\bar{b}^2\sum_{j,i}^{j\neq i}\int\left\langle e^{-iQR_i(0)}e^{-iQR_j(t)}\right\rangle e^{-i\omega t}dt \\ &+\frac{1}{2\pi\hbar}\frac{k_1}{k_0}\overline{b^2}\sum_{j}^{j=i}\int\left\langle e^{-iQRj(0)}e^{-iQR_j(t)}\right\rangle e^{-i\omega t}dt\end{aligned} \tag{2.16}$$

This leads to the introduction of *coherent* and *incoherent* scattering, related to the terms of the sum in Equation 16 respectively. The coherent scattering arises from interference effects and would be the scattering if all the nuclei of any element had the same scattering length b. The incoherent scattering, on the other hand, does not arise from interference effects and is related to the distribution or deviation of scattering length from the mean value $\bar{b}$ and therefore is proportional to $\overline{b^2} - \bar{b}^2$. The coherent and the incoherent scattering cross section into all directions can be defined as follows:

$$\begin{aligned}\sigma_{coh} &= 4\pi\bar{b}^2 \\ \sigma_{inc} &= 4\pi\left(\overline{b^2} - \bar{b}^2\right)\end{aligned} \tag{2.17}$$

Subsequently, the double differential cross section can be re-written as:

$$\begin{aligned}\frac{\partial^2\sigma}{\partial\Omega\partial\omega} &= \frac{1}{8\pi^2\hbar}\frac{k_1}{k_0}\sigma_{coh}\sum_{j,i}\int\left\langle e^{-iQR_i(0)}e^{-iQR_j(t)}\right\rangle e^{-i\omega t}dt \\ &+\frac{1}{8\pi^2\hbar}\frac{k_1}{k_0}\sigma_{inc}\sum_{j}\int\left\langle e^{-iQRj(0)}e^{-iQR_j(t)}\right\rangle e^{-i\omega t}dt \\ &=\left(\frac{\partial^2\sigma}{\partial\Omega\partial\omega}\right)_{coh}+\left(\frac{\partial^2\sigma}{\partial\Omega\partial\omega}\right)_{inc}\end{aligned} \tag{2.18}$$

The coherent scattering contains information about the correlation between the positions of different nuclei and the collective excitations in a sample. The incoherent scattering component can provide information about the individual nuclei and single particle excitations in the sample.

2.3.2. Scattering functions:

The pair-correlation function describes the position of nuclei in space and time, and is given for N nuclei as:

$$G(R,t)=\frac{1}{N}\sum_{i,j}^{N}\left\langle \delta\left\{R+R_i(0)-R_j(t)\right\}\right\rangle \tag{2.19}$$

The space Fourier transformation of the pair-correlation function $G(Q,t)$ is called intermediate scattering function:

$$I(Q,t)=\int_{-\infty}^{\infty}G(R,t)e^{iQ.R}dR=\frac{1}{N}\sum_{i,j}\left\langle e^{-iQ.R_i(0)}e^{-iQ.R_j(t)}\right\rangle \tag{2.20}$$

A time Fourier transform of the intermediate scattering functions leads to the scattering function (also called as the dynamic structure factor), which provides information on the sample states as a function of energy and momentum:

$$S(Q,\omega)=\frac{1}{2\pi\hbar}\int_{-\infty}^{\infty}I(Q,t)e^{-i\omega t}dt \tag{2.21}$$

Both $I(Q,t)$ and $S(Q,t)$ can be divided into a coherent and an incoherent part. The relationship between the coherent and incoherent scattering functions and the double differential scattering cross section can be written as:

$$\frac{\partial^2\sigma}{\partial\Omega\partial E} = \frac{\sigma_{inc}}{4\pi\hbar}\frac{k_1}{k_0}NS_{inc}(Q,\omega) + \frac{\sigma_{coh}}{4\pi\hbar}\frac{k_1}{k_0}NS_{coh}(Q,\omega) \qquad (2.22)$$

2.3.3. Magnetic cross-section:

The interaction between the magnetic moment of a neutron μ_n, and the electrons inside the scattering system originates from the Zeeman interaction of the neutron with the magnetic field distribution inside the sample arising from the spin and orbital angular momenta of unpaired electrons. The magnetic moments of a neutron is given by $\mu_n = -\gamma\mu_N\sigma_n$ where $\gamma = 1.913$ is the gyromagnetic ratio of the neutron, and $\mu_N = 5.051 \times 10^{-27}$ J/T is the nuclear magneton. If p denotes the electron momentum operator and R the distance vector measured from this electron, then by introducing the unit vector $\hat{R} = R/|R|$, the total Zeeman interaction with the field produced by this electron can be derived from electromagnetic theory:

$$V_{mag}(r) = \frac{\mu_0}{2\pi}\gamma\mu_N\mu_B\sigma_n\cdot\left(\nabla\times\left(\frac{s\times R}{|R|^2}\right) + \frac{1}{\hbar}\frac{p\times\hat{R}}{|R|^2}\right) \qquad (2.23)$$

where $\sigma_n = 2s_n$ is the Pauli spin operator and s is the operator for the electron spin.

The first term originates from the field created by the magnetic moment associated with the electronic spin angular momentum. The second term comes from the orbital angular momentum of electronic charges. The motion of these charges may be viewed as current elements and hence contributes to the field distributions as described by the law of Biot and Savart.

Substituting this electromagnetic potential into double partial differential cross section one can come up with the equation for magnetic scattering differential cross section. This was first pointed out by Van Hove (1954):

$$\left(\frac{\partial^2\sigma}{\partial\Omega\partial E_1}\right)_{mag} = \frac{1}{\hbar}\frac{k_1}{k_0}(\gamma r_0 g/2)^2 |F(Q)|^2 \exp(-2W)\sum_{\alpha\beta}\left(\delta_{\alpha\beta} - \hat{Q}_\alpha\hat{Q}_\beta\right)S^{\alpha\beta}(Q,\omega) \quad (2.24)$$

The scattering function $S^{\alpha\beta}(Q,\omega)$ is then given by:

$$S^{\alpha\beta}(Q,\omega) = \frac{1}{2\pi}\sum_{R,R'}\exp\left(-iQ\cdot(R-R')\right)\int_{-\infty}^{\infty}dt\,\exp\left(-i\omega t\right)\left\langle S_R^{\alpha}(0)S_{R'}^{\beta}(t)\right\rangle \quad (2.25)$$

A useful property of $S(Q,\omega)$ is that it is connected to the imaginary part of the generalizedmagnetic susceptibility $\chi(Q,\omega) = \chi'(Q,\omega) + i\,\chi''(Q,\omega)$ through the fluctuation-dissipation theorem (Furrer 1995):

$$S(Q,\omega) = [n(\omega)+1]\chi''(Q,\omega) = \frac{\chi''(Q,\omega)}{1-\exp(-\hbar\omega/k_BT)} \quad (2.26)$$

in which the exponential term is called the Bose factor. The imaginary part of the susceptibility $\chi''(Q,\omega)$ is a very important property of the system and describes how the system responds to external forces. For instance, magnetic susceptibility of a system characterizes the magnetic response of that system to the magnetic field:

$$M(Q,\omega) = \chi''(Q,\omega)\, H(Q,\omega) \tag{2.27}$$

The probability that a neutron gains an energy ω is different from the probability that a neutron looses an energy ω in the scattering process. This is due to the fact that it is $\exp(-\hbar\omega / k_B T)$ times less probable for the system to be in a higher initial state. Hence, the scattering function has to be corrected for this factor when calculating the susceptibility at different temperatures and energy transfers and this is exactly what the Bose factor does in Equation 2.26.

2.4. Instruments:

2.4.1. Triple-Axis Spectrometers:

A triple-axis spectrometer is an extremely simple machine. It is based only on the Bragg's law and simple geometry in reciprocal space. In a triple-axis experiment a beam of neutrons traverses a path through the instrument determined by the settings of three angles θ_S, θ_M and θ_A. Figure 2.7 shows a triple-axis spectrometer with a monochromator crystal, located in the beam path from source to sample position, and an analyzer crystal, located in the path from sample to detector. Monochromators and analyzers are either

perfect crystals or crystals that have been deformed in a controlled manner to obtain certain characteristic properties. Typical monochromator and analyzer materials are pyrolytic graphite (PG), silicon and germanium.

At the monochromator and analyzer positions neutrons are reflected according to Bragg's law:

$$n\lambda = 2d \sin\theta_i \tag{2.28}$$

where n is an integer and $i = M, A$ for monochromator and analyzer respectively. The setting of the angle θ_i causes a family of crystal planes, characterized by their distance d, to diffract exactly those neutrons with wavelengths $\lambda = 2\pi/k$ determined by Equation 2.28. Hence, a monochromator transforms a polychromatic beam of neutrons to a beam of neutrons with wavenumbers k, $2k$, etc. When this beam hits the sample, the scattered neutrons leave the sample along a distribution of directions and with a distribution of energies and spin directions which are determined by the spin-dependent partial differential scattering cross-sections.

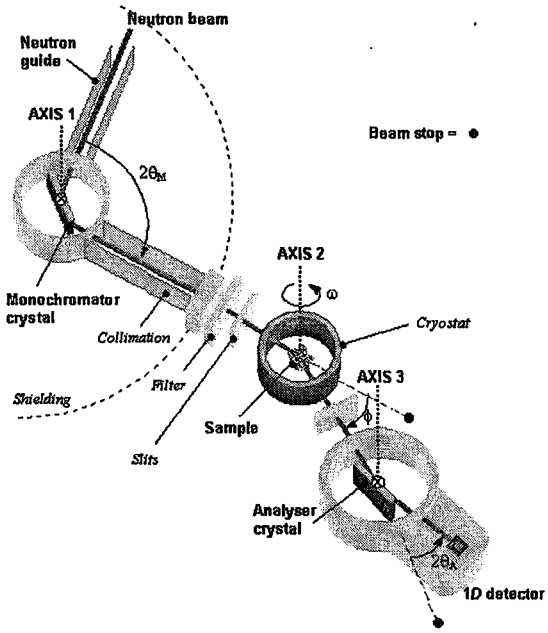

Figure 2.7: The layout of a triple-axis spectrometer (Connolly 2003).

By varying the scattering angle θ_S between k_i and k_f, the angular distribution can be explored. At the same time, the energy distribution in each given direction can be studied by varying the analyzer angle θ_A. Additional information may be collected by considering not only the change in momentum and energy of the neutron in the scattering process, but also possible changes in its spin state.

2.4.2. Time-of-Flight Spectrometers:

The time-of-flight method complements the triple-axis spectrometer technique. The triple-axis spectrometer is ideally suited to the study of excitations in oriented samples at specific points in (Q,ω) phase space. Time-of-flight instruments, on the other

hand, may be used to explore rather large regions of phase space since many detectors simultaneously collect neutrons over a wide range of values of the scattered energy.

Figure 2.8 illustrates a simple time-of-flight spectrometer. Neutron beam from the reactor reflects from a monochromator crystal. The monochromatic beam, characterized by its energy E_0 and wave vector k_0, is then pulsed by a chopper placed at a known distance L_{CS} from the sample. An array of detectors is arranged at a known fixed distance L_{SD} from the sample, and scattered neutrons arrive at the detectors at times determined by their scattered energies E. The time of flight of a neutron from the chopper is given by:

$$t_{CD} = t_{CS} + t_{SD} = \tau_0 L_{CS} + \tau L_{SD} \tag{2.29}$$

where t_{CS} and t_{SD} are the times of flight of the neutron from chopper to sample and from sample to detector, respectively, and τ_0 and τ are the reciprocal velocities of the neutron before and after scattering. If the initial energy E_0, is known, then using t_{CD} and the final energy E, the energy transfer (i.e. $\hbar\omega = E_0 - E$) may be determined. Given the angle between the incident and scattered neutron wave-vectors, the wave-vector transfer (i.e. $Q = k_0 - k$) can also be calculated.

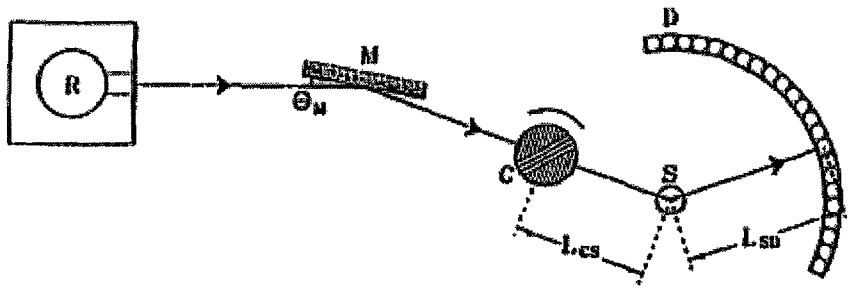

Figure 2.8: Schematic plan view of a simple time-of-flight spectrometer. The letters *R*, *M*, *C*, *S*, and *D* denote the reactor, monochromator, chopper, sample and detectors, respectively (Copley and Udovic 1993).

2.4.3. Powder Diffractractrometers:

A polycrystalline aggregate or powder is referred to the kind of materials that are not single crystals, but are composed of billions of tiny crystallites, called. In these materials there will be a great number of crystallites in all possible orientations. When a powder with randomly oriented crystallites is placed in an incident beam, the beam will see all possible interatomic planes. This can be explained using the Ewald sphere:

- There is a d^*_{hkl} vector associated with each point in the reciprocal lattice with its origin on the Ewald sphere at the point where the direct incident beam exists.
- Each crystallite located in the center of the Ewald sphere has its own reciprocal lattice with its orientation determined by the orientation of the crystallite with respect to the beam.

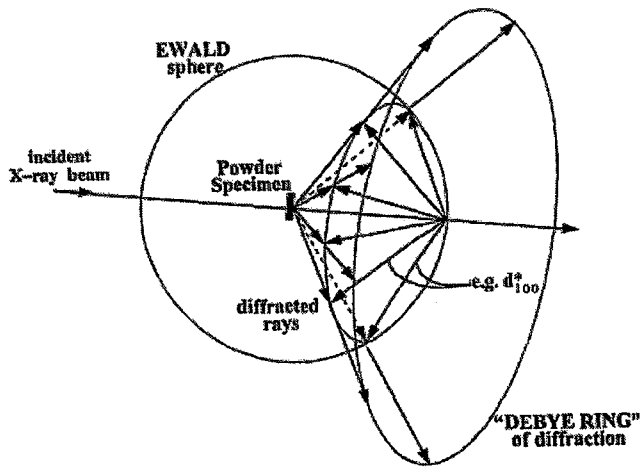

Figure 2.9: The intersection of d^*_{100} vectors from a powder with the Ewald sphere (Connolly 2003).

Figure 2.9 shows this geometry from the d^*_{100} reflection, which forms a sphere of vectors originating from the point of interaction with the beam. The number of vectors will be equal to the number of crystallites interacting with beam. The angle between the beam and the cone of diffraction is 2θ.

Chapter 3

X-ray Diffraction and Neutron Scattering from $CuGeO_3$:

3.1. Introduction:

The magnetic properties of low-dimensional systems of quantum spins with antiferromagnetic (AF) interactions display various interesting phenomena due to their quantum nature and their large fluctuations. The spin–Peierls (SP) transition in $S = 1/2$ Heisenberg chains with spin–lattice interactions (Bray *et al.* 1975) is one example. Studies of the SP transition already had a relatively long history of theoretical and experimental research (Bray *et al.* 1975); however experimental studies were limited to organic materials (Bray *et al.* 1975), which were difficult to grow as large single crystals and for which the doping or substitution of impurities was not possible. Therefore detailed studies of spin excitations by neutron inelastic scattering which requires

relatively large single crystals or the doping effects in SP systems had not been performed on organic SP materials.

This was the situation as of 1992, at which time Hase *et al.* (1993a) discovered a new SP compound, $CuGeO_3$, which was the first inorganic SP material. This discovery not only added a new material to the list of SP materials but a new phase of the studies on this problem had begun with it. This was mostly due to large, high-quality single crystals that could be grown, which allowed the properties of this compound to be studied thoroughly.

Because the two-dimensional CuO_2 planes are responsible for the high temperature superconductivity, AF oxides containing Cu^{2+} ions have been studied extensively since the discovery of cuprate superconductors in 1986. When the research on $CuGeO_3$ began in 1992, the motivation to study the magnetic properties of low-dimensional spin systems including linear chains with Cu^{2+} ions, was to compare one-dimensional Cu^{2+} based antiferromagnets with two-dimensional cuprate superconductors. Later on, detailed x-ray and neutron scattering techniques revealed both the spin and charge structures and the spin excitations of this material. In addition, studies could be performed on doping effects (Hase *et al.* 1993b). The simpler lattice structure, as compared with the previously known organic SP compounds, provided a more detailed theoretical understanding of the observed structural phase transition.

In this chapter, the general properties of $CuGeO_3$ and the SP transition will be discussed briefly and we will then be concerned with the $CuGeO_3$ in the presence of Cd impurities.

3.2. Structure of $CuGeO_3$:

$CuGeO_3$ possesses an orthorhombic unit cell which belongs to the *Pbmm* space group at room temperature. The lattice parameters at room temperature are $a = 4.81$ Å, $b = 8.47$ Å and $c = 2.941$ Å (Völlenkle *et al.* 1967) and the structure consists of Cu-O octahedra chains that are stacked along the *c*-axis and are separated along *a*-axis from one another by tetrahedra chains of Ge-O. Figure 3.1 schematically illustrates the crystal structure of $CuGeO_3$.

The magnetic properties of this material arise from the spin-1/2 moments of the Cu^{2+} ions. The distance between nearest neighbor Cu^{2+} ions, along the *c*-axis, is much shorter than that between the next-nearest ones along the *b*-axis. This causes strong super-exchange interactions mediated by the O^{2-} ions which are shared between adjacent octahedra along the *c*-axis. Also, larger Cu-Cu and Cu-O-Cu distances along the *b*-axis make both direct exchange and super-exchange interactions weaker than the ones along the *c*-axis. Along the *a*-axis, the magnetic moments are isolated from one another by Ge-O tetrahedra, giving rise to weaker interactions in this direction as well. Thus, we would expect quasi-one dimensional spin chains, knowing that the strongest interactions are along the *c*-axis with weaker exchange along the *b*-axis and the weakest along the *a*-axis.

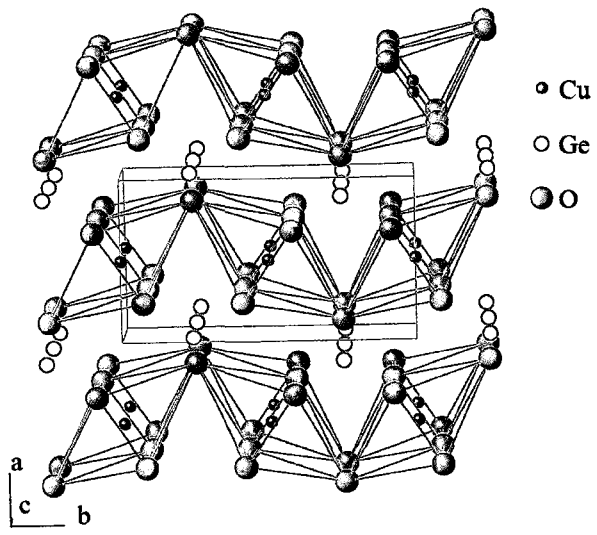

Figure 3.1: Crystal structure of $CuGeO_3$. The spin 1/2 Cu^{2+} chains are along the *c*-axis (Völlenkle *et al.* 1967).

3.3. Spin-Peierls Transition in $CuGeO_3$:

In 1993, the initial susceptibility measurements on $CuGeO_3$ were performed by Hase *et al.* who reported the detailed magnetic properties of this material and discovered the SP transition in this inorganic compound. The susceptibility versus temperature was measured along the three principal axes in a single crystal. These experimental results are shown in Figure 3.2 (Hase *et al.* 1993a). The most outstanding feature was that the characteristic susceptibilities $\chi(T)$ in all directions dropped exponentially to a small constant values below a temperature of about 14K. This suggested that some kind of phase transition exists. The susceptibilities above the transition temperature were found

to be almost isotropic and their temperature dependence characteristic was shown to be of a one-dimensional AF spin system (Bonner and Fisher 1964). These results are very good evidence for the existence of one-dimensional AF chain structure and a spin–Peierls transition at about 14K in $CuGeO_3$ (Hase *et al.* 1993a).

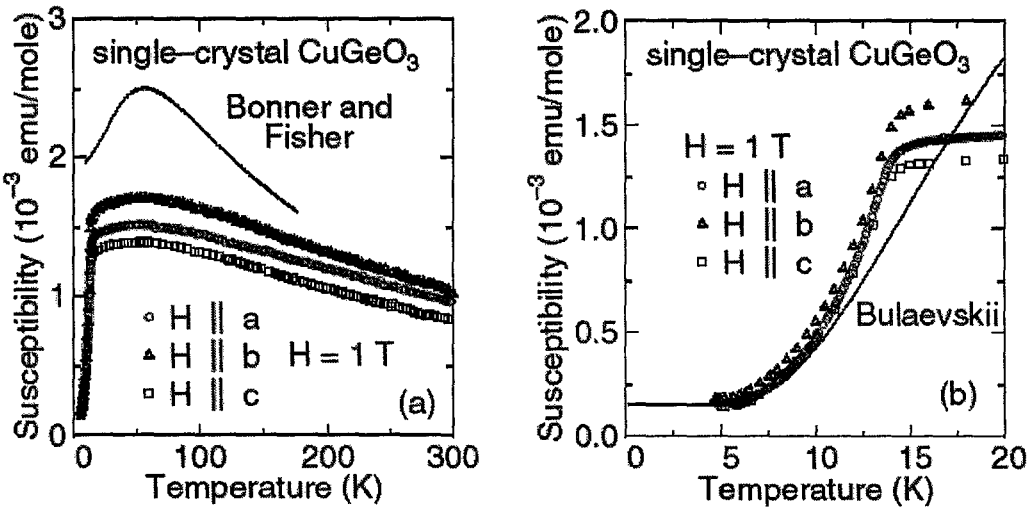

Figure 3.2: The magnetic susceptibility of single-crystal $CuGeO_3$ measured under H = 1T. (a) The solid curve is a theoretical one calculated by Bonner and Fisher (1964) with J = 88K. (b) The susceptibility below 20K. The solid curve is a theoretical one calculated by Bulaevskii (1969) (Hase *et al.* 1993a).

Nishi *et al.* (1994) showed the presence of a gapped excitation spectrum in $CuGeO_3$ using inelastic neutron scattering experiments. These measurements also allowed the excitations to be mapped out along the three crystalline directions in the form of dispersion curves. From the fits to these dispersion curves of low-energy spin excitations, the values of the exchange interactions along the chain for the *c* direction (the

nearest neighbor couplings) as well as the b and the a directions could be determined: J_c = 10.4 meV, $J_b \sim 0.1J_c$ and $J_a \sim -0.01J_c$. The values for J_b and J_a are just a fraction of the coupling along the chain direction, J_c, which confirms the quasi-one dimensional nature of the $CuGeO_3$ magnetic system.

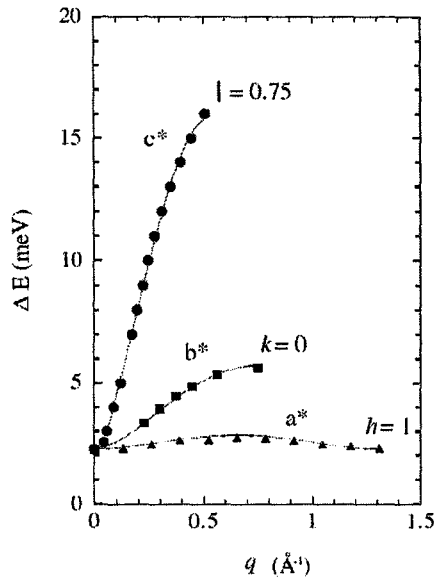

Figure 3.3: The dispersion relations of the magnetic excitants in $CuGeO_3$ along each principal axis at T = 4K for zone center (0, 1, 0.5) and q = 0. The solid curves indicate resultant curve fittings using the Heisenberg AF spin-wave formula. (Nishi *et al.* 1994).

It can also be concluded that the interactions along the c (chain) and b directions are antiferromagnetic while that along the a direction is ferromagnetic (Nishi *et al.* 1994). This means that $CuGeO_3$ is not a perfect one-dimensional spin system, but in some sense it may be considered as an anisotropic three-dimensional spin system. This contrasts with

typical organic SP materials, which were considered to be much better one-dimensional spin systems.

The existence of a spin excitation gap was supported later by other neutron inelastic scattering experiments (Kiryukhin and Keimer 1995, Regnault *et al.* 1996). These experiments not only showed a gapped excitation spectrum, but by applying magnetic field one could examine the nature of these excitations across the gap. The applied magnetic field resulted in a splitting of the excitation energies into three distinct components. This splitting increased with field, directly demonstrating the singlet-triplet nature of the excitations.

Another intrinsic property of the SP system is the dimerization of the lattice. The observation of superlattice reflections due to new periodicity, brought on by the dimerization of the spin chains, was not trivial and many neutron and x-ray diffraction experiments failed to detect it at first. Hence, there were initial doubts among the researchers regarding the validity of the SP transition as the mechanism of the phase transition in $CuGeO_3$. Finally, more than a year after the discovery of the SP transition in $CuGeO_3$ the dimerization of the lattice was found at almost the same time by electron, X-ray and neutron diffraction (Kamimura *et al.* 1994, Hirota *et al.* 1994, Pouget *et al.* 1994).

The reason for the difficulty in observing the lattice dimerization turned out to be that the dimerization was not a simple one and the satellite peaks did not exist only along the c^* direction, where the earlier studies had searched. These reflections were found to exhibit Miller indices ($h/2$, k, $l/2$) with h, l odd (Hirota *et al.* 1994). This indicated that

besides the doubling of the unit cell along the chain direction, there were additional dimerizations along *a*-axis that were not expected (Kamimura *et al.* 1994, Pouget *et al.* 1994). Furthermore, structure factor calculations indicated that these superlattice peaks were reduced in intensity by a factor of $\sim 10^{-4}$ when compared to principle Bragg peaks, which also made the detection of these reflections problematic (Hirota *et al.* 1994).

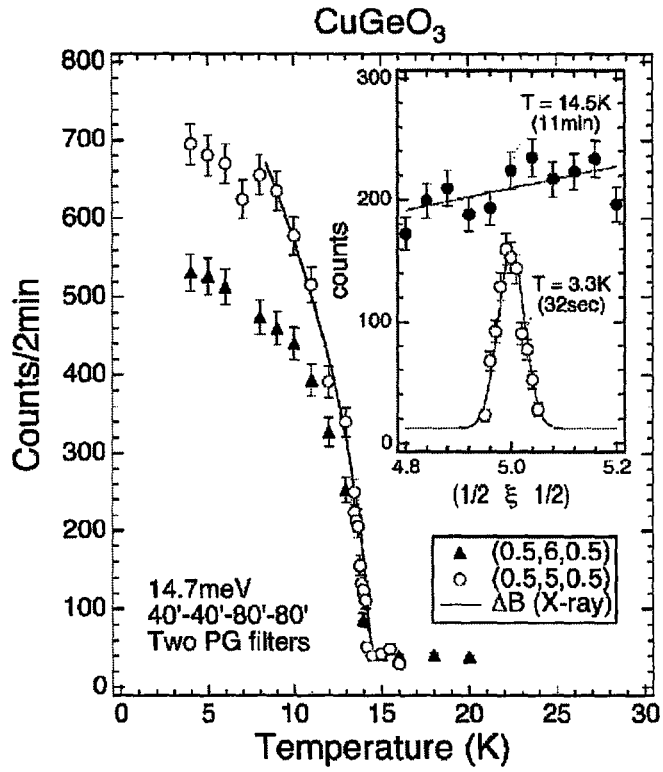

Figure 3.4: The temperature dependence of the superlattice reflections at (1/2, 5, 1/2) and (1/2, 6, 1/2) on heating. Peak profiles of the (1/2, 5, 1/2) reflection at 3.3K and 14.5K (T_{sp} = 14.2K) are shown in the inset (Hirota *et al.* 1994).

Considering the projection of the crystal structure onto the *a–c* plane, as is illustrated in Figure 3.5, one can understand these additional dimerizations. The Cu ion displacements are accompanied by the O ion displacements causing a boost in the exchange interactions within the dimers while they interfere with the superexchange interactions and consequently result in a reduction of the exchange interactions between the dimers. Hirota *et al.* (1994) proposed that these Cu ion displacements along *a*-axis are out of phase from one chain to the next, resulting in a doubly dimerized unit cell that can be seen in Figure 3.5.

Figure 3.6 shows the *H-T* phase diagram of $CuGeO_3$ (Hamamoto *et al.* 1994). The magnetic phase diagram of $CuGeO_3$ agrees qualitatively with both experimental results of typical organic SP materials (Bloch *et al.* 1980, Bloch *et al.* 1981, Northby *et al.* 1982) and a theoretical one (Cross 1979). This indicates that there are universal features to the phase diagram of SP systems, either organic or inorganic.

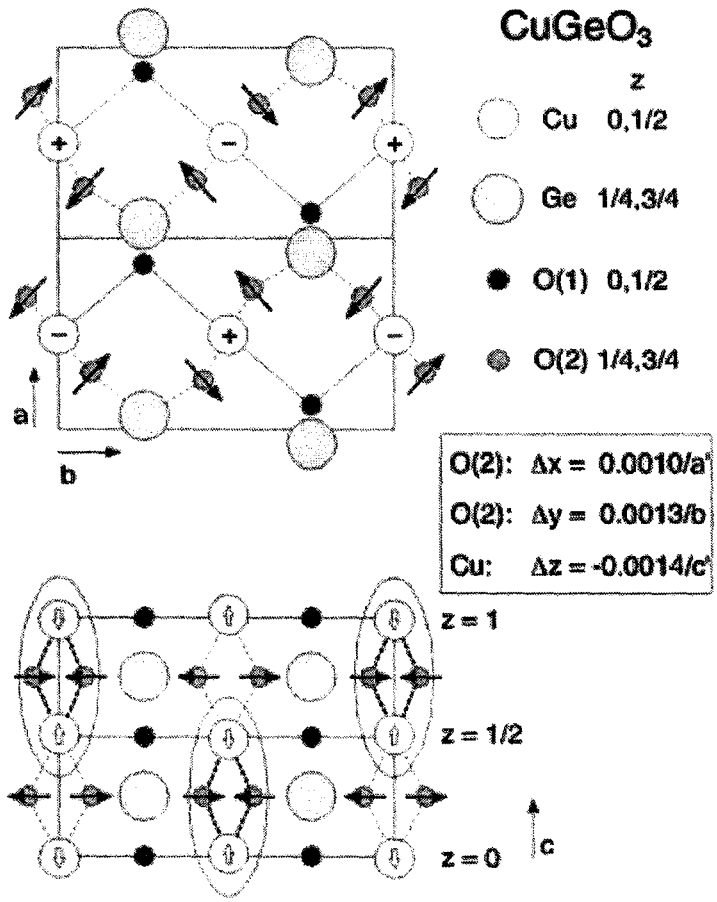

Figure 3.5: Schematic representation of the low-temperature structure for $CuGeO_3$ in the SP state. The rectangles show the unit cell for the high-temperature structure. The cell becomes doubled in the *a* and *c* directions below T_{sp}. Arrows and signs indicate the directions of dis-placements (Hirota *et al.* 1994).

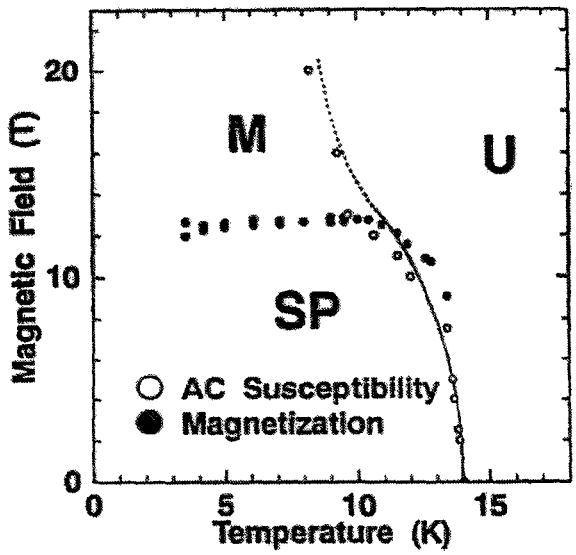

Figure 3.6: The magnetic phase diagram of $CuGeO_3$. (Hamamoto *et al.* 1994)

3.4. Spin–Peierls transition in doped $CuGeO_3$:

All the known SP systems prior to the discovery of $CuGeO_3$ in 1993 were composed of large and complex organic molecules which did not accept dopant ions into their systems so there had been no work done to study the effect of doping on the SP phase transition. $CuGeO_3$, in contrast, readily accepts impurities on both the Cu^{2+} site and on the Ge^{4+} site. This provided the possibility for experimentalists to explore the doping effect on $CuGeO_3$.

The effect of substituting nonmagnetic Zn^{2+} ions ($S = 0$) for Cu^{2+} ions ($S = 1/2$) was investigated by Hase *et al.* (1993b). They observed that the SP transition temperature

decreased with increasing Zn concentration x in $Cu_{1-x}Zn_xGeO_3$, while the magnitude of the susceptibility at low temperatures increased with x. Most prominently they found out that a new phase appears below T_{sp}. The phase was first assigned to a spin-glass state (Hase *et al.* 1993b), but it turned out later that the correct phase is antiferromagnetic (Oseroff *et al.* 1995, Hase *et al.* 1995, Hase *et al.* 1996). In 1995, Oseroff *et al.* tried doping for the Ge^{4+} site and they observed the same phenomena seen while doping for the Cu^{2+} site. Neutron diffraction (Hase *et al.* 1996) of $Cu_{0.966}Zn_{0.034}GeO_3$ also showed magnetic Bragg reflections below a characteristic temperature T_N (Figure 3.7). In addition, it was determined that the spin structure was such that the magnetic moments were arranged antiparallel along the b and parallel along the a-axis. This configuration is consistent with the signs of the exchange interactions achieved in pure $CuGeO_3$ (Nishi *et al.* 1994).

It is now recognized that at sufficiently low temperatures, AF long-range order (AFLRO) occurs in $CuGe_{1-y}Si_yO_3$ (Renard *et al.* 1995) and $Cu_{1-x}M_xGeO_3$ where M = Zn (Hase *et al.* 1993b, Oseroff *et al.* 1995, Hase *et al.* 1995, Hase *et al.* 1996, Lussier *et al.* 1995), Ni (Oseroff *et al.* 1995, Lussier *et al.* 1995, Koide *et al.* 1996, Koide *et al.* 1998), Mn (Oseroff *et al.* 1995). The nature of this AF phase in not fully understood, but the important point is that this phase has unusual features. One of these is the coexistence of the AFLRO and the LRO of the dimerization due to the SP transition in the low-concentration region.

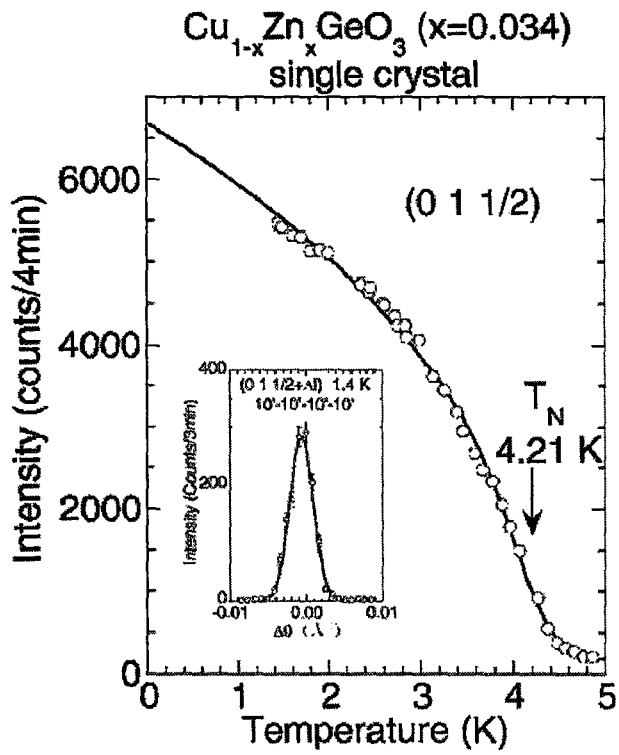

Figure 3.7: The temperature dependence of the intensity of the magnetic Bragg peak at (0, 1, 1/2) in single-crystal $Cu_{0.966}Zn_{0.034}GeO_3$. Inset: a profile of the (0, 1, 1/2) peak at 1.4 K is shown (Lusseir *et al.* 1995).

Masuda *et al.* (1998) showed a new feature of the impurity-induced AF phases and the relation between the dimerization and AFLRO. According to this study, there are two kinds of AF phase in $Cu_{1-x}Mg_xGeO_3$ as a function of Mg concentration x. One of them is the dimerized antiferromagnetic (D-AF) phase, which has the dimerization of the lattice and the AFLRO at the same time. The other is the uniform antiferromagnetic (U-AF) phase, in which, it is claimed, only the AFLRO exists and the dimerization is absent (or the dimerization has only short-range order). There is a first-order phase transition

between these phases. The critical concentration x_c for this first-order transition was reported to be near 0.023 (Masuda *et al.* 1998).

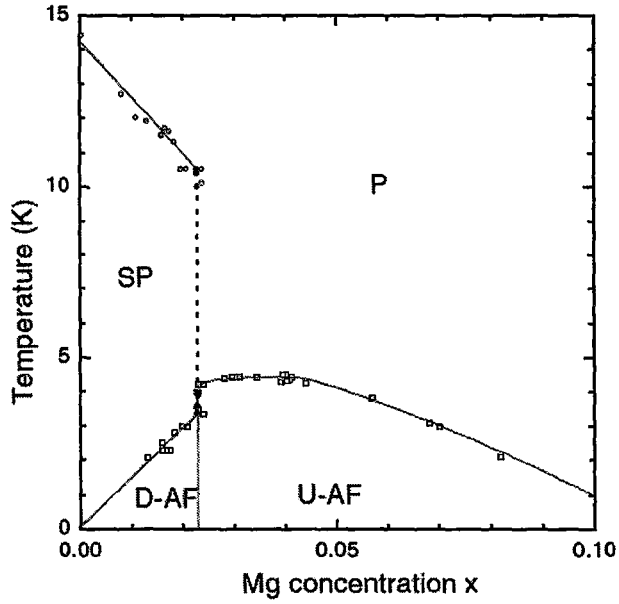

Figure 3.8: The $T - x$ phase diagram of $Cu_{1-x}Mg_xGeO_3$. At $x = 0.023$ a jump of T_N and sudden disappearance of T_{sp} are observed (Masuda *et al.* 1998).

3.5. Critical phenomena at the spin-Peierls transition:

3.5.1. Previous Experiments:

Pure $CuGeO_3$:

Prior to Lumsden *et al.* (1998a), various measurements of the critical phenomena associated with the SP transition in pure $CuGeO_3$, produced different values for critical exponents belonging to several universality classes (Harris *et al.* 1994, Sahling *et al.* 1994, Liu *et al.* 1995, Fujita *et al.* 1995, Saint Paul *et al.* 1995, Harris *et al.* 1995, Winkelmann *et al.* 1995, Lorenz *et al.* 1997, Moncton *et al.* 1977, van Bodegom *et al.* 1981). In 1998, Lumsden *et al.* carefully examined the temperature dependence of the (1/2, 5, 1/2) superlattice peak intensity using X-ray diffraction to measure the order parameter associated with the SP transition in $CuGeO_3$, which is shown in Figure 3.9.

The solid line in this figure represents the best fit using the modified power law. This fit yields an exponent β of 0.35 ± 0.03 at a transition temperature of 14.05K ± 0.01K (Lumsden *et al.* 1998a). The value of β obtained from these measurements is consistent with conventional 3D behavior. This strongly supports the theoretical work by Plumer (1996), where the displacements of both Cu and O are taken into consideration, and predicts 3D *XY* universality for which β has been estimated theoretically to be 0.346 ± 0.002 (le Guillan and Zinn-Justin 1980).

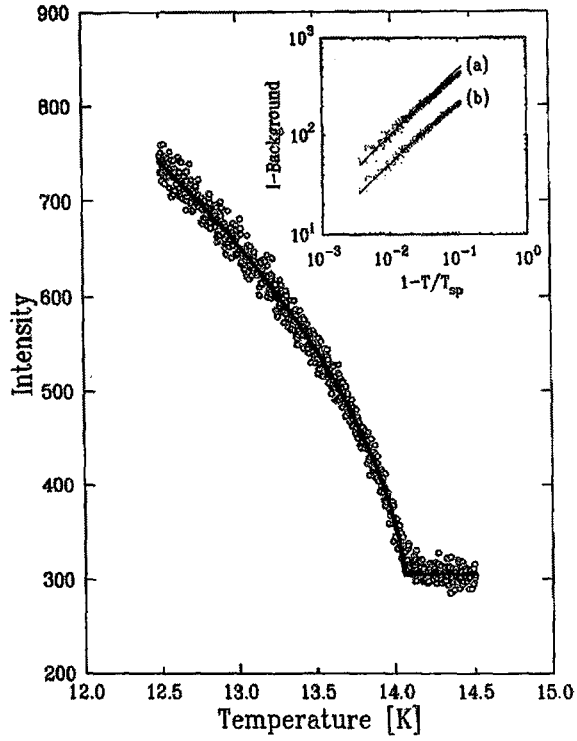

Figure 3.9: X-ray-scattering peak intensity of the (1/2, 5, 1/2) superlattice reflection as a function of temperature (Lumsden *et al.* 1998a).

Doped $CuGeO_3$:

Lumsden *et al.* (1998b) performed X-ray diffraction measurements on samples with three different dopant ions, Zn^{2+} and Cd^{2+} replacing Cu^{2+}, and Si^{4+} substituted for Ge^{4+}. The ionic radius of Zn^{2+}, Cd^{2+}, Cu^{2+} and Si^{4+} and Ge^{4+} are 0.74, 0.97, 0.72, 0.42 and 0.52 Å respectively (Weast 1981). Thus, Si^{4+} represents a smaller dopant ion, Zn^{2+} a dopant ion of roughly the same size, and Cd^{2+} a substantially larger dopant ion.

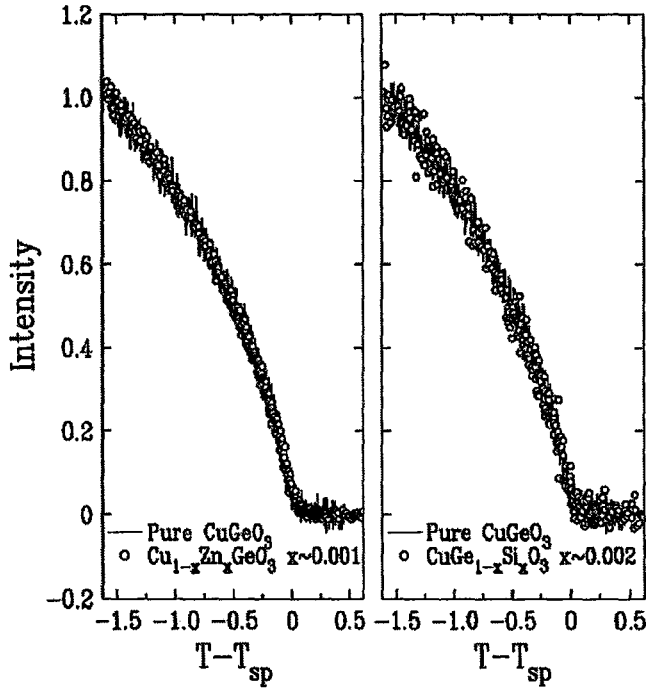

Figure 3.10: Peak intensity data plotted as a function of temperature for $Cu_{1-x}Zn_xGeO_3$ with $x \sim 0.001$ and $CuGe_{1-x}Si_xO_3$ with $x \sim 0.002$. (Lumsden *et al.* 1998b)

Figure 3.10 shows the results for the Zn and Si-doped samples observed by Lumsden *et al.* (1998b) for which peak intensity data are plotted as a function of $T - T_{sp}$ and are normalized to unity at $T - T_{sp}$ = -1.5K. The left panel shows the results for 0.1% Zn-doped sample overlaid on the results from the pure sample and the right panel shows the same result for the 0.2% Si-doped sample. In both cases excellent agreement with the pure data was observed indicating critical behavior very similar to that obtained for the pure compound. The only compound which showed deviation from the data obtained for the pure material was that for the Cd-doped sample as shown in Figure 3.11.

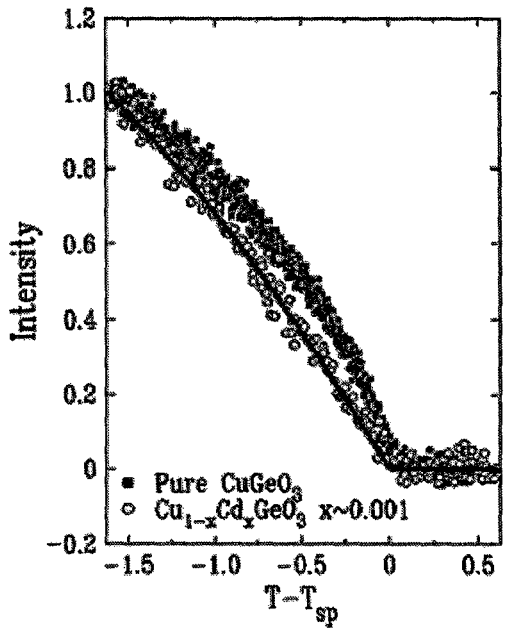

Figure 3.11: Peak intensity data plotted as a function of temperature for $Cu_{1-x}Cd_xGeO_3$ with $x \sim 0.001$ (Lumsden *et al.* 1998b).

The data for the Cd-doped sample shows clear deviation from the pure data over the entire investigated temperature range and the intensity seems to be exhibiting linear behavior over this range suggesting a value of the exponent β consistent with mean field behavior. Lumsden *et al.* (1998b) examined the behavior of the best fit values of β as a function of the lowest temperature (relative to T_{sp}) and compared it with the theoretical expectations for the 3D XY universality. They observed that the Cd-doped data was described by a value of about 0.5 for β, which is consistent with mean field theory. The

results for the Zn-doped and Si-doped samples showed the values for the exponent β, which were very consistent with the results obtained for the pure compound.

This difference between β obtained for the Cd-doped sample and those of the pure compound as well as Zn and Si doped samples was strong motivation for further studies on the Cd-doped $CuGeO_3$ by means of X-ray diffraction and neutron scattering techniques. The goal was to extend previous measurements and investigate the critical behavior of this material with direct measurements of the gap excitation as a function of temperature.

In what follows, I will focus on our recent results obtained from these measurements on a new single crystal of Cd-doped $CuGeO_3$.

3.5.2. Experimental Details:

Sample Preparation:

A single crystal of $Cu_{1-x}Cd_xGeO_3$ with small x was grown from a self-flux by floating zone image furnace techniques. Neutron diffraction measurements performed on the sample at the Chalk River facilities revealed a high quality single crystal throughout its volume with a mosaic spread of about 0.4 degree.

A small piece of this crystal was used for magnetic characterization with SQUID magnetometer, and the characteristic falloff of the dc susceptibility near 14K was observed. Figure 3.12 shows the comparison of dc susceptibility measurements

performed on pure and Cd-doped samples. As it can be seen in this figure, both pure and Cd-doped samples have very similar T_{sp} values, indicating that there is a very low concentration of Cd present in the diluted compound.

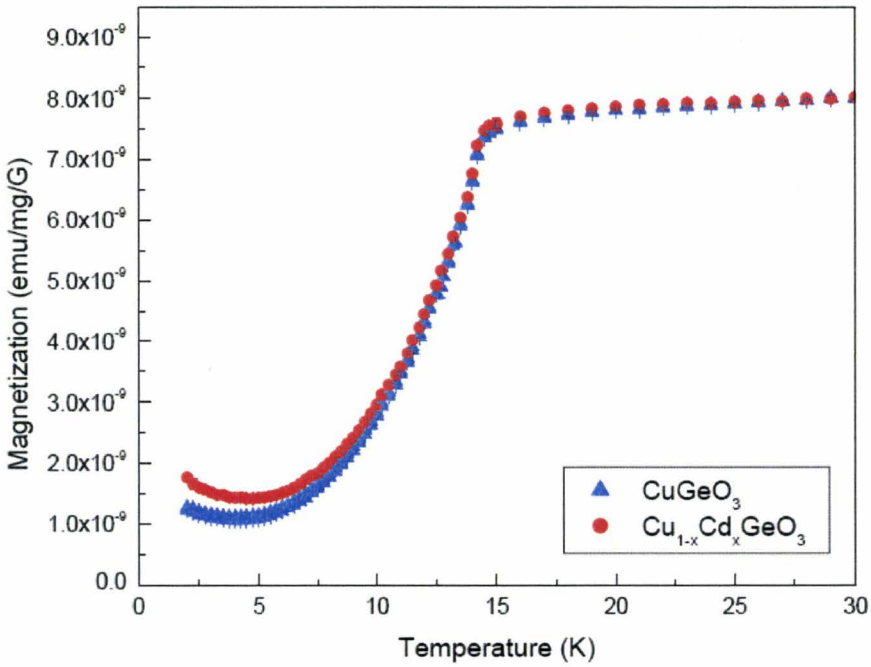

Figure 3.12: Susceptibility measurements for $CuGeO_3$ and $Cu_{1-x}Cd_xGeO_3$.

X-ray Diffraction Measurements:

The X-ray diffraction experiments were performed on a piece of crystal cut from the very high quality single crystal of $Cu_{1-x}Cd_xGeO_3$ with small x, grown by the floating zone technique. The incident X-ray beam was Cu K_α radiation from an 18 KW rotating

anode generator. The (0.5, 5, -0.5) superlattice reflection was examined for the order parameter analysis in order to provide comparable results with previous measurements performed by Lumsden *et al.* on pure (1998a) and Cd-doped (1998b) samples. Initially this reflection was chosen due to its relative strength when compared to other possible reflections, which is known to be reduced in intensity by a factor of ~ 10^{-4} when compared to principal Bragg peaks.

3.5.3. Results and Discussions:

The temperature dependence of the (0.5, 5, -0.5) superlattice Bragg peak was examined in order to measure the order parameter associated with the SP transition in the single crystal of $Cu_{1-x}Cd_xGeO_3$. Figure 3.13 illustrates the temperature dependence of the (0.5, 5, -0.5) supperlattice peak. It can be seen that the peak intensity vanishes at some finite temperature about 14K, very close to T_{sp} for the pure material (Hase *et al.* 1993a, Nishi *et al.* 1995, Fujita *et al.* 1995), and the intensity seems to be exhibiting linear behavior for temperatures within 0.5K of transition temperature. Thus the asymptotic behavior of the order parameter appears to be linear suggesting a value of the exponent β consistent with the mean field theory, i.e. $2\beta = 1$ (Plischke and Bergersen 1989). These results are in agreement with the ones previously reported by Lumsden *et al.* (1998b), although the Cd-doped $CuGeO_3$ samples were different. The single crystal sample used in

this study was grown using floating zone technique while the one used by Lumsden *et al.* was grown using flux method.

In order to determine the critical behavior of the order parameter, the measured data was fit to a power law in the reduced temperature $t = 1 - T/T_{sp}$:

$$Intensity = I_0 t^{2\beta} + Backgound \tag{3.1}$$

This power law is expected to be valid in the so-called asymptotic critical region, near T_{sp}, where the length scale associated with fluctuations in the order parameter dominates over all other relevant length scales in the system. As one moves below the asymptotic region in temperature, the expected power-law behavior must be modified (Aharony and Ahler 1980), as shown in Equation 3.2:

$$Intensity = I_0 t^{2\beta}(1 + At^{\Delta}) + Backgound \tag{3.2}$$

where the exponent Δ has an approximate value of 0.5 (Aharony and Ahler 1980).The solid line shown in Figure 3.13 is the result of such a fit to our data. This fit yields an exponent β of 0.45 ± 0.02 at a transition temperature of 14.2K ± 0.05K.

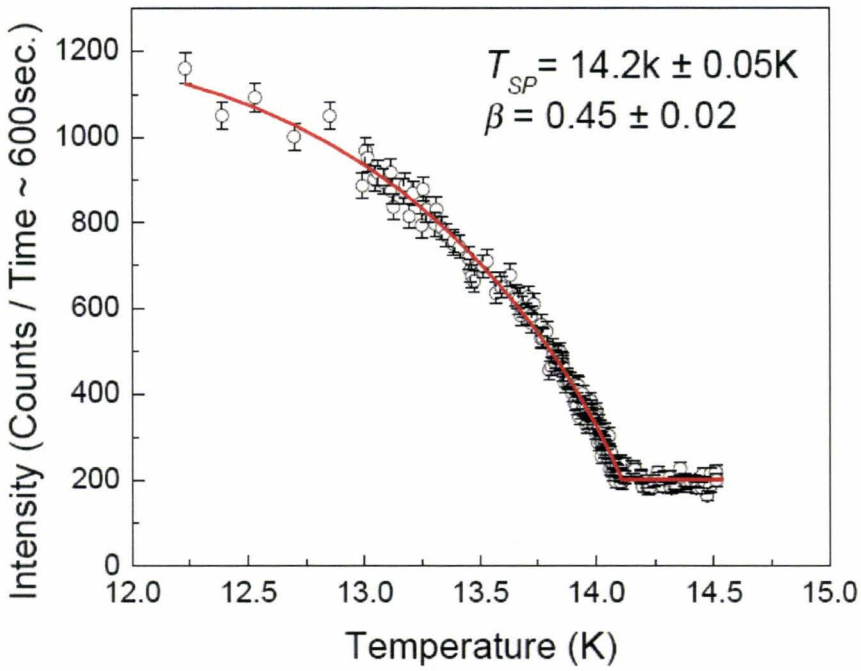

Figure 3.13: Peak intensity as a function of temperature for $Cu_{1-x}Cd_xGeO_3$.

By comparing these results with the ones for Zn- and Si-doped samples achieved by Lumsden *et al.* (1998b), it is clear that the critical behavior for Cd-doped sample is consistent with the mean field behavior ($\beta = 0.5$) while the critical behavior for the pure compounds as well as the Zn and Si doped materials are in agreement with the 3D XY behavior.

3.6. Inelastic Scattering Studies of $Cu_{1-x}Cd_xGeO_3$:

3.6.1. Previous Experiments on Pure $CuGeO_3$:

Previous inelastic neutron scattering measurements, performed on pure $CuGeO_3$ by Regault *et al.* (1996), confirmed the existence of a gap with $\Delta \sim 2$meV in the magnetic excitation spectrum at $T_{sp} = 14.2\text{K} \pm 0.2\text{K}$, associated with the antiferromagnetic zone center $k_{AF} = (0, 1, 1/2)$.

It is known that AF long-range order (AFLRO) can occur in diluted $CuGeO_3$ at very low temperatures and when the concentration of impurity is low this antiferromagnetic phase coexists with the SP phase (Hase *et al.* 1994, Uchinokura *et al.* 1995, Renard *et al.* 1995, Hase *et al.* 1996). Thus, we wanted to study the spin gap excitation of the Cd-doped $CuGeO_3$ as a function of temperature, and to investigate possible antiferromagnetic long range ordering in this compound.

3.6.2. Experimental Details:

Sample Preparation:

The large single crystal of diluted $CuGeO_3$ doped with low concentration of Cd was used for these inelastic neutron scattering measurements.

Inelastic Neutron Scattering Measurements:

The crystal was mounted in a magnet cryostat and the temperature ranged from 0.32K to 25K. The sample was aligned such that the (0, *K*, *L*) plane of the crystal was coincident with the horizontal scattering plane. The inelastic neutron scattering experiments were performed on a single crystal of $Cu_{1-x}Cd_xGeO_3$ with small x using the N5 triple axis spectrometer with a fixed final energy of 3.52 THz at the Chalk River Laboratories. Pyrolytic graphite crystals were used for both monochromator and analyzer, and two Pyrolytic graphite filters were used in the scattered beam in order to reduce the influence of $\lambda/2$ and $\lambda/3$ contaminations at (0, 1, 0.5) point.

3.6.3. Results and Discussions:

In this study, a series of neutron scattering for Cd-doped $CuGeO_3$ were measured at the magnetic zone center k_{AF} = (0, 1, 0.5) as a function of temperature. Our motivation for conducting these measurements was to investigate any possible antiferromagnetic long range ordering (AFLRO) in this material. However, no such evidence of the AFLRO was observed down to 0.32K. This could be due to insufficient concentration of Cd in the sample. It is also possible that 0.32K is not a sufficiently low temperature and that Néel temperature is even lower. In addition, we were intrigued to investigate the excitation energy of the system, Δ, as a function of the order parameter δ. This relationship is

predicted by theory to be in the form of $\Delta \sim \langle\delta\rangle^{\nu}$ in which $\nu = 2/3$ (Cross and Fisher 1979).

The collected data was analyzed in order to determine triplet excitation and damping as a function of temperature and order parameter. A total of four different scenarios were considered for this analysis. These cases are the combinations of two different theoretical models (i.e. Lorentzian and Damped Harmonic Oscillator) and two different possible backgrounds. The two backgrounds are estimated using the low (4K) and the high (21K) temperature data sets and, for simplicity, will be referred to as LT and HT background, respectively.

For the background estimated using a low temperature (4K) data set (i.e. LT), it is assumed that all magnetic scattering is in the sharp peak centered at about 2 meV as shown in Figure 3.14(a). Therefore the non-magnetic part of the spectrum can be readily extracted from the data, which is used as background for other temperatures. For the background estimated using a high temperature (21K) data set (i.e. HT), it is assumed that there are no significant magnetic contributions to the scattering measurements as shown in Figure 3.14(b). Therefore the entire spectrum can be used as background for other temperatures. The quality of these assumptions can be assessed using Figure 3.15, which shows the temperature scan for constant energy $\nu = 0.1$ THz at $Q = (0, 1, 0.5)$. The solid line in the figure is guide to the eye.

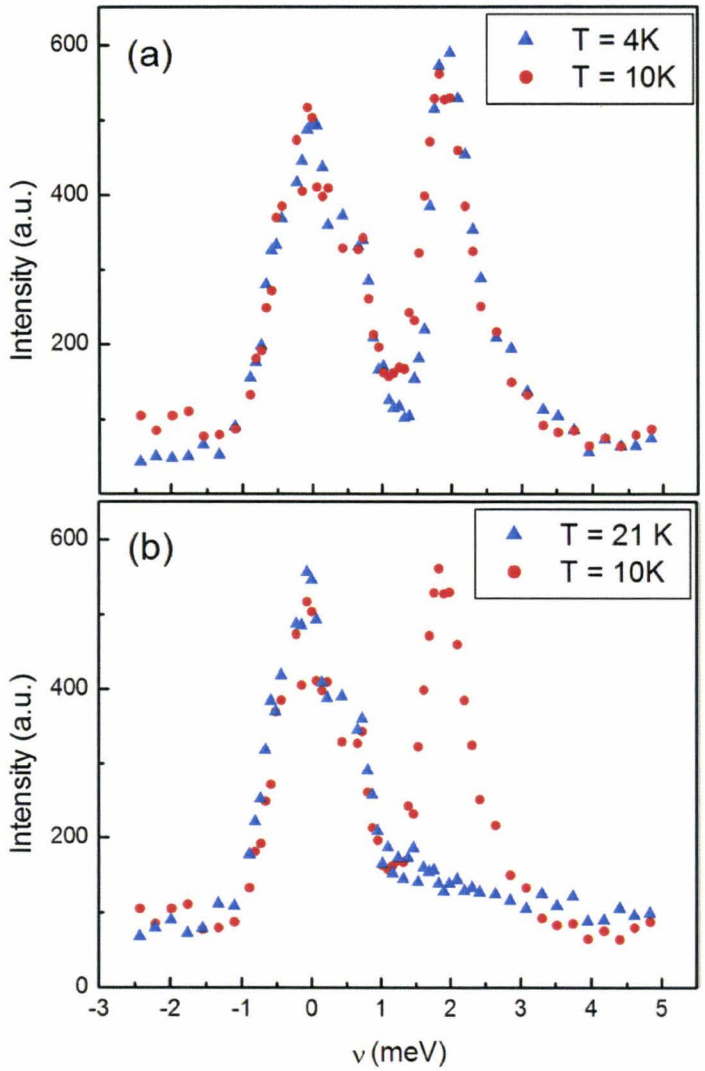

Figure 3.14: The comparison between (a) T=4K and T=10K, (b) T=21K and T=10K data sets at Q = (0, 1, 1/2).

Additional high resolution neutron scattering measurements were performed on the sample in order to make sure that there is no temperature dependence feature in the

quasi-elastic peak and it is safe to systematically subtract it from the various energy scans, in order to obtain the purely magnetic part of the signal.

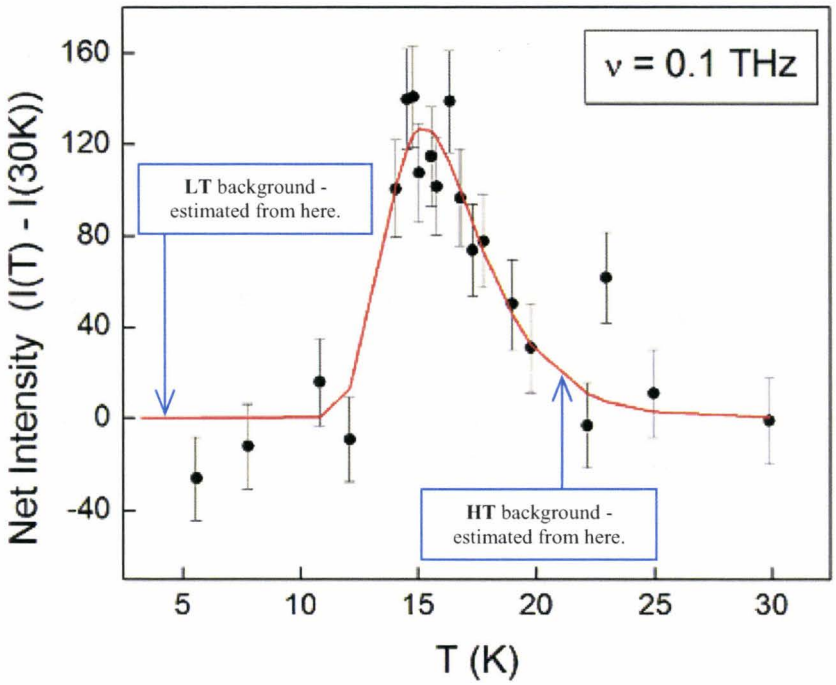

Figure 3.15: The temperature scan for constant energy ν = 0.1 THz at Q = (0, 1, 0.5). The solid line is a guide to the eye.

The experimental data at finite temperatures has been analyzed using two different scattering functions: A Lorentzian function which was used previously by Regnault *et al.* (1996) for analyzing pure $CuGeO_3$ and a Damped Harmonic Oscillator function. The Lorentzian function used in the analysis is in the following form:

$$S(k_{AF},\omega) \sim \frac{S_0}{\Gamma} \frac{\omega}{1-\exp\left(-\frac{\omega}{kT}\right)} \left[\frac{1}{1+\left(\frac{\omega-\Delta}{\Gamma}\right)^2} + \frac{1}{1+\left(\frac{\omega+\Delta}{\Gamma}\right)^2} \right] \quad (3.3)$$

where S_0 is a normalization factor and Γ the damping parameter. The Damped Harmonic Oscillator function employed in the analysis is described by the following equation:

$$S(Q,\omega;T) = \chi(Q,T) \frac{1}{1-\exp\left(-\frac{\omega}{kT}\right)} \left\{ \frac{4\omega\Gamma_{Q,T}/\pi}{\left(\omega^2-\Omega_{Q,T}^2\right)^2 + 4\omega^2\Gamma_{Q,T}^2} \right\} \quad (3.4)$$

where Ω_Q is the renormalized DHO frequency:

$$\Omega_{Q,T}^2 = \omega_{Q,T}^2 + \Gamma_{Q,T}^2 \quad (3.5)$$

$\omega_{Q,T}$ is the oscillator natural frequency, and $\Gamma_{Q,T}$ is a damping parameter. $\chi(Q,T)$ is the wavelength dependent susceptibility and is treated as normalization constant during the fitting procedure.

In the fitting procedure, the functions given by Equations 3.3 and 3.4 have been convoluted with the instrumental resolution function. I have used a MatLab based program, ResLib, in order to calculate the resolution function using the appropriate experimental condition and convoluted the model with the resolution. This convolution was then fit to the data. It is important to note that although the experiment was performed at constant Q = (0, 1, 0.5), the finite instrumental resolution will make a range of relevant Q values concentrated on Q = (0, 1, 0.5). Therefore, it is necessary to include

the dispersion relation in the resolution convolution calculations. The dispersion relation near the magnetic zone center used in the analysis is described by the following equation:

$$\omega_{Q,T} = \sqrt{\Delta_T{}^2 + (v_a q_a)^2 + (v_b q_b)^2 + (v_c q_c)^2} \qquad (3.6)$$

where q_i are the components of the reduced wave vector from k_{AF} and v_i are the spin wave velocities. The values of the spin-wave velocities along different directions were measured by Regnualt *et al.* (1996).

Figures 3.16 and 3.17 illustrate corrected experimental data obtained at temperatures T = 10K, 13K ($T < T_{sp}$), T = 14K ($T \sim T_{sp}$) and T = 15.5K ($T > T_{sp}$) for both backgrounds (HT and LT) as well as both theoretical models (Lorentzian and DHO), as were discussed earlier. The solid lines shown in Figures 3.16 and 3.17 are the results of the resolution convoluted fits. χ^2 analysis shows the high quality of these fits and that both models represent the line-shape of the data quite well. The analysis also reveals that DHO model provides a slightly better fit for the data. It is clear from these figures that as the temperature increases, the gap energy decreases and the peak broadens in energy. It is also apparent that the collapse of the gap energy, which signifies the spin-Peierls transition, occurs at about 14K; approximately at about the same SP transition temperature for pure $CuGeO_3$ compound (Regnault *et al.* 1996).

The best fits of the experimental data result in a set of parameters, Δ (energy gap) and Γ (damping), versus T. The temperature dependence of these parameters using both models (Lorentzian and DHO) for data sets employing the two possible backgrounds (LT and HT) are presented in Figure 3.18. It can be seen in this figure that the gap value starts

to decrease only above 11K, whereas the damping increases rapidly in the neighborhood of T_{sp}. This is in agreement with previous inelastic neutron scattering experiments performed on the pure compound (Regnualt *et al.* 1996). Looking at Figure 3.18, one can also determine the phase transition temperature. This temperature can be identified as the intersection of the gap excitation and the damping parameter. It can also be seen that the DHO model results in higher values for gap energy comparing to the Lorentzian model. However, the results from Lorentzian model are in closer agreement with the previous results for pure compound reported by Regnault *et al.* (1996).

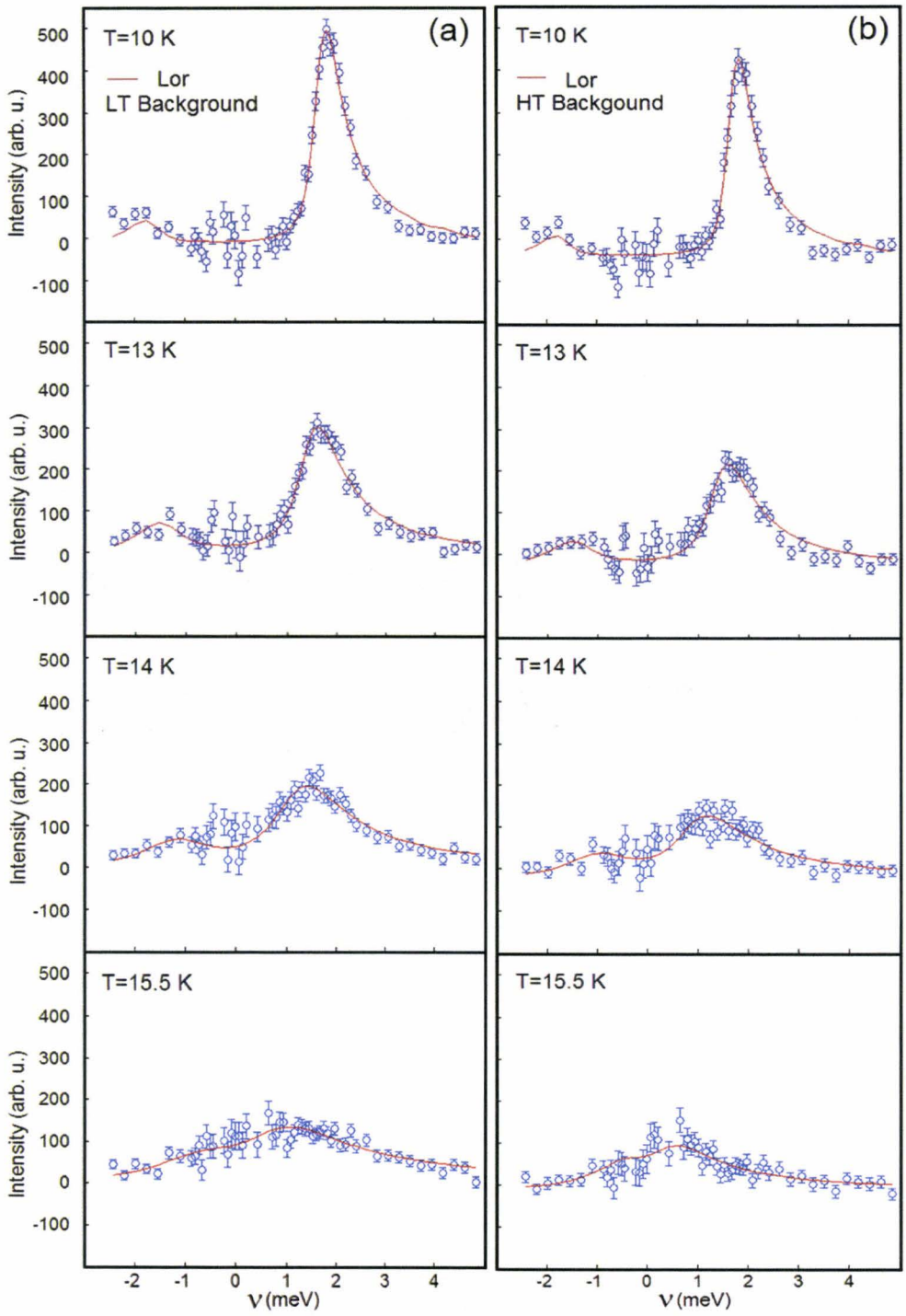

Figure 3.16: Constant-Q scans at Q = (0, 1, 0.5) for various temperatures for (a) LT and (b) HT background subtracted data sets. In both cases, the solid lines are fits using Equation 3.3 as described in the text.

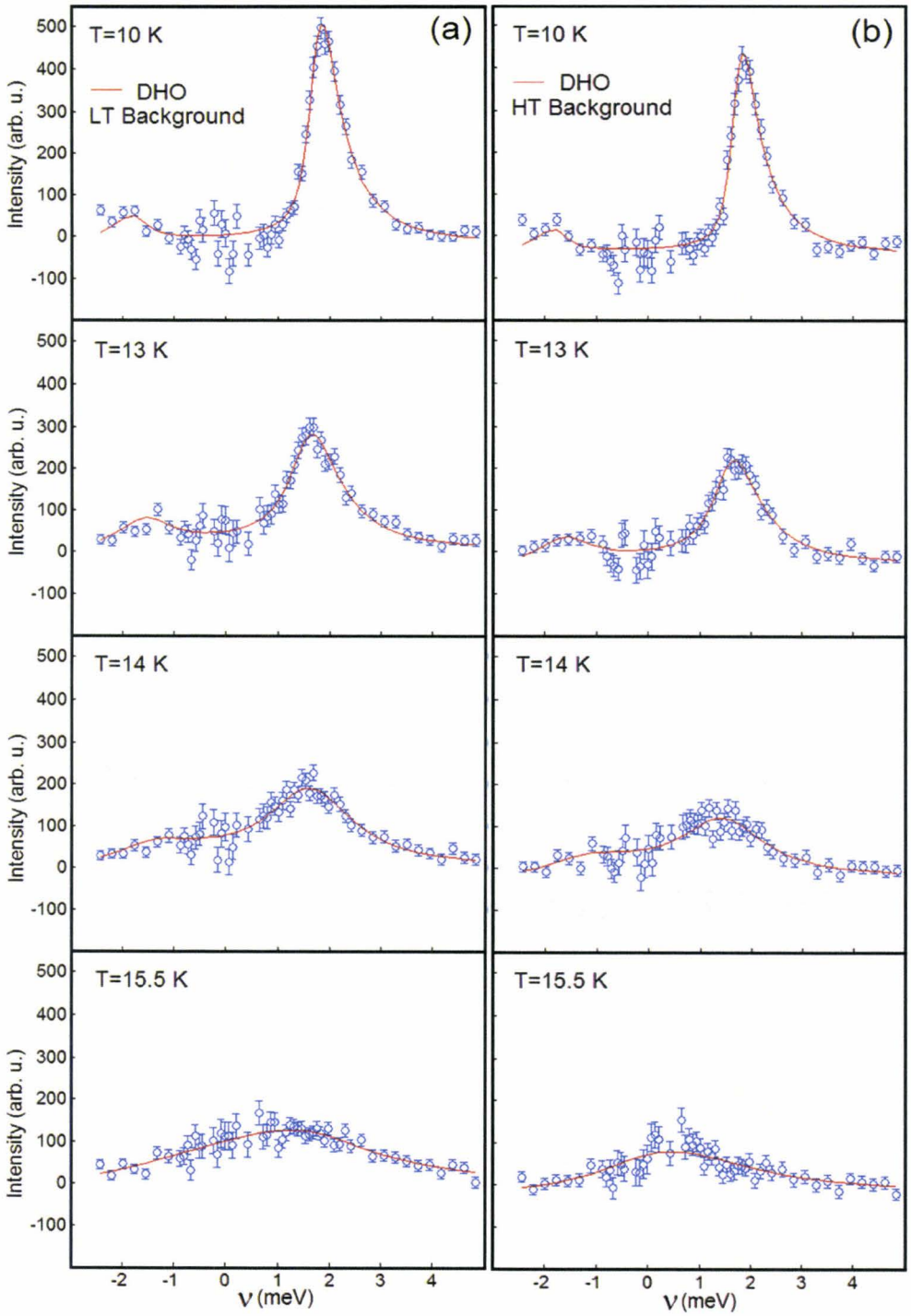

Figure 3.17: Constant-Q scans at Q = (0, 1, 0.5) for various temperatures for (a) LT and (b) HT background subtracted data sets. In both cases, the solid lines are fits using Equation 3.4 as described in the text.

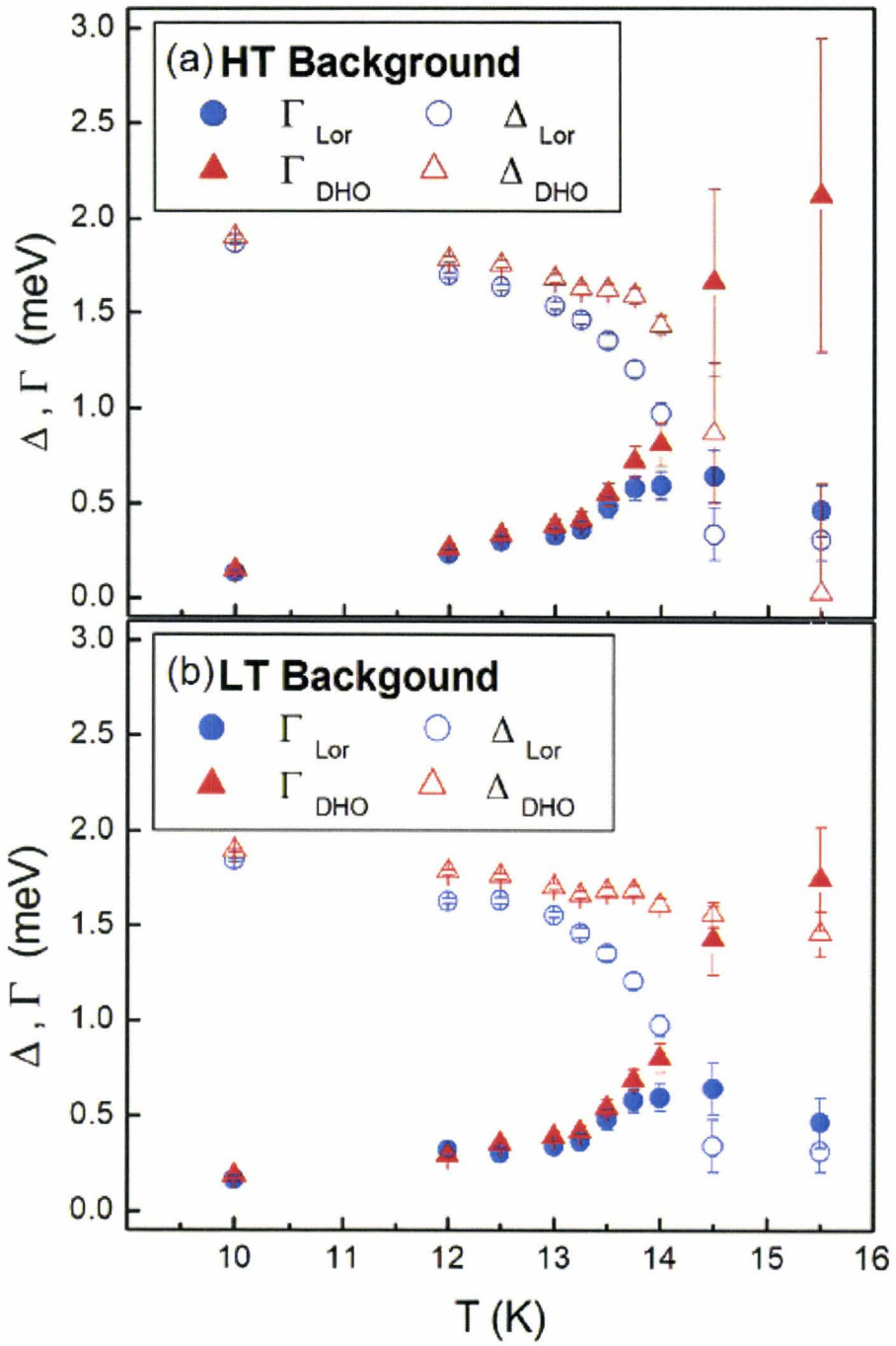

Figure 3.18: Temperature dependence of the gap energy (Δ) and damping parameter (Γ) for (a) HT and (b) LT background subtracted data sets comparing the two theoretical models described in the text.

From the theoretical point of view, the relation between the gap energy and the order parameter have been predicted to be a power-law relation of type $\Delta(T) \propto \left(\langle\delta\rangle_T\right)^{\nu}$, with values of ν ranging from 2/3 to 1, depending on the model or approach used (Pytte 1974, Cross and Fisher 1979). Recent numerical calculations have given value of ν = 0.69 ± 0.01 (Regnault *et al.* 1996). Previous inelastic neutron scattering measurements conducted by Regnault *et al.* (1996) also indicated ν ~ 2/3. One of the key components of the analysis was to examine this relationship. The main test was obtained from a plot of the gap energy value $\Delta(T)$ versus $\sqrt{I(T)}$ for $T < T_{sp}$. Here, $I(T)$ is the intensity of a superlattice peak measured at temperature T, which was obtained from X-ray diffraction measurements and is related to the order parameter $\langle\delta\rangle_T$ by $I(T) \propto \left(\langle\delta\rangle_T\right)^2$ (Cross and Fisher 1979). This allows us to experimentally determine the relationship between $\Delta(T)$ and $\langle\delta\rangle_T$ for the Cd-doped sample, and compare it with the previous results obtained for pure sample by Regnault *et al.* (1996).

Figures 3.19 and 3.20 show the relation between the gap energy and the normalized order parameter for both models for LT and HT backgrounds. In order to produce these plots, I have used the results for the order parameter from the X-ray diffraction experiments performed on the sample along with the fitting results of the gap energy obtained from analyzing the inelastic neutron scattering measurements. In these figures, the solid lines represent fits obtained from the power law Equation 3.7:

$$\Delta(T) = \Delta(0) + \left(\langle\delta_T\rangle\right)^{\nu}_{norm} \tag{3.7}$$

in which, $\Delta(0)$ is the gap energy at $T = 0$ and has a theoretical value of $\Delta(0) = 0$ (Cross and Fisher 1979).

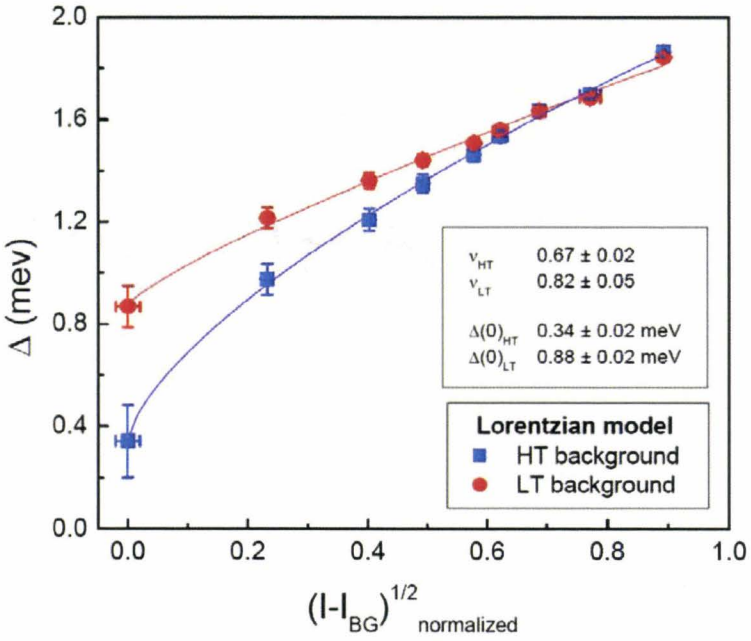

Figure 3.19: Plot of the gap energy Δ as a function of square root of intensity at the point Q = (0, 1, 0.5). The solid lines are the fits to power laws as described in the text for Lorentzian model and both HT and LT backgrounds.

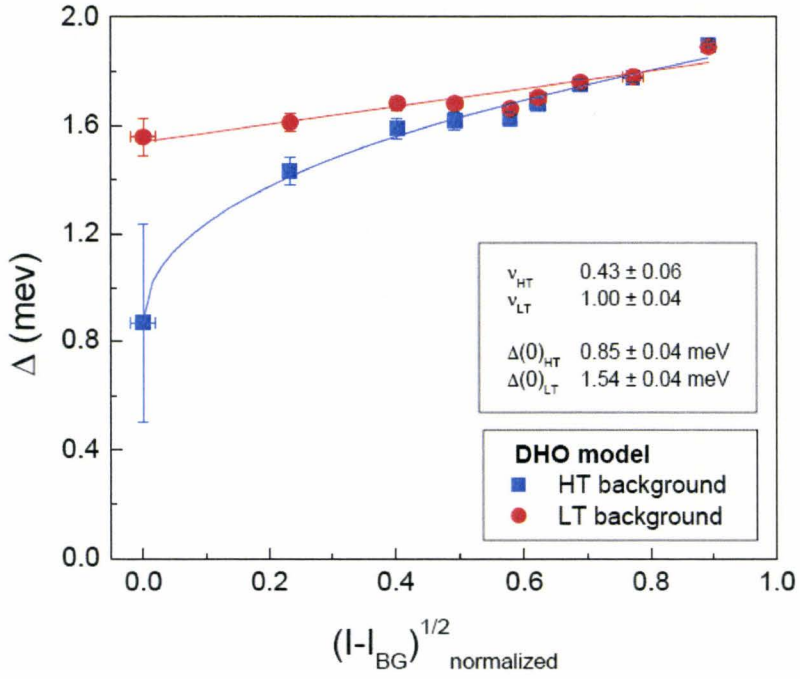

Figure 3.20: Plot of the gap energy Δ as a function of square root of intensity at the point Q = (0, 1, 0.5). The solid lines are the fits to power laws as described in the text for DHO model and both HT and LT backgrounds.

Table 3.1 summarizes the parameters obtained from the fits. It can be seen that for both models, HT background gives a smaller value for ν compared to that obtained from LT background. From the values of Δ(0), one can also conclude that for both models and either background the gap excitation does not go to zero at phase transition, which is not in agreement with the theoretical prediction.

	Lorentzian Model		DHO Model	
	LT BG	**HT BG**	**LT BG**	**HT BG**
ν	0.82 ± 0.05	0.67 ± 0.02	1.00 ± 0.04	0.43 ± 0.06
Δ(0) in meV	0.88 ± 0.02	0.34 ± 0.02	1.54 ± 0.04	0.85 ± 0.04

Table 3.1: Summary of the parameters obtained from Figures 3.19 and 3.20.

3.7. Conclusion:

In this study, a low concentration of Cd was successfully doped into $CuGeO_3$ and a high quality single crystal was grown. Using this single crystal, the temperature dependence of the (0.5, 5, -0.5) superlattice Bragg peak was examined using X-ray diffraction, in order to measure the order parameter associated with the SP transition in $Cu_{1-x}Cd_xGeO_3$. It was observed that the peak intensity of $Cu_{1-x}Cd_xGeO_3$ vanishes at some finite temperature about 14K, which is very close to T_{sp} for the pure material.

The critical behavior of the order parameter of the Cd-doped $CuGeO_3$ was also investigated. For this purpose, the measured data was fit to a power law. This fit resulted

in an exponent β of 0.45 ± 0.02 at a transition temperature of 14.2K ± 0.05K, which is consistent with the mean field behavior (β= 0.5).

In this study, a series of spin-wave spectrums for Cd-doped $CuGeO_3$ at magnetic zone center k_{AF} = (0, 1, 0.5) as a function of temperature were also measured by means of inelastic neutron scattering, looking for possible antiferromagnetic long range ordering in this material. No such evidence of the AFLRO was observed down to a temperature of 0.32K, which could be due to insufficient concentration of Cd in the sample or that the Néel temperature is lower than 0.32K.

A total of four different scenarios were considered for the analysis of the collected data, which are the combinations of two different theoretical models (i.e. Lorentzian and Damped Harmonic Oscillator) and two different possible backgrounds (estimated from low or high temperature data sets, respectively referred to as LT and HT background). Best fit for the data was determined based on resolution convolution calculations. χ^2 analysis showed the high quality of these fits and that both models represent the line-shape of the data quite well, although it was seen that DHO model provides a slightly better fit for the data. It is clear from analysis of the neutron scattering measurements that with increasing temperature, the gap energy decreases and the peak broadens in energy.

The energy gap Δ and damping Γ versus temperature were obtained from the fits to the inelastic neutron scattering data. It was seen that the gap value starts to decrease at above 11K, whereas the damping increases rapidly in the neighborhood of T_{sp}, which is in agreement with previous inelastic neutron scattering experiments performed on the pure compound. It was also seen that the DHO model results in higher values for gap

energy comparing to the Lorentzian model while Lorentzian model provides values closer to the ones previously reported for pure compound.

Finally, the relation between the gap energy and the order parameter was studied. For this purpose the order parameter was calculated as the square roof of peak intensity, obtained from the X-ray diffraction measurements. Four different combinations of backgrounds and theoretical models were considered and in each case, a power law equation was fit to the data. It was observed that for both models, the HT background analysis gives a smaller value for the exponent ν compared to that obtained from LT background. It was also concluded that for both models and either background the gap excitation does not vanish at phase transition, in contrast to the theoretical expectations.

Chapter 4

Neutron Scattering from $SrCu_2(BO_3)_2$:

4.1. Introduction:

Layered quantum magnets have been at the forefront of condensed matter physics research in large part due to their relevance to high temperature superconductivity. Two-dimensional copper-oxides, in which conducting holes are introduced, provide the framework for much exotic behavior, with high temperature superconductivity being the best appreciated example. More broadly, quantum antiferromagnets are of interest because the pattern for their behavior is not the orderly, antiparallel arrangement of magnetic moments in a Néel state, but the formation of singlets in which the magnetic moments lose their spin-up or spin-down identity and reside in a quantum mechanical superposition of both spin-up and spin-down.

Kageyama *et al.* (1999a) discovered a new two-dimensional spin gap system $SrCu_2(BO_3)_2$. A remarkable feature of $SrCu_2(BO_3)_2$ is that the theoretical model for interacting spin 1/2 dimers, which was considered and solved exactly by Shastry and Sutherland in 1981, is appropriate for this system (Miyahara and Ueda 1999).

In this chapter, I will discuss new high-resolution inelastic neutron scattering measurements, which probe both the energy and Q dependencies of the previously identified bands of excitations with new precision. Measurements were performed on two different high-resolution cold neutron instruments, allowing both high energy resolution to resolve the three $n = 1$ triplet excitations in $SrCu_2(BO_3)_2$, and high Q resolution to detect different Q dependencies among the n-triplet excitations, where $n = 1$, 2, and 3. In addition, neutron powder diffraction measurements were performed on a sample to investigate the possibility of a proposed structural phase transition in this compound.

4.2. Structure of $SrCu_2(BO3)_2$:

$SrCu_2(BO_3)_2$ crystallizes (Smith and Keszler 1991) into the tetragonal space group $I\bar{4}2m$ with lattice parameters a =8.995 Å, c = 6.649 Å. The schematic crystal structure is represented in Figure 4.1. As shown on this figure, $SrCu_2(BO_3)_2$ is a layered compound consisting of slightly buckled $Cu(BO_3)$-planes separated by Sr Atoms. Figure 4.2 gives a top-view onto an isolated $Cu(BO_3)$-plane.

The magnetic properties of the crystal are dominated by the $S = 1/2$ spins which are considered to be situated on the Cu^{2+} sites. By geometry we find two Cu^{2+} ions close to each other and we connect them by lines as shown in Figure 4.2. It can be seen that the Cu^{2+}sites are arranged in dimers at right angles to each other and forming a square lattice. The leading terms, in the Hamiltonian which describe how the spin 1/2 magnetic moments interact are given by an intra-dimer antiferromagnetic exchange interaction, J, as well as an inter-dimer exchange interaction, J'. J = 85K and J' = 54K are anti-ferromagnetic interactions estimated from the susceptibility and the gap measurements (Miyahara and Ueda 1999). It was first observed by Miyahara and Ueda in 1999 that a single $Cu(BO_3)$-plane can be mapped onto the Shastry-Sutherland model.

One should also note that every second $Cu(BO_3)$-plane is rotated by $\pi/2$ about one of the dimer centers, so that each dimer has a rotated dimer above and below. Thus the inter-plane exchange interactions are frustrated by the geometry. Since fits to the susceptibility measurements result in weaker inter-plane interactions (Miyahara and Ueda 1999), we will mostly concentrate on the in-plane physics.

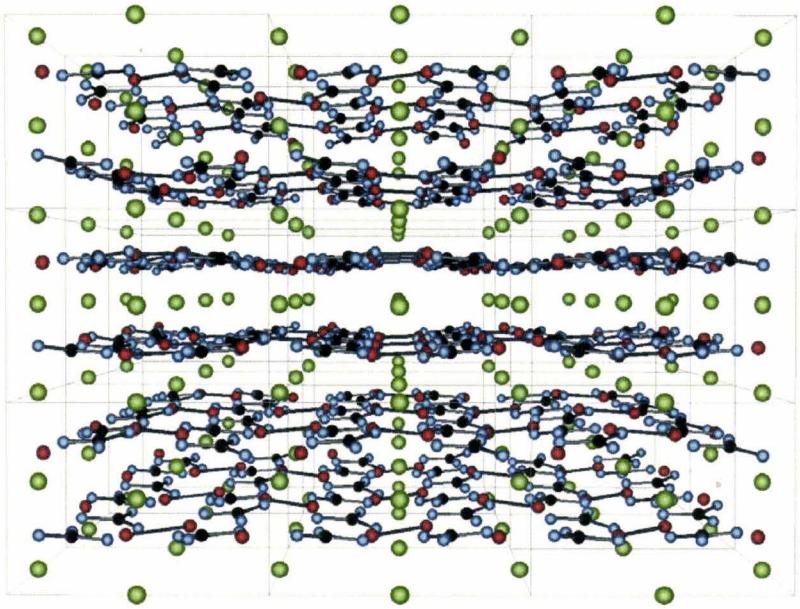

Figure 4.1: Crystal structure of $SrCu_2(BO_3)_2$, which is a layered compound with slightly buckled $Cu(BO_3)$-planes separated by Sr-atoms: green spheres; Cu: red, B: black, O: blue (Knetter *et al.* 2000).

4.3. Theoretical model for $SrCu_2(BO_3)_2$:

In 1999, Miyahara and Ueda introduced the frustrated Shastry-Sutherland model for $SrCu_2(BO_3)_2$ with $S = 1/2$ as shown in Equation 4.1 where *nn* stands for nearest neighbor and *nnn* for next nearest neighbor:

$$H = J\sum_{nn} S_i \cdot S_j + J'\sum_{nnn} S_i \cdot S_j \qquad (4.1)$$

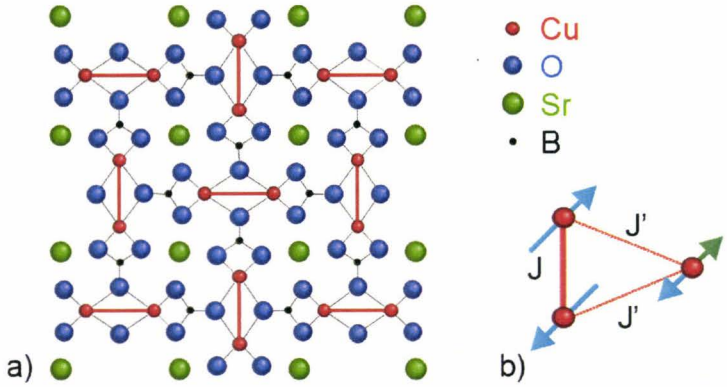

Figure 4.2: (a) A schematic drawing of the basal plane structure of $SrCu_2(BO_3)_2$ is shown. Red atoms joined by red bars highlight the Cu^{2+} dimers. (b) The leading order exchange interactions which shows the nearest-neighbor (*nn*) intra-dimer (*J*) and next-nearestneighbor (*nnn*) inter-dimer (*J'*) antiferromagnetic interactions (Kageyama *et al.* 1999a).

It is known that both interactions, J and J', are antiferromagnetic and similar in strength, such that the system is not far from the critical value of $x = J'/J$ for a quantum phase transition to a four sublattice Néel state (Miyahara and Ueda 1999). In their original work, Shastry-Sutherland (1981) argued that the direct product of the singlet states on J bonds, described by Equation 4.2, is always an eigenstate of the Hamiltonian.

$$|\psi\rangle = \prod_a |s\rangle_a = \prod_a \frac{1}{\sqrt{2}}\left(|\uparrow\downarrow\rangle_a - |\downarrow\uparrow\rangle_a\right) \tag{4.2}$$

In the this equation, a denotes a nearest-neighbor bond.

They also showed that, this eigenstate (Equation 4.2) is the exact ground-state of the Hamiltonian for $J'/J \leq 0.5$. For $J'/J \geq 0.5$, there is no exact solution for this model. Therefore, one can conclude that there is a quantum phase transition at $(J'/J)_c$ greater

than 0.5. For small J'/J the collective singlet state shown in Equation 4.2 is the ground-state, which has a spin gap and does not exhibit long range ordering.

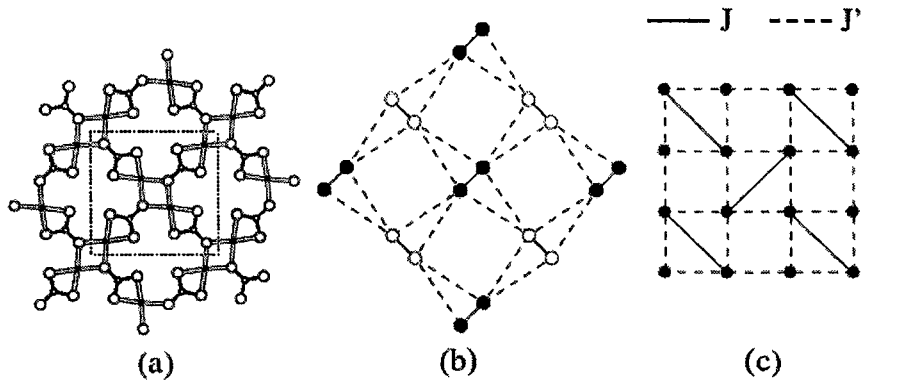

Figure 4.3: (a) Schematic view of the crystal structure of a $CuBO_3$ layer. Full circles represent Cu sites. Big open circles are O sites and small open circles are B sites. The dotted line shows the unit cell (Kageyama *et al.* 1999). (b) Two-dimensional orthogonal dimer model, which is equivalent to (c) the Shastry–Sutherland model (Miyahara and Ueda 2003).

Assuming $J = 0$ and $J' \neq 0$, the model is equivalent to a two-dimensional Heisenberg model. Manousaki (1991) reported that there is a general agreement that the two-dimensional Heisenberg model has antiferromagnetic long-range order ground-state and no spin gap. Therefore, in the limit $J'/J >> 1$, the antiferromagnetically ordered state must be the ground state. Series expansion calculations by Koga and Kawakami (2000) give the phase transition point $(J'/J)_c = 0.68$ associated with this quantum phase transition.

Initially, a direct phase transition from the dimer singlet state to the AF ordered state was proposed (Shastry and Sutherland 1981, Miyahara and Ueda 1999). However,

recent works favor the possibility of an intermediate phase and therefore, in addition to these two states, it is possible that other states also exist between them (Albercht et al. 1996, Chung et al. 2001, Takushima et al. 2001, Läuchli et al. 2002). At present, our picture of the ground state of this orthogonal dimer model is that there may be three phases. Theoretical existence of the dimer singlet state for $J'/J < 1$ and an AF ordered state for $J'/J >> 1$ is established and the nature of the intermediate state in this model remains an open question.

One of the unique features of $SrCu_2(BO_3)_2$ is the very localized triplet excitations which have a tendency to crystallize at high magnetic fields. Recent experiments showed that the triplet excited states split in the presence of magnetic field. Experiments also revealed that the spin triplet excitation energy decreases linearly with increasing magnetic field, which extrapolates to zero at about 20T magnetic field (Cépas *et al.* 2001, Cépas and Ziman 2001, Nojiri *et al.* 2003). However, the experimental data deviates from this linear extrapolation at a finite magnetic field (Jorge *et al.* 2004). This indicates that the magnetic field causes the lowest energy triplet state to cross the ground-state. Consequently, this results in a condensation of the triplets in to the ground-state, and the appearance of magnetization plateaux (Jorge *et al.* 2004).

It has also been shown, both by theory and experiment, that the lowest branch of magnetic excitations in $SrCu_2(BO_3)_2$ has a relatively small bandwidth (Kageyama *et al.* 2000, Weihong *et al.* 1998, Gaulin *et al.* 2004). The experiments conducted in this study, which will be discussed later in this chapter, showed a large bandwidth for the higher energy excitations which may be interpreted as unresolved dispersive excitations.

The inelastic neutron scattering experiments presented in this thesis show that the excitations are not purely local and the triplet states split in zero magnetic field. Cépas *et al.* (2001) argued that the corrections to the Hamiltonian, although small, are necessary and this splitting of the excited states in zero field can be accounted for by considering the Dzyaloshinsky-Moria (DM) interaction, which occurs in low-symmetry crystals, in the Hamiltonian. The contribution from DM interaction term to the Hamiltonian is given by:

$$H_{DM} = \sum_{\langle i \to j \rangle} D \cdot \left(S_i \times S_j \right) + \sum_{\langle i \to j \rangle'} D' \cdot \left(S_i \times S_j \right) \tag{4.3}$$

Here, $\langle i, j \rangle$ and $\langle i, j \rangle'$ indicate that i and j are nearest neighbor and next-nearest neighbor, respectively. The arrows indicate that the corresponding bonds have a particular orientation.

Assuming that the $CuBO_3$ in $SrCu_2(BO_3)_2$ is a mirror plane, there is a center of inversion at the middle of the dimer bond which forbids the DM interaction between nearest neighbors. However, each dimer is separated from the neighboring dimer by a BO_3 triangle for which there is no center of inversion at the middle of the bond. This allows the DM interaction to exist between the next nearest neighbors. It also indicates that the main components of D must be perpendicular to the copper plane (Cépas *et al.* 2001). However since there is a buckling in the copper plane, in the real material at temperatures below 395K the mirror symmetry in this plane is lost (Sparta *et al.* 2001). In this way, in-plane components of the Dzyaloshinsky–Moriya interaction may also exist.

4.4. Inelastic Scattering Studies of $SrCu_2(BO_3)_2$:

4.4.1. Previous Experiments on $SrCu_2(BO_3)_2$:

Kageyama *et al.* (1999b) were the first to publish data on the magnetic response of $SrCu_2(BO_3)_2$. The magnetic susceptibility measured on powder sample shows a maximum at around 20K and a rapid drop towards zero with decreasing temperature, indicating an energy gap in the magnetic spectrum. The temperature dependence of the magnetic susceptibility is shown in Figure 4.4. Kageyama *et al.* (1999b) estimates the value of the spin gap to be $\Delta = 34K \pm 1K$ based on the fit to the isolated dimer model. Various experiments also showed evidence that $SrCu_2(BO_3)_2$ has the spin gap $\Delta \sim 35K$ (Kageyama *et al.* 1999b, Nojiri *et al.* 1999, Kageyama *et al.* 2000a, Lemmens *et al.* 2000). Therefore it is experimentally confirmed that the ground state of this material is nonmagnetic.

Kageyama *et al.* (2000b) later published relatively low resolution inelastic neutron scattering (INS) data obtained from a large single crystal. These measurements have revealed three bands of excitations corresponding to single (n = 1) triplet excitations, as well as to two (n = 2), and to three (n = 3) triplet excitations. These measurements directly showed the appearance of the energy gap in the spectrum of excitations with decreasing temperature, as well as the dispersion of these excitations in an applied magnetic field. Electron spin resonance (Nojiri *et al.* 1999), far infrared studies (Rõõm *et al.* 2000) and nuclear magnetic resonance (Kodama *et al.* 2002) give further evidence for a singlet ground state above which a triplet excitation with gap 2.9 meV can be found.

The more recent studies (Cépas *et al.* 2001, Kakurai 2002) have been able to investigate subleading terms in the spin Hamiltonian. Terms such as the Dzyaloshinski-Moriya (DM) interaction, which is allowed by symmetry between spins on neighboring dimers, can account for both the dispersion of these excitations and the removal of the threefold degeneracy which would otherwise characterize the $n = 1$ triplet excitation spectrum in $SrCu_2(BO_3)_2$. The presence of such small terms in the spin Hamiltonian has also been investigated through high field specific heat measurements (Jorge *et al.* 2004).

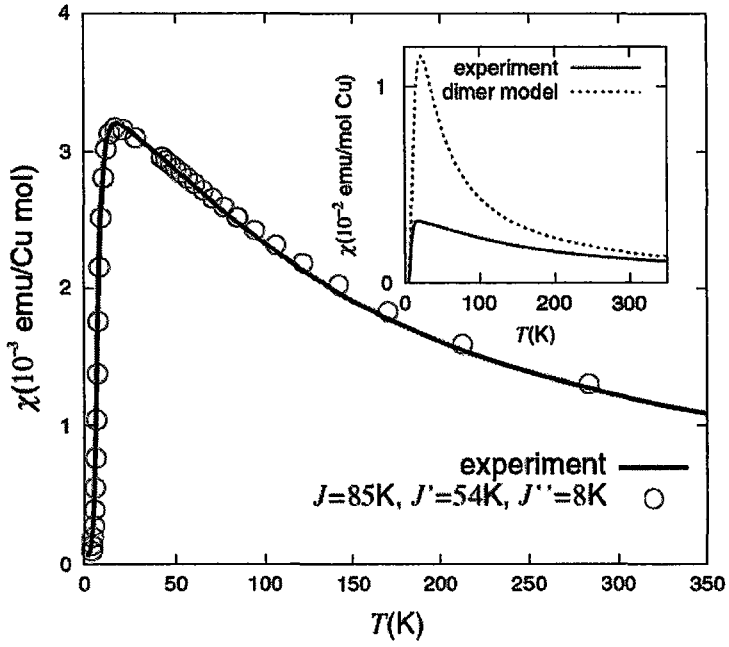

Figure 4.4: The temperature dependence of the magnetic susceptibility (solid curve). Circles are the result of numerical calculation with the optimal parameter set. The inset is the result of fitting by an isolated dimer model (Kageyama *et al.* 1999b , Miyahara and Ueda 1999).

The estimated values of J and J' have evolved over time as both theory and experiment have improved. One can find various fits of the model parameters to the experimental data. The earliest fit by Miyahara and Ueda (1999) gives $x = 0.68$ and $J = 100\text{K} = 8.617\text{meV}$. In a later and improved calculation, they found $x = 0.635$ and $J = 85\text{K} = 7.325\text{meV}$ (Totsuka *et al.* 2001). Other values in this range are for instance $x = 0.664$ and $J = 83\text{K} = 7.15\text{meV}$ (Zheng *et al.* 1999) or $x = 0.65$ and $J = 87\text{K} = 7.50\text{meV}$ (T. Munehisa and Y. Munehisa 2003). The range of given x values is rather close to the critical value of $x_c \approx 0.69$. There are experimental possibilities which may push $SrCu_2(BO_3)_2$ towards the critical value by means of pressure or chemical substitutions. A direct observation of a real substance at or close to a quantum critical point would indeed be very interesting, but has so far not been realized.

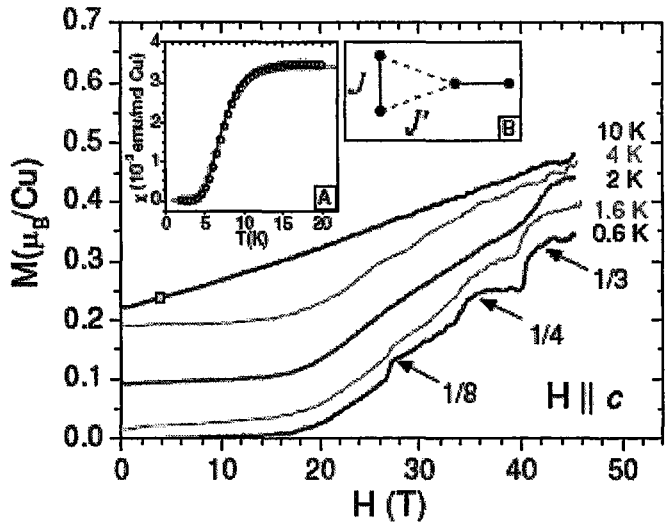

Figure 4.5: Magnetization vs field for $SrCu_2(BO_3)_2$ at different temperatures between 0.6K and 10K. Inset A: Magnetic susceptibility measured at $H = 4\text{T}$ in a SQUID magnetometer and the calculated susceptibility. Inset B: Two copper dimers in the CuBO3 plane where the coupling constants J (*nn*) and J' (*nnn*) are indicated. (Jorge *et al.* 2004)

Much interest has also focused on magnetization plateaus which appear beyond 20T in $SrCu_2(BO_3)_2$ (Kodama *et al.* 2002). Strong magnetic fields generate triplets, within a background of singlets, which can undergo Bose-Einstein condensation (BEC) at densities determined by the applied magnetic field, which takes on the role of a chemical potential. Figure 4.4 shows the high field magnetization measurements which have been performed by Jorge *et al.* (2004). These measurements were performed on the same sample that was used for our neutron scattering experiments which will be discussed later in this chapter. The 1/3, 1/4 and 1/8 platueax were observed in these measurements and are shown in Figure 4.5.

4.4.2. Experimental Details:

Sample Preparation:

The present single crystal of $SrCu_2(^{11}BO_3)_2$ was grown from a self-flux by floating zone image furnace techniques. Stoichiometric amounts of CuO, $SrCO_3$ and B_2O_3 were mixed, preannealed, and then annealed at 870 °C. Finally, the powder was regrinded, pelletized and annealed in O_2 several times. Rods were formed by hydrostatic pressing and the growth was performed in a Crystal System Optical Furnace at a growth speed of 0.25 mm/h in O_2. No additional flux was applied.

The crystal is cylindrical in shape, with approximate dimensions of 0.6 cm in diameter by 10 cm long. Small pieces of the crystal were used for bulk characterization and the characteristic falloff of the dc susceptibility near 10K. Well-defined plateaux in magnetization versus applied magnetic field was observed, which is shown in Figure 4.5 (Jorge *et al.* 2004). Neutron diffraction measurements performed at Chalk River Laboratories, enabled by the use of ^{11}B isotope, revealed a high quality single crystal throughout the volume of the sample with a mosaic spread of less than 0.2 degree. Figure 4.7 illustrates the dc susceptibility measurements performed on the sample using SQUID magnetometer.

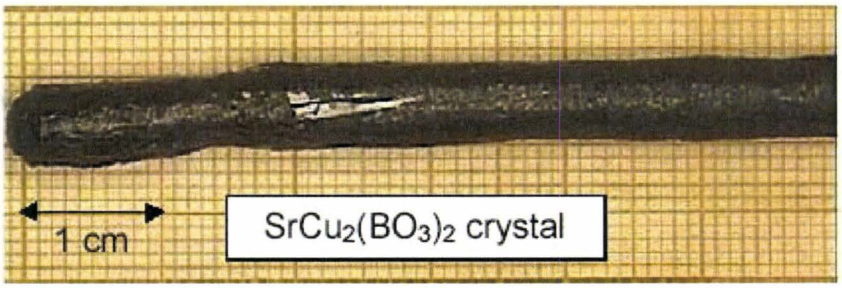

Figure 4.6: Single crystal of $SrCu_2(BO_3)_2$ grown using optical floating zone technique.

Inelastic Neutron Scattering Measurements:

The single crystal was mounted in a pumped ^4He cryostat with the long cylindrical axis vertical, placing the (*H*, 0, *L*) plane of the crystal coincident with the

horizontal scattering plane. Neutron scattering measurements were performed using the Disk Chopper Spectrometer (DCS) and SPINS triple axis spectrometer, both located on cold neutron guides at the NIST Center for Neutron Research.

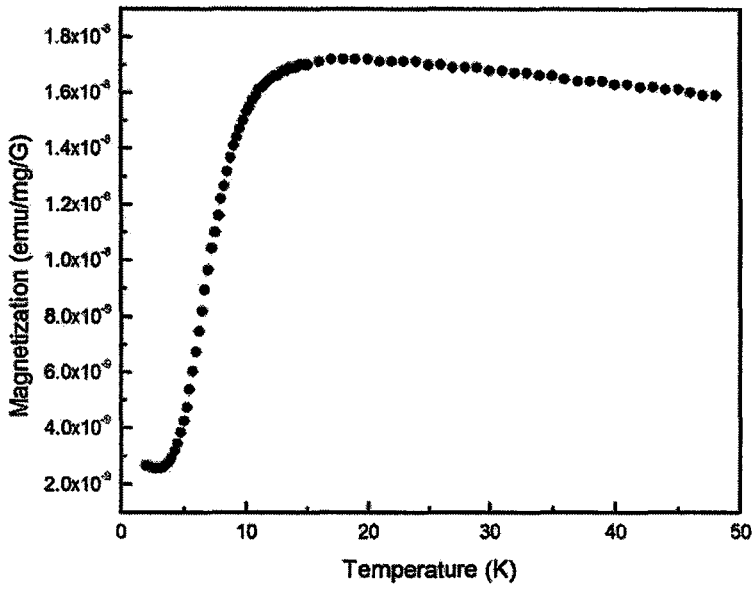

Figure 4.7: SQUID measurements performed on the grown $SrCu_2(BO_3)_2$ single crystal showing the same dc-susceptibility behavior as observed previously by Kageyama *et al.* in 1999b.

The DCS uses choppers to create pulses of monochromatic neutrons whose energy transfers on scattering are determined from their arrival times in the instrument's 913 detectors located at scattering angles from -30 to 140 degrees. Using 5.1 meV incident neutrons, the energy resolution was 0.09 meV. The SPINS triple axis

spectrometer was operated using seven pyrolytic graphite analyzer blades accepting seven degrees in scattering angle, and neutrons of 5 meV, fixed scattered energy. A cooled Be filter was placed in the scattered beam to remove contamination of higher order neutrons, and the resulting energy resolution was ~ 0.5 meV. Figures 4.8 and 4.9 show the schematic picture of the SPINS triple axis spectrometer and DCS time of flight spectrometer.

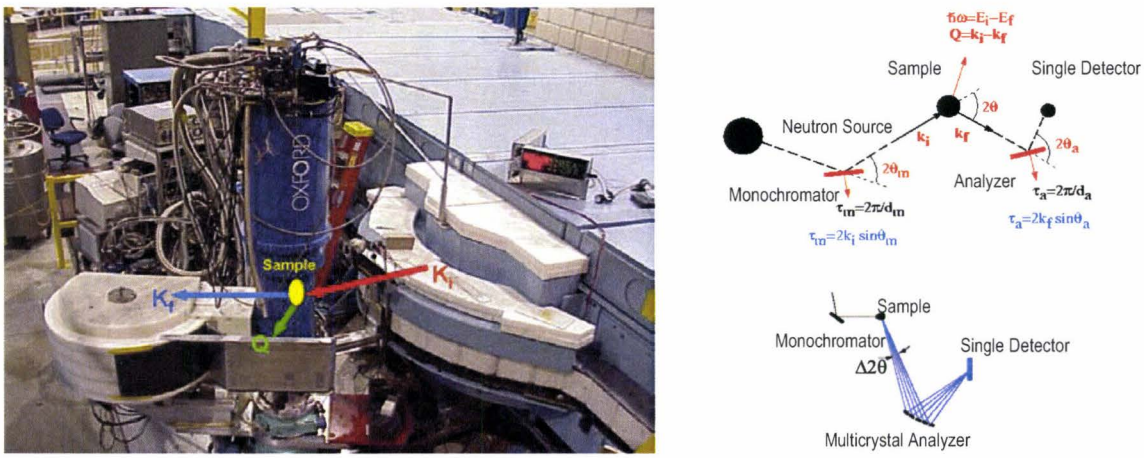

Figure 4.8: (Left panel) The SPINS triple axis spectrometer with a superconducting magnet, located on cold neutron guides at the NIST Center for Neutron Research. (Right panel) A schematic view of the triple axis spectroscopy with multicrystal analyzer (NIST Center for Neutron Reaserch 2005).

4.4.3. Results and Discussions:

SPINS triple axis measurements:

In this study, a series of constant-Q measurements with the triple axis instrument were performed across the (H, 0, L) plane of $SrCu_2(BO_3)_2$ at 1.4K. The summary of such scans with intervals of $\Delta H = 0.2$ is shown in the color contour map in top panel of Figure 4.10, which displays data within the $\hbar\omega$, H plane at K = 0 and L = 0. The bottom panel of the figure shows typical scans making up this map. Top panel of the figure clearly identifies both the n = 1 triplet excitation near $\hbar\omega$ = 3.0 meV and the n = 2 triplet excitation near $\hbar\omega \sim 4.9$ meV. It can also be seen that there is a continuous component to the n = 2 triplet excitation extending to at least 8 meV.

These measurements are qualitatively similar to the low resolution results reported by Kageyama *et al.* (2000a) within the (H, K, 0) plane of $SrCu_2(BO_3)_2$. However, there are important differences. As can be seen in Figure 4.10, there is no substantial dispersion of the maximum of the spectral weight of the n = 2 triplet excitation in contrast to a bandwidth of 1.5 meV reported in the Kageyama *et al.* measurements (2000a). Also it can be seen that the Q-dependence of these excitations is different from that reported by Kageyama *et al* (2000a).

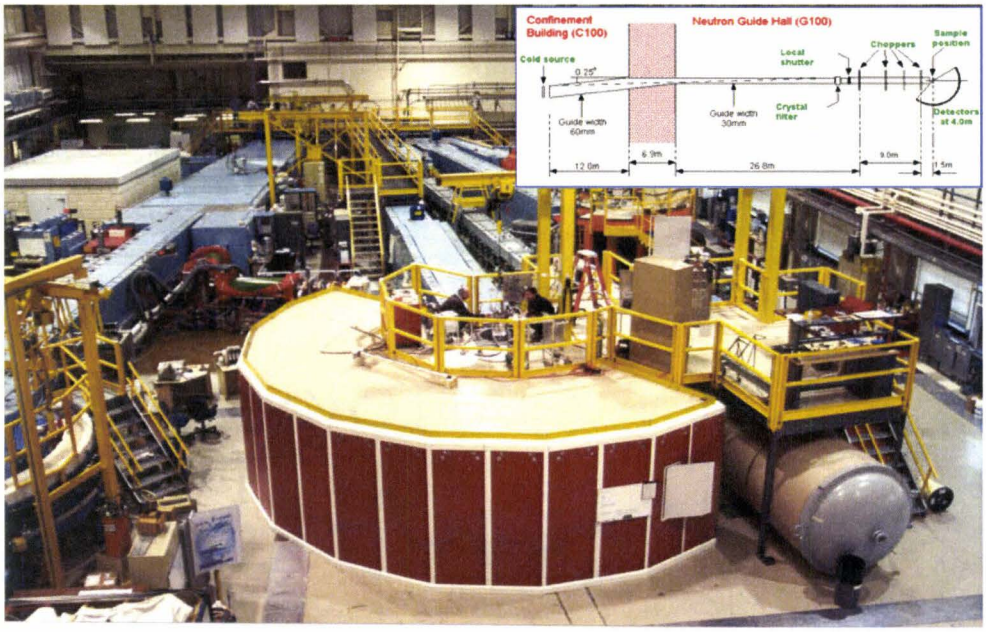

Figure 4.9: The Disk Chopper Spectrometer (DCS) located on cold neutron guides at the NIST Center for Neutron Research. Inset: A schematic view of the spectrometer (NIST Center for Neutron Reaserch 2005).

Figure 4.11 illustrates the results of constant energy scans conducted at $\hbar\omega$ = 3, 4.8, and 9 meV. The energies correspond to the n-triplet excitations with n = 1, 2 and 3, respectively. These measurements show most of the weight of the n = 1 excitation at 3 meV to peak up at half integer values of H (i.e. H = 1.5 and 2.5) within the (H, 0, L) plane, and at integer value of H = 2 for the n = 2 and n = 3 excitations at 4.8 meV and 9 meV, respectively.

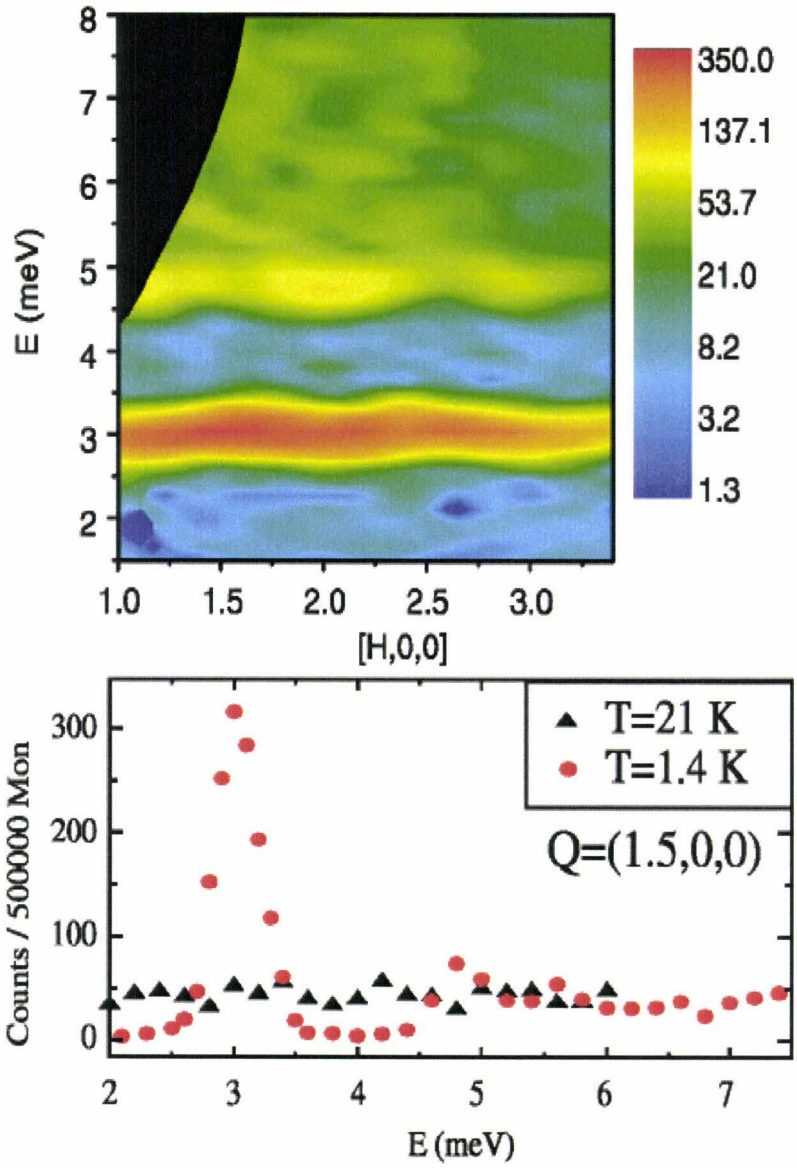

Figure 4.10: Top panel: A map of the measured dynamic structure factor for $SrCu_2(BO_3)_2$ at T = 1.4K along the (H, 0, 0) direction. Bottom panel: Constant-Q scans for Q = (1.5, 0, 0) (Gaulin *et al.* 2004).

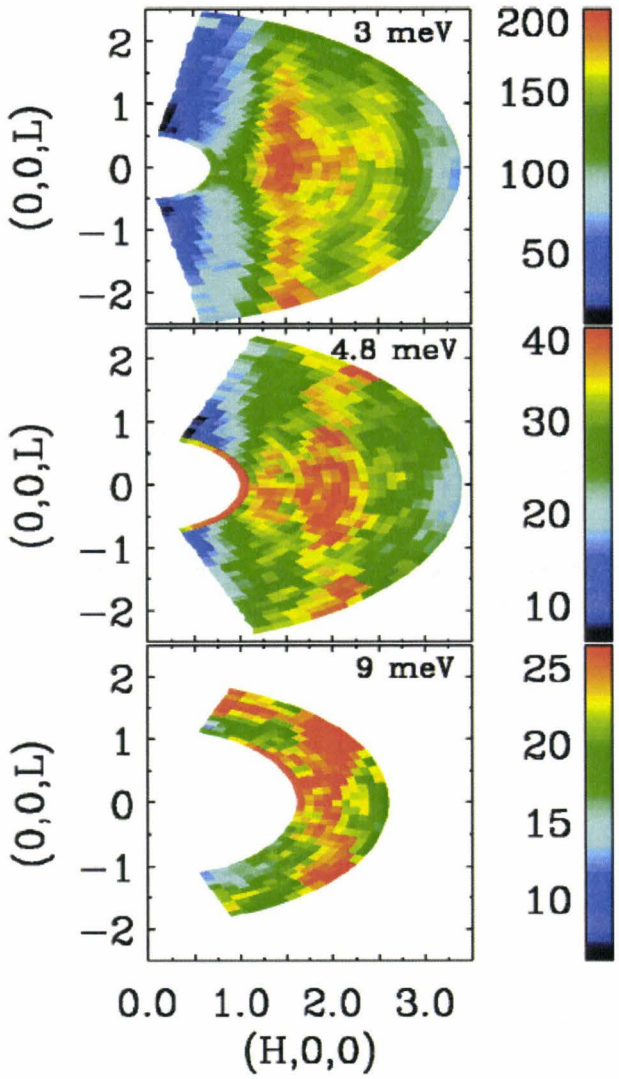

Figure 4.11: Constant energy scans at 3 (top panel), 4.8 (middle panel), and 9 meV (bottom panel) probing the *Q*-dependence of the $n = 1$, 2, and 3 triplet excitations in $SrCu_2(BO_3)_2$ within the (*H*, 0, *L*) plane at $T = 1.4$ K (Gaulin *et al.* 2004).

The results indicate distinct form factors for the n-triplet excitations, in which the $n = 1$ triplet is different from the multi-triplet excitations. Using perturbation techniques, Knetter and Uhrig (2004) recently calculated the $n = 2$ triplet contribution to the dynamic

structure factor within the (*H, K,* 0) plane of $SrCu_2(BO_3)_2$. They specifically showed that there is a peak in the form factor at (2, 0, 0). This is consistent with the inelastic scattering measurements conducted in the present study. Furthermore, there is an excellent agreement between the present results for the $n = 2$ triplet in the (*H,* 0, 0) direction, as shown in Figure 4.11, and the theory. It is also clear from this figure that the *Q*-dependence of all the excitations show little *L*-dependence, consistent with well isolated two-dimensional basal planes.

DCS time of flight measurements:

Since the scattering results show little *L*-dependence, the DCS measurements could be integrated along *L*. These results allow a high precision determination of the dispersion of the $n = 1$ triplet excitations in the (*H,* 0) direction within the tetragonal basal plane. This is illustrated in Figure 4.12. The top panel shows a color contour map of the inelastic scattering. The bottom panel shows cuts through this map, for constant-*Q* scans at (-1, 0), (-1.5, 0), and (-2, 0), respectively from top to bottom. These inelastic measurements clearly resolve three branches of triplet excitation. Earlier work (Cépas *et al.* 2004, Kakurai 2002, Jorge *et al.* 2004, Zorko *et al.* 2003, Nojiri *et al.* 2003) suggests that the dispersion of these branches is a result of DM interaction. The energies of the top and bottom modes at $Q = (-2, 0)$ and (-1, 0) are in excellent agreement with the ESR results of Nojiri *et al.* (1999) who found states at 2.81 meV (679 ± 2 GHz) and 3.16 meV

(764 ± 2 GHz) for $Q = 0$. This splitting arises from the out-of-plane DM interaction, D_{OP}. To the lowest order in J'/J (i.e., ignoring quantum fluctuations), this splitting has the value of $4D_{OP}$ (Gaulin *et al.* 2004). However, the spectrum and its bandwidth are renormalized due to quantum fluctuations. Cépas *et al.* (2001) estimated that this renormalization reduces the bandwidth by a factor of about 2.

The gap between the $S^z = \pm 1$ modes at $Q = (-1.5, 0)$ has been attributed (Karkurai 2002) to the in-plane DM interaction, D_{IP}, which is a result of the buckling of the planes. This splitting, which has the theoretical value of $2\sqrt{2}\,D_{IP}$ (Gaulin *et al.* 2004), is observed to be about 0.18 meV for the present measurements. Details of the renormalization of the value of this gap due to quantum fluctuations are at present unknown. However, if the renormalization for in and out-of-plane DM interactions were similar, then D_{IP} would be about $0.7D_{OP}$, which is quite large in light of the small magnitude of the buckling of the layers (Cépas *et al.* 2001).

The middle panel of Figure 4.12 shows the $S^z = 0$ mode, which is sketched along with higher and lower energy $S^{\pm}$ modes. This mode is predicted to have a zero form factor at $Q = (1.5, 0)$ (Cépas *et al.* 2001) and is expected to be centered between the top and bottom $S^{\pm}$ bands, whose form factors are maximal near (1.5, 0). The bandwidth of the $S^z = 0$ mode is extremely small, roughly 0.1 meV, and it is known to be least affected by anisotropic interactions; hence it is most directly comparable to calculations of the $n = 1$ triplet excitation based on Equation 4.1. This bandwidth, which scales as x^6 ($x = J'/J$), is similar to the bandwidth found by Weihong *et al.* (1999) for $x = 0.6$ and is about 4% of the $n = 1$ triplet gap energy.

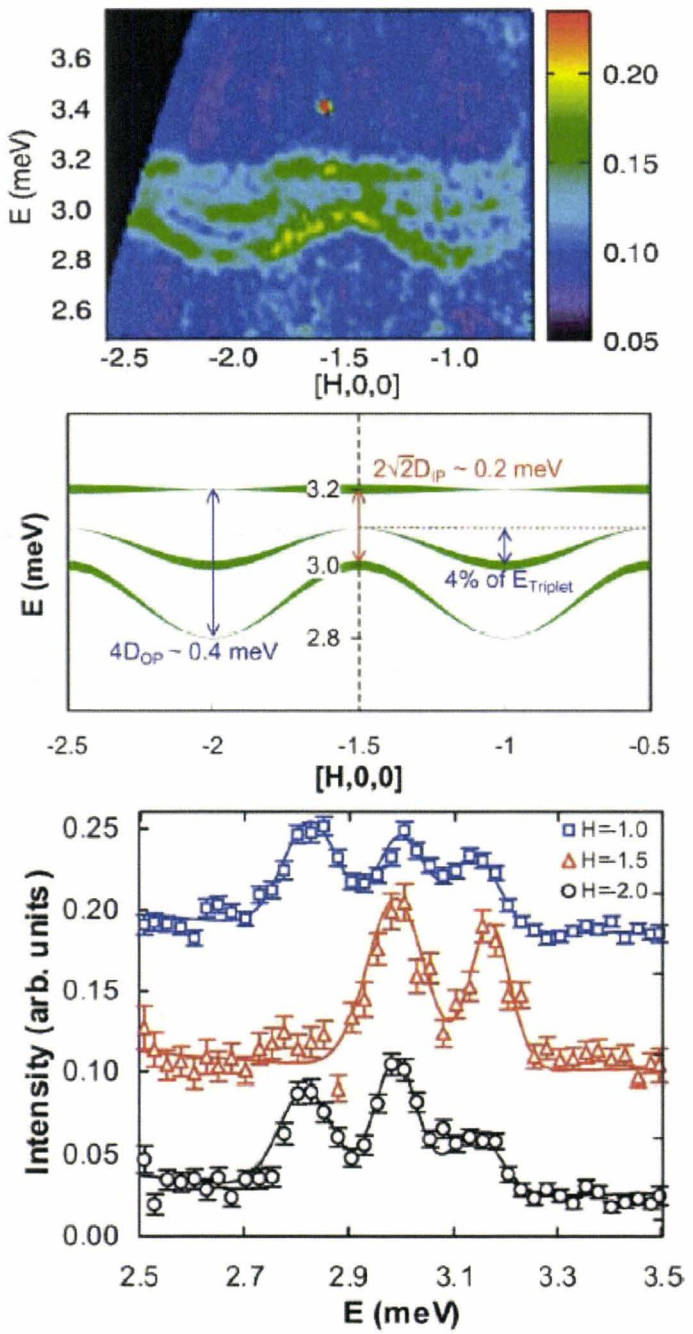

Figure 4.12: Top panel: Color contour map of the dynamic structure factor for the n = 1 triplet excitations along the (H, 0) direction within the basal plane of $SrCu_2(BO_3)_2$ measured with the DCS spectrometer at T = 1.4K and integrated along L. Middle panel: A cartoon of the dispersion and form factors appropriate to the S^z and $S^{\pm}$ n = 1 triplet excitations. Bottom panel: Cuts through the map of the top panel, which approximate constant-Q scans and clearly resolve the three branches to the n = 1 triplet excitation.

Temperature Dependence measurements:

The temperature dependence of both $n = 1$ and $n = 2$ triplet excitations and that of the $n = 1$ triplet excitations were measured using SPINS and DCS, respectively. The SPINS measurements at $Q = (1.5, 0, 0)$ and $(2, 0, 0)$ and energy transfers of $\hbar\omega = 3$ and 4.85 meV, for the $n = 1$ and $n = 2$ triplet excitations, respectively, are shown in Figure 4.13. The DCS measurements integrate the inelastic scattering in data sets of the form shown in the top panel of Figure 4.12. The DCS measurements integrate between 2.7 and 3.3 meV and across all wave vectors from $H = -2.25$ to $H = -0.75$ along $(H, 0)$ within the basal plane.

As it can be see in Figure 4.13, the temperature dependences of the $n = 1$ and $n = 2$ triplet excitations are identical. This could not have been concluded from earlier measurements (Kageyama *et al.* 2000b). The temperature dependence of the inelastic scattering can be very well described as the complement of the dc susceptibility (Jorge *et al.* 2004). The complement of χ, referred to as $1 - \chi$ in Figure 4.13, is given by $\chi\,(T = 20\text{K}) - \chi\,(T)$ and is scaled to compare the temperature dependence of the inelastic scattering. It can be seen from Figure 4.13 that this provides an excellent description of the temperature dependence of the inelastic scattering.

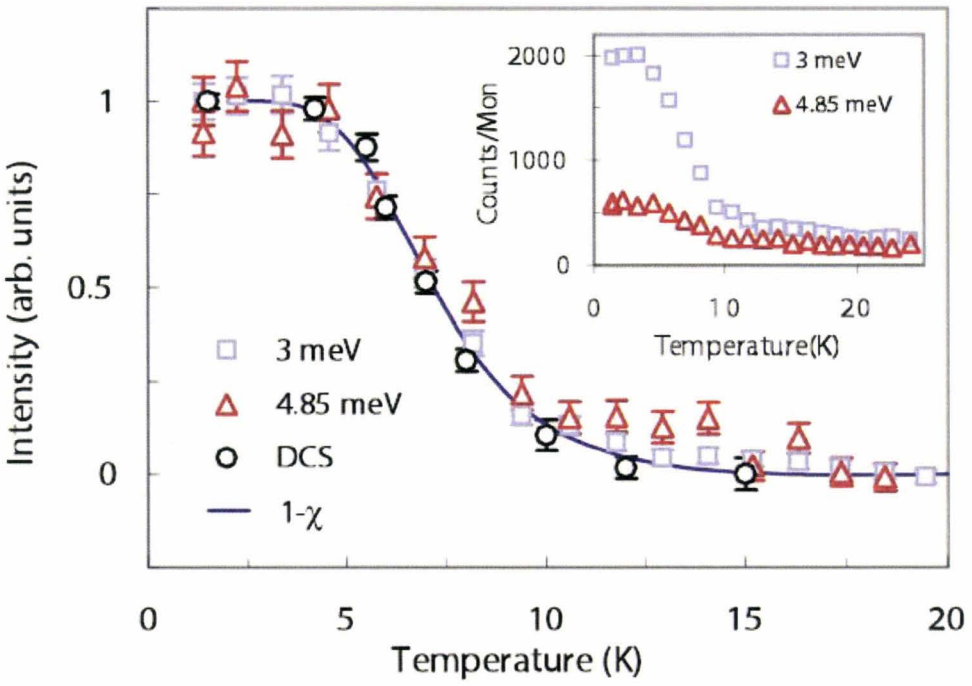

Figure 4.13: The temperature dependence of inelastic intensity at (1.5, 0, 0) and $\hbar\omega$= 3 meV, as well as at (2, 0, 0) and $\hbar\omega$= 4.85 meV. The inset shows the raw intensity data, while the main figure shows the normalized intensity assuming zero at 20K and compared to the complement of the measured dc susceptibility (1 – χ).

4.5. Neutron Diffraction Studies of $SrCu_2(BO_3)_2$:

As was discussed previously, the crystal structure of $SrCu_2(BO_3)_2$ is tetragonal and is characterized by a layered structure of $CuBO_3$ and Sr planes (Smith and Keszler 1991, Kageyama *et al.* 1999a, Sparta *et al.* 2001). In the $CuBO_3$ layer, BO_3 molecules make a triangle and the Cu^{2+} ions are connected through the BO_3 molecules. All the Cu^{2+} ions are located at crystallographically equivalent sites and have a spin S = 1/2. Each

Cu^{2+} ion has one nearest-neighbour Cu^{2+} ion and four next-nearest-neighbour Cu^{2+} ions in the plane. A pair of nearest-neighbour Cu^{2+} ions are connected through O sites, which are vertices of BO_3 triangles, form a dimer unit. The dimer units are connected orthogonally through BO_3 molecules. The distance between the nearest-neighbour Cu^{2+} ions is 2.905 Å, and that between the next nearest-neighbour Cu^{2+} ions is 5.132 Å at room temperature. A buckling of the $CuBO_3$ plane is observed below 395K (Sparta *et al.* 2001). The unit cell in the layer contains two types of dimer which are mutually orthogonal. One type of dimer makes a flat plane and the two planes, corresponding to the orthogonal dimers, are slightly shifted from each other.

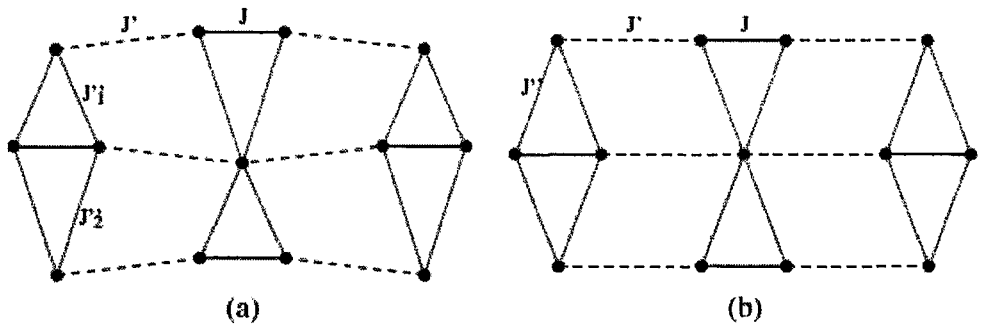

Figure 4.14: (a) A sketch of the projection of the dimer bonds along [110] at 100K showing a buckling of the $CuBO_3$ plane (b) A sketch at 433K showing the $CuBO_3$ plane as a mirror plane (Sparta *et al.* 2001).

4.5.1. Previous Experiments:

Sparta *et al.* (2001) were the first to report that in $SrCu_2(BO_3)_2$ at T_s = 395K, a structural phase transition from the space group $I\bar{4}2$ to $I4/mcm$ (both are tetragonal) has been observed by X-ray diffraction. One can see from Figure 4.14 (a) that below T_s there is a buckling in the $CuBO_3$ plane. As shown in Figure 4.14 (b), above T_s two dimers in the unit cell lie in the same plane and there is no buckling of the $CuBO_3$ plane; therefore, the $CuBO_3$ plane is a mirror plane. The existence of a mirror plane is important for possible Dzyaloshinsky-Moriya interactions. Above T_s, the DM interactions may exist only for the next-nearest neighbor pairs and do not exist for the nearest-neighbor pairs, since the middle of a nearest-neighbor bond is an inversion centre. However, below T_s, the mirror plane is lost; therefore, Dzyaloshinsky-Moriya interactions can exist for both next-nearest-neighbor pairs and nearest-neighbor pairs.

Jorge *et al.* (2004), performed specific heat measurements on $SrCu_2(BO_3)_2$ in a continuous magnetic field H up to 33T. They argued that an intra-dimer Dzyaloshinsky-Moriya (DM) interaction, which violates the observed crystal symmetry at temperatures below T_s = 395K is required to explain the low temperature specific heat of $SrCu_2(BO_3)_2$ in magnetic fields H > 18T (Cépas *et al.* 2001, Cépas and Ziman 2002, Nojiri *et al.* 2003).

The components of the *nn* DM interaction are constrained by the crystal symmetry at low temperatures (Sparta et al. 2001, Cépas *et al.* 2001). According to this symmetry, the *z*-component of D (*nn* DM interactions) must be zero. Jorge *et al.* (2004) proposed that, there may be a structural phase transition at low temperatures that lowers

the crystal symmetry allowing a non-zero value for the z-component of the nearest neighbor DM interaction. The fact that the symmetry of the system is affecting the Dzyaloshinsky-Moriya interactions and consequently changes the thermal and magnetic properties of the material, may be helpful in adapting a better theory for the system which can better explain the experimental results.

Following the arguments made by Jorge *et al.* (2004), neutron diffraction measurements were performed in order to investigate any possible structural phase transition in $SrCu_2(BO_3)_2$ at low temperatures.

4.5.2. Experimental Details:

Elastic neutron diffraction measurements were performed on a fine powder sample of $SrCu_2(BO_3)_2$ with 2.37 Å and 1.3Å neutrons at the C2 diffractrometer of the Chalk River Laboratories from 3K to 20K. The crystal was mounted in a pumped ^4He cryostat with the long cylindrical axis vertical. High and low resolution measurements were done in steps of 0.25 degree covering the range of 5 to 85 degree in 2θ for $\lambda =$ 2.37Å and from 5 to 115 degree in 2θ for $\lambda = 1.3$Å.

4.5.3. Results and Discussions:

Figures 4.15 and 4.16 show the results of the elastic neutron diffraction measurements performed on $SrCu_2(BO_3)_2$ to investigate any possible structural phase transition in this material at low temperatures. Figure 4.15 shows the results for $\lambda = 1.3$Å at 3.8K and 20K temperatures while Figure 4.16 shows the results for $\lambda = 2.37$Å at 3.8K and 20K temperatures. In both figures, black squares and red circle represent the data collected at 3.8K and 20K, respectively. In order to find any possible variation in the diffraction spectra indicating a possible structural phase transition of the material, the difference between the measurements at these two temperatures was calculated. The green upward triangles represent the subtracted values. The blue downward triangles show the subtracted values binned to ease the detection of variation between the two spectrums.

It can be seen from the figures that the diffraction spectrum for both wavelength at T = 3.8K and 20K are the same. This indicates that there is no structural phase transition in $SrCu_2(BO_3)_2$ in this temperature range. Therefore, more theoretical and experimental research is needed to clarify the observed behavior of the heat capacity and ESR spectrum reported by Jorge *et al.* (2004).

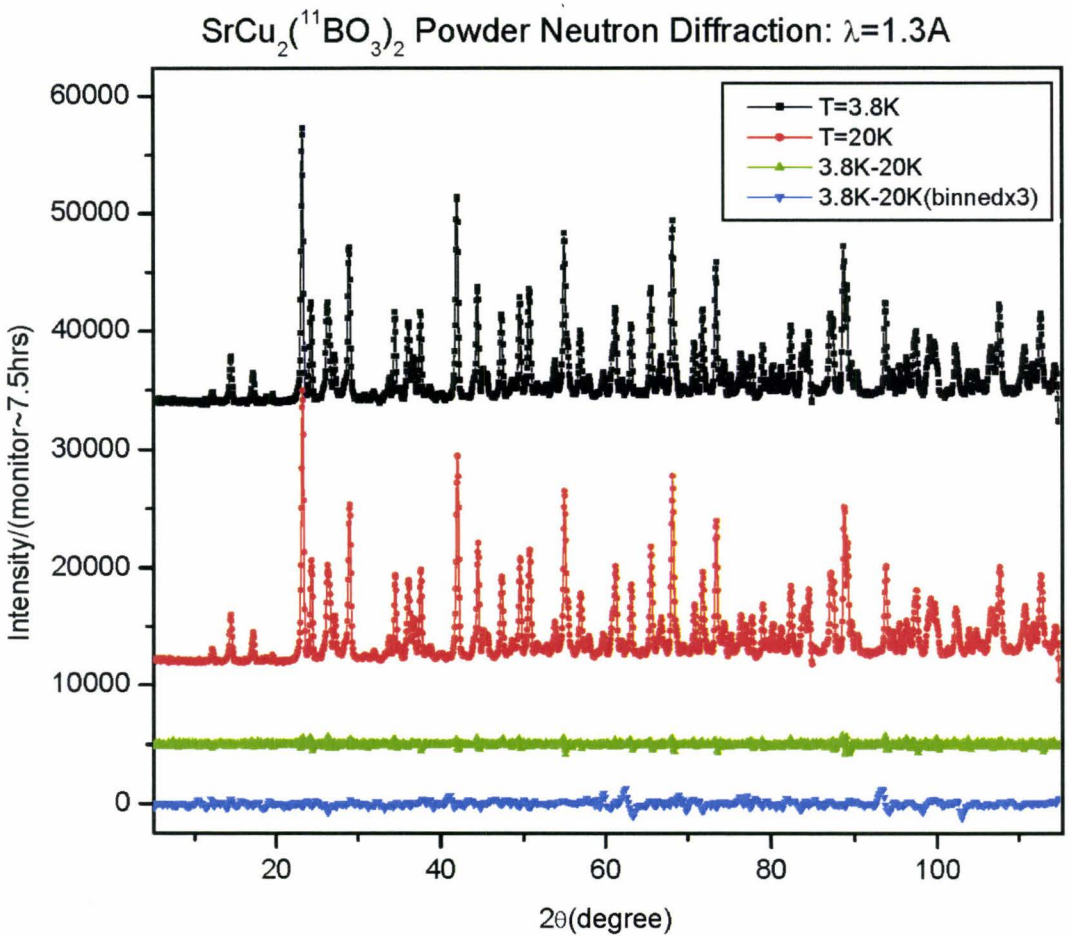

Figure 4.15: The result of the elastic neutron diffraction measurements performed on $SrCu_2(BO_3)_2$ for λ = 1.3Å at 3.8K and 20K temperatures.

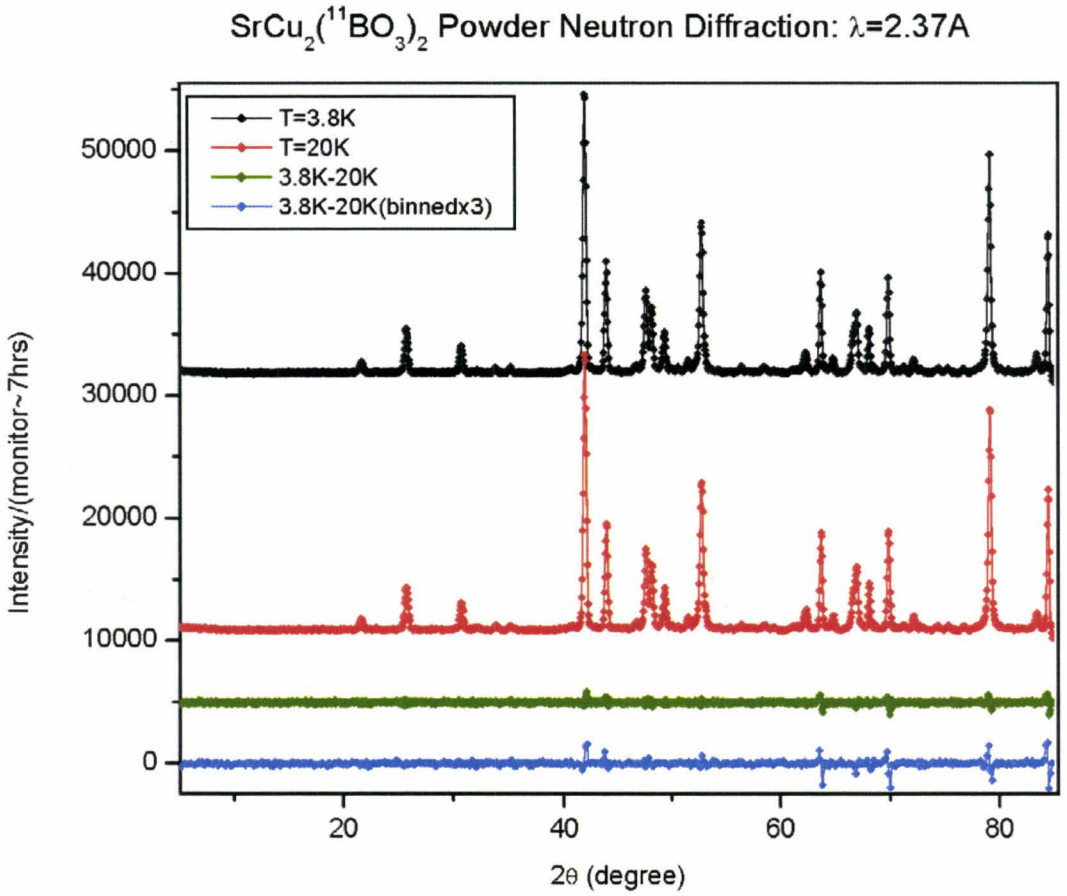

Figure 4.16: The result of the elastic neutron diffraction measurements performed on $SrCu_2(BO_3)_2$ for $\lambda = 2.37$Å at 3.8K and 20K temperatures.

4.6 Conclusion:

For this study, a high quality single crystal of $SrCu_2(^{11}BO_3)_2$ was grown from a self-flux by floating zone image furnace techniques. New high-resolution inelastic neutron scattering measurements were conducted on this single crystal on the (*H*, 0, *L*) plane. Measurements were performed on two different high-resolution cold neutron instruments at the NIST Center for Neutron Research, SPINS and DCS, allowing both high energy resolution to resolve the three $n = 1$ triplet excitations in $SrCu_2(BO_3)_2$, and high Q resolution to detect different Q dependencies among the n-triplet excitations, where $n = 1$, 2, and 3. In addition, neutron powder diffraction measurements were performed on a sample to investigate the possibility of a proposed structural phase transition in this compound.

The inelastic neutron scattering measurements identify both the $n = 1$ triplet excitation near $\hbar\omega = 3.0$ meV and the $n = 2$ triplet excitation near $\hbar\omega \sim 4.9$ meV. It can also be seen that there is a continuous component to the $n = 2$ triplet excitation extending to at least 8 meV. In addition, the results show that the $n = 1$ excitation (3 meV) peaks up at half integer values of $H = 1.5$ and 2.5, the $n = 2$ (4.8 meV) and $n = 3$ (9 meV) excitations peak up at integer value of $H = 2$, within the (*H*, 0, *L*) plane. It was also observed that the Q-dependence of all the excitations demonstrate little L-dependence. Thus the scans were integrated along L to allow a high precision determination of the dispersion of the $n = 1$ triplet excitations in the (*H*, 0) direction.

Examining the data reveals qualitative similarities to the low resolution results previously reported by Kageyama *et al.* within the (*H*, *K*, 0) plane of $SrCu_2(BO_3)_2$ but

with some important differences. It can be seen that there is no substantial dispersion of the maximum of the spectral weight of the $n = 2$ triplet excitation in contrast to what was reported by Kageyama *et al.* and that the Q-dependence of these excitations is different from that reported by Kageyama *et al.* The data also indicates distinct form factors for the n-triplet excitations.

Further analysis of the present inelastic neutron scattering measurements revealed that the triplet excitation exists in three non degenerate branches, which arises from the out-of-plane DM interaction. However, the gap between the $S^z = \pm 1$ modes at $Q = (-1.5, 0)$ has been attributed (Karkurai 2002) to the in-plane DM interaction, which is a result of the buckling of the planes and was observed to be about 0.18 meV for the present measurements.

Moreover, the temperature dependence of both $n = 1$ and $n = 2$ triplet excitations and that of the $n = 1$ triplet excitations were measured using SPINS and DCS, respectively. It is seen that the temperature dependences of the $n = 1$ and $n = 2$ triplet excitations are identical, which could not have been concluded from measurements reported by Kageyama *et al.* It was also shown that the temperature dependence of the inelastic scattering can be very well described as the complement of the dc susceptibility

In order to investigate any possible structural phase transition in $SrCu_2(BO_3)_2$, high and low resolution elastic neutron diffraction measurements with $\lambda = 2.37$Å and $\lambda = 1.3$Å for $T = 3.8$K and 20K were performed. Measurements indicate that there is no structural phase transition in $SrCu_2(BO_3)_2$ in this temperature range.

References:

Aharony, A. & Ahlers, G. *Phys. Rev. Lett.* **44**, 782 (1980).

Albrecht, M. & Mila, F. *Europhys. Lett.* **34**, 145 (1980).

Ashcroft, N. W. & Mermin, N. D. *Solid State Physics,* Sauders College Publishing, Toronto (1976).

Bloch, D., Voiron, J., Bonner, J. C., Bray, J. W., Jacobs, I. S. & Interrante, L. V. *Phys. Rev. Lett.* **44**, 294 (1980).

Bloch, D., Voiron, J., Bray, J. W., Jacobs, I. S., Bonner, J. C. & Kommandeur, J. *Phys. Lett.* A **82**, 21 (1981).

Bonner, J. C. & Fisher, M. E. *Phys. Rev.* **135**, A640 (1964).

Bray, J. W., Hart, H. R. Jr, Interrante, L. V., Jacobs, I. S., Kasper, J. S., Watkins, G. D., Wee, S. H. & Bonner, J. C. *Phys. Rev. Lett.* **35**, 744 (1975).

Bray, J. W., Interrante, L. V., Jacobs, I. S. & Bonner, J. C. *Extended Linear Chain Compounds* , Vol. 3rd, Plenum Press (1983).

Bulaevskii, L. N. *Fiz. Tverd. Tela.* **11**, 1132, 1969. Engl. transl. *Sov. Phys.–Solid State* **11**, 921 (1969).

Bulaevskii, L. N., Buzdin, A. I. & Khomskii, D. I. *Solid State Commun.* **27**, 5 (1978).

Cépas, O., Kakurai, K., Regnault, L. P., Ziman, J. P. B. T., Aso, N., Nishi, M., Kageyama, H. & Ueda, Y. *Phys. Rev. Lett.* **87**, 167205 (2001).

Cépas, O. & Simon, T. *cond-mat* /0207191 (2002).

Chung, C. H., Marston, J. B. & Sachdev, S. *Phys. Rev. B* **64,** 134407 (2001).

Coad, S., Petrenko, O., Paul D. McK, Fåk, B., Lussier, J-G. & McMorrow, D. F. *Physica B* **239,** 350 (1997).

Collins, M.F. *Magnetic Critical Scattering*, Oxford, New York (1989).

Copley, J. & Terrence, U. *J. Res. Natl. Inst. Stand. Technol.* **98**, 71-87 (1993).

Cross , M. C., & Fisher, D. S. *Phys. Rev. B* **19**, 402 (1979).

Cross, M. C. *Phys. Rev. B* **20**, 4606 (1979).

Dzyaloshinski, I. *J. Phys. Chem. Solids* **4**, 241 (1958).

Fujita, M., Ubukata, K., Arai, M., Tonegawa, T., Mino, M., Motokawa, M., Knight, K., Forsyth, B., Bennington, S. M., Akimitsu, J. & Fujita, O., *Physica B* **219** and **220**, 95 (1996).

Fukuyama, H., Tanimoto, T. & Saito, M. *J. Phys. Soc. Japan* **65**, 1182 (1996).

Furrer, A. *Magnetic Neutron Scattering*, Vol. 1st, World Scientific, Singapore (1995).

Gaulin, B. D., Lee, S. H., Haravifard, S., Castellan, J. P., Berlinsky, A. J., Dabkowska, H. A., Qiu, Y. & Copley, J. R. D. *Phys. Rev. Lett.* **93**, 267202 (2004).

Haldane, F. D. M., *Phys. Rev. Lett.* **50**, 1153 (1983).

Hamamoto, T., Adachi, N., Kido, G., Hase, M., Sasago, Y. & Uchinokura, K. *J. Phys. Soc. Japan* **63**, 1218 (1994).

Harris, Q. J., Feng, Q., Birgeneau, R. J., Hirota, K., Kakurai, K., Lorenzo, J. E., Shirane, G., Hase, M., Uchinokura, K., Kojima, H., Tanaka, I. & Shibuya, Y. *Phys. Rev. B* **50**, 12606 (1994).

Harris, Q. J., Feng, Q., Birgeneau, R. J., Hirota, K., Shirane, G., Hase, M. & Uchinokura, K. *Phys. Rev. B* **52**, 15420 (1995).

Hase M., Sasago Y., Terasaki I., Uchinokura K., Kido G. & Hamamoto T. *J. Phys. Soc. Japan* **65**, 273 (1996).

Hase M., Terasaki I., Sasago Y., Uchinokura K., Tokunaga M., Miura N., Kido G., Hamamoto T. & Obara H. *Physica B* **201**, 167 (1994).

Hase, M., Koide, N., Manabe, K., Sasago, Y., Uchinokura, K. & Sawa, A. *Physica B* **215**, 164 (1995).

Hase, M., Terasaki, I. & Uchinokura, K. *Phys. Rev. Lett.* **70**, 3651 (1993a).

Hase, M., Terasaki, I., Uchinokura, K., Tokunaga, M., Miura, N. & Obara, H. *Phys. Rev. B* **48**, 9616 (1993b).

Hase, M., Terasaki, I., Sasago, Y., Uchinokura, K. & Obara, H. *Phys. Rev. Lett.* **71**, 4059 (1993c).

Hase, M., Uchinokura, K., Birgeneau, R. J., Hirota, K. & Shirane, G. *J. Phys. Soc. Japan* **65**, 1392 (1996).

Hirota, K., Cox, D. E., Lorenzo, J. E., Shirane, Tranquada, G., J. M., Hase, M., Uchinokura, K., Kojima, H., Shibuya, Y. & Tanaka , I. *Phys. Rev. Lett.* **73**, 736 (1994).

Isobe, M. & Ueda, Y. *J. Phys. Soc. Japan* **65**, 3142 (1996).

Jorge, G. A., Stren, R., Jaime, M., Harrison, N., Bonča, J., Shawish, S. El, Baista, C. D. , Dabkowska, D. A. & Gaulin, B. D. *cond-mat*/0309534 (2004).

Kadanof, L. P. *Phase Transition and Critical Phenomena*, Academic Press (1976).

Kageyama, H., Nishi, M., Aso, N., Onizuka, K., Yosihama, T., Nukui, K., Kodama, K., Kakurai, K. & Ueda, Y. *Phys. Rev. Lett.* **84**, 5876 (2000).

Kageyama, H., Onizuka, K., Ueda, Y., Nohara, M., Suzuki, H. & Takagi, N. *J. Exp. Theor. Phys.* **90**, 129 (2000).

Kageyama, H., Onizuka, K., Yamauchi, T., Ueda, Y., Hane, S., Mitamura, H., Goto, T., Yoshimura, K. & Kosuge, K. *J. Phys. Soc. Japan* **68**, 1821 (1999).

Kageyama, H., Ueda, Y., Narumi, Y., Kindo, K., Kosaka, M. & Uwatoko, Y. *Prog. Theor. Phys. Suppl.* **145**, 17 (2002).

Kageyama, H., Yoshimura, K., Stern, R., Mushnikov, N., Onizuka, K., Kato, M., Kosuge, K., Slichter, C., Goto, T. & Ueda, Y. *Phys. Rev. Lett.* **82**, 3168 (1999).

Kakurai, K. *Quantum Properties of Low Dimensional Antiferromagnets*, Kyushu University Press, Fukuoka (2002).

Kamimura, O., Terauchi, M., Tanaka, M., Fujita, O. & Akimitsu, J. *J. Phys. Soc. Japan* **63**, 2467 (1994).

Kiryukhin, V. & Keimer, B. *Phys. Rev. B.* **52**, R704 (1995).

Kittle, C. *Introduction to Solid State Physics*, John Wiley & Sons Inc., New York (1986).

Knetter, C., Bühler, A., Müller-Hartmann, E. & Uhrig, G. S. *Phys. Rev. Lett.* **85** 3958 (2000).

Knetter, C., Müller-Hartmann, E. & Uhrig, G. S. *J. Phys.: Condens. Matter* **12** 9069 (2000).

Knetter, C. & Uhrig, G. S. *Phys. Rev. Lett.* **92**, 027204 (2004).

Kodama, K., Takigawa, M., Horvatić, M., Berthier, C., Kageyama, H., Ueda, Y., Miyahara, S., Becca, F. & Mila, F. *Science* **298**, 395 (2002).

Kodama, K., Yamazaki, J., Takigawa, M., Kageyama, H., Onizuka, K. & Ueda, Y. *J. Phys.: Condens. Matter* **14**, L319 (2002).

Koga, A. & Kawakami, N. *Phys. Rev. Lett.* **84**, 4461 (2000).

Koide, N., Uchiyama, Y., Hayashi, H., Masuda, T., Sasago, Y., Uchinokura, K., Manabe, K. & Ishimoto, H. *cond-mat*/9805095 (1998).

Koide, N., Sasago, Y., Masuda, T. & Uchinokura, K. *Czech. J. Phys.* **46** (S2), 1981 (1996).

Landau, L. D. & Lifshitz, E. M., *Statistical Physics*, Addison-Wesley, Reading, Mass. (1969).

Läuchli, A., Wessel, S., & Sigrist, M. *Phys. Rev. B* **66**, 014401 (2002).

le Guillou, J. C. & Zinn-Justin, J. *Phys. Rev. B* **21**, 3976 (1980).

Lemmens, P., Grove, M., Fischer, M., Guntherodt, G., Kotov, V. N., Kageyama, H., Onizuka, K. & Ueda, Y. *Phys. Rev. Lett.* **85**, 2605 (2000).

Liu , X., Wosnitza, J., von Lohneysen , H. & Kremer, R. K., *Z. Phys. B* **98**, 163 (1995)

Lorenz , T., Ammerahl, U., Auweiler, T., Büchner, B., Revcolevschi, A., & Dhalenne, G. *Phys. Rev. B* **55**, 5914 (1997).

Lumsden, M. D., Gaulin, B. D. & Dabkowska, H. *Phys. Rev. Lett.* **76**, 4919 (1996).

Lumsden, M. D., Gaulin, B. D. & Dabkowska, H. *Phys. Rev. B.* **57**, 14097 (1998a).

Lumsden, M. D., Gaulin, B. D. & Dabkowska, H. *Phys. Rev. B.* **58**, 12252 (1998b).

Lussier, J. G., Coad, S. M., McMorrow, D. F. & Paul, D. McK. *J. Phys.: Condens. Matter* **7**, L325 (1995).

Manousakis, E. *Rev. Mod. Phys.* **63**, 1 (1991).

Martin, M. C., Hase, M., Hirota, K., Shirane, G., Sasago, Y., Koide, N. & Uchinokura, K. *Phys. Rev. B* **56**, 3173 (1997).

Masuda, T., Fujioka, A., Uchiyama, Y., Tsukada, I. & Uchinokura, K. *Phys. Rev. Lett.* **80**, 4566 (1998).

Miyahara, S. & Ueda, K. *Phys. Rev. Lett.* **82**, 3701 (1999).

Miyahara, S. & Ueda, K. *J. Phys. Soc. Japan.* **69**, Suppl. B, 72 (2000).

Miyahara, S. & Ueda, K. *J. Phys. Condens. Matter* **15**, R327 (2003).

Moncton , D. E., Birgeneau, R. J., Interrante , L. V. & Wudl , F. *Phys. Rev. Lett.* **39**, 507 (1977).

Moriya, T. *Phys. Rev.* **120**, 91 (1960).

Müller-Hartmann, E., Singh, R. R. P., Knetter, C. & Uhrig, G. S. *Phys. Rev. Lett.* **84**, 1808 (2000).

Munehisa, T. & Munehisa, Y. J. *Phys. Soc. Japan.* **72**, 160 (2003).

Nishi, M., Fujita, O. & Akimitsu, J. *Phys. Rev. B* **50**, 6508 (1994).

Nojiri, H., Kageyama, H., Onizuka, K., Ueda, Y. & Motokawa, M. *J. Phys. Soc. Japan* **68**, 2906 (1999).

Nojiri, H., Kageyama, H., Ueda, Y. & Motokawa, M. *cond-mat*/0212479 (2003).

Northby, J. A., Groenendijk, H. A., de Jongh, L. J., Bonner, J. C., Jacobs, I. S. & Interrante, L.V. *Phys. Rev. B* **25,** 3215 (1982).

Oseroff, S. B., Cheong, S. W., Aktas, B., Hundley, M. F., Fisk, Z. & Rupp, L. W. Jr. *Phys. Rev. Lett.* **74,** 1450 (1995).

Peierls, R. E., *Quantum Theory of Solids*, Oxford University Press, London (1955).

Plischke, M. & Bergersen, B. *Equilibrium Statistical Physics*, Prentice Hall, Englewood Cliffs, NJ (1989).

Plumer, M., *Phys. Rev. B* **53**, 594 (1996).

Pouget, J. P., Regnault, L. P., Ain, M., Hennion, B., Renard, J. P., Veillet, P., Dhalenne, G. & Revcolevschi, A. *Phys. Rev. Lett.* **72,** 4037 (1994).

Regnault, L. P., Renard, J. P., Dhalenne, G. & Revcolevschi, A. *Europhys. Lett.* **32**, 579 (1995).

Regnault, L. P., Aïn, M., Hennion, B., Dhalenne, G. & Revcolevschi, A. *Phys. Rev. B.* **53**, 5579 (1996).

Renard, J. P., Le Dang, K., Veillet, P., Dhalenne, G., Revcolevschi ,A. & Regnault, L. P. (1995) *Europhys. Lett.* **30**, 475.

Rõõm, T., Nagel, U., Lippmaa, E., Kageyama, H., Onizuka, K. & Ueda, Y. *Phys. Rev. B* **61**, 14342 (2000).

Sahling, S., Lasjaunias, J. C., Monceau, P. & Revcolevschi, A. *Solid State Commun.* **92**, 423 (1994).

Saint Paul, M., Monceau, P. & Revolevschi, A. *Solid State Commun.* **93**, 7 (1995).

Sakurai, J. J. *Modern Quantum Mechanics*, Addison-Wesley Publishing Company Inc. (1985).

Sasago, Y., Koide, N., Uchinokura, K., Martin, M. C., Hase, M., Hirota, K. & Shirane, G. *Phys. Rev. B* **54**, R6835 (1996).

Shastry, S. & Sutherland, B. *Physica* **108B**, 1069 (1981).

Skjeltorp, A. T. & Sherrington, D. *Dynamical Properties of Unconventional Magnetic Systems*, NATO ASI, Ser. E, Vol. 349 Kluwer Academic, Boston (1998).

Smith, R.W. & Keszler, D. A. *J. Solid State Chem.* **93**, 430 (1991).

Sparta, K., Redhammer, G.J., Roussel, P., Heeger, G., Roth, G., Lemmens, P., Ionescu, A., Grove, M., Güntherodt, G., Hüning, F., Lueken, H., Kageyama, H., Onizuka, K., Ueda,Y. *Eur. Phys. J.* **19**, 507 (2001).

Squires, G. L. *Introduction to the Theory of Thermal Neutron Scattering*, Dover, Mineola (1996).

Stanley, H. E., *Introduction to Phase Transition and Critical Phenomena*, Clarendon Press, Oxford (1971).

Sutherland, B. & Shastry, B. S. *J. Stat. Phys.* **33**, 477 (1983).

Takushima, Y., Koga, A. & Kawakami, N. *J. Phys. Soc. Japan* **70**, 1369 (2001).

Tanaka, Y., Satoh, N. & Nagasaka, K., *J. Phys. Soc. Japan* **59**, 319 (1990).

Totsuka, K., Miyahara, S. & Ueda, K. *Phys. Rev. Lett.* **86**, 520 (2001).

Uchinokura, K., Hase, M. & Sasago, Y. *Physica B* **211**, 175 (1995).

Ueda, K. & Miyahara, S. *J. Phys.: Condens. Matter* **11**, L175 (1999).

Völlenkle, H., Wittmann, A. & Nowotny, H. *Monatsh. Chem.* **98**, 1352 (1967).

van Bodegom, B., Larson, B. C. & Mook, H. A. *Phys. Rev. B* **24**, 1520 (1981) .

Weast, R.C. *Handbook of Physics and Chemistry 62nd Edition*, CRC Press, Boca Raton, FL. (1981).

Weihong, Z., Oitmaa, J. & Hamer, C. J. *Phys. Rev. B* **60**, 6608 (1999).

Winkelmann, H., Gamper, E., Büchner, B., Braden, M., Revcolevschi, A.& Dhalenne, G. *Phys. Rev. B* **51**, 12884 (1995).

Zheng, W., Hamer, C. & Oitmaa, J. *Phys. Rev. B* **60**, 6608 (1999).

Zorko, A., Arcon, D., van Tol, H., Brunel, L.C. & Kageyama, H. *cond mat*/0311079 (2003).